Technische Universität München
TUM School of Engineering and Design

TUM

Energy-based surface contributions for interior acoustics -
A diagnosis tool to trace sound radiating surfaces

Caglar Gürbüz

Kurzfassung

Die Identifikation von lärmerzeugenden Strukturflächen spielt eine enorm wichtige Rolle im Entwurf von vibroakustischen Systemen, weil schwingende Strukturen Schall in ihre Umgebung emittieren. Insbesondere in der Fahrzeugakustik ist das Verfahren der Flächenbeitragsanalyse weit verbreitet, um diejenigen Flächen an der Karosserie zu identifizieren, die am meisten zum Schalldruckpegel an der Fahrerposition beitragen. Jedoch hat sich bisher keine Zielgröße für akustische Innenraumprobleme durchgesetzt. In klassischen Flächenbeitragsanalysen wird der Schalldruckpegel an der relevanten Position als Zielgröße herangezogen. Dies begünstigt allerdings mehrere Nachteile: Erstens ist der lokale Schalldruckpegel stark positionsabhängig. Die Identifikation von Flächenbeiträgen wird somit insbesondere in Frequenzbereichen und Regionen mit niedrigen Schalldrücken erschwert. Zweitens sind nach aktuellem Stand der Forschung Flächenbeiträge positiv oder negativ, wodurch akustische Kurzschlüsse begünstigt werden. Des Weiteren beschränken sich bestehende Verfahren auf einen einzelnen Auswertepunkt. Flächenbeiträge in Bezug auf ein gesamtes Volumen werden bisher nicht berücksichtigt. Letzlich leiden bestehende Verfahren darunter, dass das frequenzabhängige Helmholtz-Problem wiederholt für jede relevante Frequenz gelöst werden muss. Bei großen Frequenzbereichen oder feinen Frequenzauflösungen führt dies zu einem erheblich hohen Berechnungsaufwand.

Das Ziel dieser Arbeit ist die Entwicklung eines robusten numerischen Verfahrens für die effiziente Berechnung von Flächenbeiträgen in Innenräumen. Die Flächenbeitragsanalyse wird in eine Randelementeformulierung implementiert. Somit ist lediglich die geometrische Diskretisierung des umschließenden Randes erforderlich. Als Zielgröße wird die Schallenergie bzw. die Schallenergiedichte betrachtet. Somit wird nicht nur die Aussagekraft der Flächenbeiträge erhöht sondern auch der akustische Kurzschluss umgangen. Die Vorhersage der Flächenbeiträge ist besonders in Frequenzbereichen und Positionen mit geringen Schalldruckwerten robust. Darüber hinaus wird die energiebasierte Beitragsanalyse dahingehend erweitert, dass Flächenbeiträge bezüglich des eingeschlossenen Volumens ermittelt werden können. Zur Steigerung der Effizienz wird die Schallenergie im Volumen durch die Schallenergiedichten an einer Punkteschar approximiert. Schließlich wird ein Multi-Fidelity-Ansatz für akustische Simulationen mit der Randelementemethode vorgestellt, um Frequenzganganalysen von akustischen Systemen zu beschleunigen. Die Grundlage hierfür bilden Gaussprozesse, die wiederum auf dem Bayes'schen Wahrscheinlichkeitsprinzip basieren. Dadurch werden Unsicherheiten berücksichtigt, die beispielsweise durch beschränkte Information über die Modellparameter oder durch Fertigungstoleranzen auftreten können. Die in dieser Thesis entwickelten Verfahren werden anhand einer industriellen Problemstellung, nämlich dem niederfrequenten Dröhngeräusch in Fahrzeugen, validiert.

Insgesamt wird in dieser Doktorarbeit ein effizientes und robustes Diagnosewerkzeug für die Identifikation von schallerzeugenden Quellen auf schwingenden Oberflächen vorgestellt. Die Schallenergiedichte als kombinierte Druck-Schnelle Zielgröße ermöglicht dabei

tiefere Einblicke in das akustische Verhalten eines Systems. Darüber hinaus wird ein probabilistisches Verfahren für effiziente Frequenzganganalysen vorgestellt. Somit sind Vorhersagen über das Systemverhalten möglich, auch wenn nur Teilinformationen vorliegen. Dies ebnet den Weg für eine schnelle Entscheidungsfindung gerade in der frühen Entwicklungsphase.

Abstract

Owing to physical principles, sound is emitted from vibrating structures into the ambient fluid. The identification of vibrating patterns is thus an important aspect in the design of vibroacoustic systems. Particularly in the realm of automotive acoustics, the theory of contribution analysis is frequently used to retrieve chassis components contributing most to the sound pressure level at the driver's position. As a purely numerical method, contribution analyses allow to identify critical components in early design stages. However, research to date has not yet defined a suitable control objective for interior acoustic problems. In current contribution analysis methods, the sound pressure level at a certain position is used as a control objective, which implies a series of difficulties. Firstly, the sound pressure level is highly sensitive to the position of the relevant evaluation point. By this means, the identification of vibrating surfaces becomes particularly complicated in regions with low sound pressures. In addition to this, current techniques suffer from acoustic short circuits caused by bipolar surface contributions. Moreover, traditional methods are limited to contributing surfaces with respect to a single evaluation point. The surface contributions regarding the enclosed volume is not yet explored. Finally, the underlying acoustic problem involves the treatment of the frequency-dependent Helmholtz problem. To date, the Helmholtz equation is repetitively solved for each relevant frequency. This becomes extremely inefficient when broad frequency bands or fine frequency resolutions are analyzed.

This cumulative thesis introduces a robust and efficient method for contribution analyses in interior acoustics. It is embedded in a boundary element formulation and requires thus only a discretization of the enveloping surface. In the proposed method, the sound energy density is regarded as a control objective. This enables accurate and robust predictions even at frequency regimes and locations with low sound pressure levels. Moreover, the energy-based contribution analysis is extended to surface contributions regarding an entire volume. By interpreting the surface contributions to the energy density as integration points, the contributing surfaces related to the sound energy are efficiently obtained. On top of that, a multi-fidelity Gaussian process is developed for accelerated frequency sweep analyses. In the spirit of a Bayesian method, the proposed technique allows to account for uncertainties. This feature is of particular interest in early design phases, as it paves the way to consider uncertainties arising from limited knowledge on model parameters or tolerances due to manufacturing processes. To validate the proposed method, the low frequency booming noise problem occurring in vehicle cabins is analyzed throughout this thesis.

Taken together, this thesis presents an accurate and robust diagnosis tool to trace sound radiating sources on vibrating surfaces. By using the sound energy density as a control objective, a combined pressure-velocity quantity is introduced, which allows to gain deeper insight into the properties of the acoustic system. In addition to this, a probabilistic method is proposed for accelerated frequency sweep analyses enabling decision making processes under limited information.

Danksagung

An dieser Stelle möchte ich bei allen Menschen bedanken, die mich in meiner Zeit als Doktorand begleitet haben.

Zunächst bedanke ich mich bei Prof. Dr.-Ing. Steffen Marburg, meinem Doktorvater, für die Betreuung dieser Doktorarbeit. Ich danke dir Steffen, dass du mir den Freiraum gegeben hast, meine Ideen zu verwirklichen, und dass ich die Möglichkeiten hatte, meine Arbeit auf internationalen Konferenzen vorzustellen. Unsere zahlreichen Gespräche auf fachlicher und persönlicher Ebene werden mir immer als konstruktiver und angenehmer Austausch in Erinnerung bleiben.

I am very grateful to Prof. Efren Fernandez-Grande. Thank you for accepting my thesis as the second reviewer and for the fruitful discussions we occasionally had.

Thank you Prof. Phaedon-Stelios Koutsourelakis for chairing chair my PhD defense and for the friendly atmosphere.

Aus einstigen Kollegen wurden meine Freunde und daraus sogar unsere Hochzeitsgäste. Ein großes Dankeschön gebührt daher der Crew am Lehrstuhl. Danke euch, Elke und Martina, für eure Mühen und Geduld mit meinen Anträgen, die ich auch mal unmittelbar vor der Frist eingereicht habe. Danke auch an Alex, Simone, Bettina, Christopher und Marcus für eure stetige Hilfsbereitschaft. Vielen Dank an meine Ko-Autoren Felix, Jonas und Johannes für eure tatkräftige Unterstützung. Ganz besonders möchte ich bei Martin bedanken. Sei es bei der TM 3 oder bei unseren gemeinsamen Paper, ich konnte mich jederzeit auf dich verlassen. Ich denke, dass wir beide auf eine sehr gute Zusammenarbeit zurückblicken können. Ich bin euch allen herzlichst für die vielen wunderschönen Momente am Lehrstuhl dankbar. Es war mir ein großes Vergnügen mit euch zu arbeiten.

Der größte Dank gilt meiner Familie.

Meine liebe Sina, ich danke dir von Herzen für dein Vertrauen und für den Rückhalt, den du mir entgegengebracht hast. Du warst immer für mich da, wenn ich dich gebraucht habe. Ich bin unheimlich froh, dass du meine Ehefrau bist.

Meinen Eltern, Zehra und Mustafa, bin ich von Herzen dankbar. Auch in schweren Zeiten habt ihr euch für mich aufgeopfert und eure Bedürfnisse stets für meine Bildung zurückgestellt. Ich bin unglaublich stolz euer Sohn zu sein.

Mein letzter Dank gilt dem kleinsten in dieser Runde: unserem Sohn Carlo. Du bist der erste Tag für uns. Dein Papa macht jetzt Doktor.

List of publications

This cumulative thesis consists of the following three publications:

A C. Gurbuz, J.D. Schmid, M. Luegmair, and S. Marburg, "Energy density-based non-negative surface contributions in interior acoustics," *Journal of Sound and Vibration*, vol. 527, p. 116824, 2022.

B C. Gurbuz, and S. Marburg, "Efficient analysis of energy-based surface contributions for an entire acoustic cavity," *Journal of Theoretical and Computational Acoustics*, 2022, accepted for publication.

C C. Gurbuz, M. Eser, J. Schaffner, and S. Marburg, "A multi-fidelity Gaussian process for efficient frequency sweeps in the acoustic design of a vehicle cabin," *The Journal of the Acoustical Society of America*, vol. 153, no. 4, p. 2006, 2023.

The publications above are thoroughly presented in the remainder of this thesis. Beyond that, further journal and conference papers have been published in the course of this PhD program, which are not included in this thesis. These are the following:

- C. Gurbuz, F. Kronowetter, C. Dietz, M. Eser, J.M. Schmid, and S. Marburg, "Generative adversarial networks for the design of acoustic metamaterials," *The Journal of the Acoustical Society of America*, vol. 149, no. 2, p. 1162–1174, 2021.

- C. Gurbuz, M. Eser, J.D. Schmid, S. Marburg, and M. Luegmair, "Gaussian processes for transfer path analysis applied on vehicle body vibration problems," *SAE International Journal of Advances and Current Practices in Mobility*, vol. 5, p. 860–865, 2022.

- C. Gurbuz, and S. Marburg, "Energy-based non-negative surface contributions approximated for the volume of an inward radiating sphere," *Proceedings of the 24th International Congress on Acoustics*, 2022.

- C. Gurbuz, and S. Marburg, "Akustische Gütemaße in Innenräumen: Schallintensität und Schallenergien," *Fortschritte der Akustik-DAGA: 45. Jahrestagung für Akustik, 18.-21. März*, 2019.

Contents

1 Introduction

Exposure to noise is a growing public health concern worldwide and poses a major environmental problem. In their report in 2011, the World Health Organization Regional Office for Europe identified that noise is related to numerous human diseases. To quantify the health impact of noise, they have applied a disability-adjusted life-year criterion. For the European countries, they have calculated 61 000 years for ischaemic heart disease, 45 000 years for cognitive impairment of children, 903 000 years for sleep disturbance, 22 000 years for tinnitus, and 587 000 years for annoyance. This makes approximately 1 618 000 healthy life years per year that are lost due to noise. These observations indicate that there is an urgent need to address the health problems caused by noise [1].

According to physical principles, vibrating structures interacting with the ambient fluid lead to pressure perturbations, which result in emitted sound. While we perceive sound from musical instruments as pleasant, we typically consider sound emissions of modern industrial products disturbing or harmful. Specialists and researchers in that field, thus, aim to mitigate undesired sound emissions to reduce the impact on their environment. Vibrating structures as central noise mechanisms are omnipresent in the interior of modern transportation systems. A non-exhaustive list encompasses aircraft fuselages, train compartments, automotive passenger cabins, and passenger cabins of modern vertical take-off and landing aircraft. Consequently, identifying sound producing vibration patterns on the structural surface is of great interest [2, 3]. In engineering practice, experience has demonstrated that implementing noise mitigation techniques in the early design stages yields quieter and better products. Apparently, actions in the early phases lead to substantial cost benefits [4]. In early design stages, experts and practitioners can rarely apply experimental measurements to identify sound sources on surfaces, as product prototypes are seldom available in these stages. Numerical methods, on the other hand, allow the analysis of surface contributions for various configurations at the early design phase enabling a fast decision-making process. Regarding applications in exterior acoustics, the radiated sound intensity is widely adopted for evaluations of the sound emission level. However, an equivalent quantity needs to be established for interior acoustic problems. On top of that, specialists are challenged to make decisions under partial information, as early design candidates are subject to numerous uncertainties potentially arising from parameter variations or manufacturing tolerances.

The overarching aim of this thesis is to develop a powerful diagnosis tool to trace sound sources on vibrating structures. Therefore, a numerical contribution analysis method is implemented, which can be readily integrated into an early design phase of a product development cycle. Prior to the implementation, a control objective for interior acoustic problems is defined enabling an accurate and robust formulation for the contribution analysis. The proposed method is then extended from a single evaluation point to a series of evaluation points to recover surface contributions to the acoustic quantities in entire volumes. The low frequency booming noise problem in passenger car cabins is investigated for validation purposes. In the final step, a multi-fidelity modeling paradigm is adopted,

combining predictions of highly accurate but costly simulations with small-scale models, which might be less accurate but fast to obtain. In this way, a holistic approach is proposed to improve the efficiency in decision-making pipelines.

1.1 State of the art

This chapter is composed of two themed parts. The first part deals with the state of the art on sound source identification problems on vibrating surfaces. Over the past decades, various approaches have been proposed to identify sound producing surfaces:

- Near-field acoustic holography (NAH)
- Equivalent source methods (ESM)
- Inverse boundary element method (IBEM)
- The Helmholtz least-squares (HELS) method
- Surface and panel contribution analysis
- Supersonic and non-negative surface contributions

In the work [5], the developments in these topics are traced until 2004. The first subsection overviews existing research on NAH and ESM (Sec. 1.1.1). Previous studies in the IBEM and HELS are presented in Sec. 1.1.2. A detailed review of surface and panel contribution analysis methods is provided in Sec. 1.1.3, while Sec. 1.1.4 reviews studies on supersonic and non-negative intensity. The second part proceeds with the review on the state of the art of probabilistic surrogate modeling, including Gaussian processes in acoustics (Sec. 1.1.5) and multi-fidelity models in the context of fast frequency sweeps (Sec. 1.1.6).

1.1.1 Near-field acoustic holography and equivalent source methods

NAH provides an experimental technique that reconstructs a three-dimensional sound field based on pressure measurements on a two-dimensional surface. Researchers in that field refer to this surface as the hologram. The sound pressure on the hologram is used as a boundary condition for a known Green's function. The three-dimensional sound field is reconstructed by convolving the hologram data with the Green's function. Based on that solution, the vector-valued intensity field is obtained, which visualizes the energy flow within the structure [6, 7, 2]. This technique has been initially investigated on elementary geometries, e.g., of planar [6], cylindrical [8], and spherical shape [9] and then transferred to interior noise reduction problems in aircraft fuselages [10, 11]. For arbitrarily shaped surfaces, the boundary element method (BEM) has been incorporated in NAH schemes [12, 13]. NAH has been further improved by measuring the normal particle velocity instead of the sound pressure. In their article [14], Jacobsen and Liu have demonstrated that the particle velocity data provides a robust alternative to sound pressure measurements.

Another technique to recover sound sources involves the group of equivalent source methods (ESMs). In the ESM, a superposition of equivalent point sources is deployed at auxiliary positions to recover the sound radiation or scattering pattern of a structure [15]. The power of these sources is determined such that they fulfill the measured data. This results in an inverse problem, requiring special treatment of the ill-posed system matrix. In contrast to finite element or boundary element formulations, the vibrating structure is not discretized in the ESM. As such, the ESM designates a meshless method [16]. Due to their simplicity, ESMs have received considerable attention leading to numerous cross-sectional studies. For instance, it has been incorporated in the NAH to increase the efficiency in the recovery procedure [17]. Moreover, the ESM has been integrated into another holographic reconstruction framework to alleviate the singularities associated with the BEM system matrix [18]. In another study, the ESM has been integrated into an NAH scheme, where the measurements are obtained with particle velocity transducers [19]. In close analogy to [14], Zhang et al. identified that a velocity-based analysis is less sensitive than traditional pressure-based methods. The ESM has further demonstrated its effectiveness in sound field separation techniques. This technique is advantageous to mitigate the impact of perturbing sound sources [20]. In interior acoustics, a monopole-based ESM has been successfully applied in a source identification problem [21]. Further work has applied an extension to dipole equivalent sources to recover sound sources on a vibrating ship hull [22]. The review article [16] provides a detailed overview tracing the developments in ESMs until 2017. More recent studies focus on ESM-based holographic reconstructions at large scale. These involve sparse formulations to alleviate the ill-posed nature inherent to reconstruction methods [23, 24, 25, 26, 27, 28].

1.1.2 Inverse BEM and Helmholtz least-squares method

In general, the BEM is used to compute the radiated or scattered sound field from a vibrating structure. This procedure is also known as forward simulation. By reversing that step the backward simulation or the inverse problem is stated. Regarding the BEM, this means that the vibration pattern on a structure is computed by imposing a known sound field. From this, the concept of the IBEM has emerged. The initial study on IBEM can be traced back to 1992. In that work, the IBEM has been incorporated in an NAH method in order to recover sound sources on arbitrarily shaped structures [29]. Moreover, the IBEM has been applied to an interior vehicle noise problem. In that work, the velocity, the pressure and the sound power on an enveloping structure have been recovered by measuring the sound pressure inside the vehicle cabin [30]. The authors in the aforementioned studies have emphasized the ill-posed nature associated with the acoustic inverse problem. The reason for this is a singularity in the acoustic system matrix leading to non-physical results. In order to treat the ill-posed problem, regularization techniques have been thoroughly investigated. A non-exhaustive list of these methods includes the Tikhonov regularization [31, 12], the truncated singular value decomposition (SVD) [32, 33], and Krylov subspace iterative methods [13]. In a cross-sectional study [18], a hybrid IBEM and ESM approach is incorporated in an NAH. In the initial step, the limited number of measured data is enriched by sound field data from multiple equivalent sources. Based on the com-

bined data set, the vibration pattern is computed by means of the IBEM. Another research deals with the comparison between the IBEM and the ESM. The authors have favored the ESM, as the IBEM is associated with higher computational costs. The reason for this is that the IBEM system matrix assembly involves the numerical discretization of a boundary integral equation, while the system matrix related to the ESM is directly evaluated. Moreover, the authors have demonstrated that the ESM can achieve similar reconstruction errors for a specific choice of evaluation points [34]. For a detailed presentation of the fundamentals on IBEM-based NAH, the interested reader is referred to the work [35]. Modern research on IBEM also focuses on sparse regularization techniques. In a recent study, for instance, acoustic radiation modes have been effectively applied in a sparse formulation [36]. In sound source identification problems, the BEM is generally preferred to the finite element method (FEM). The reason for this is that the BEM only requires the numerical discretization of the surface, which is the relevant part of the structure in sound radiation and scattering problems. However, for the sake of completeness, it should be mentioned that research has been also conducted on the inverse FEM to recover sound sources in two-dimensional cavities [37, 38] and three-dimensional [39] aircraft fuselages.

Instead of solving the acoustic inverse problem, one could possibly think about optimizing the source parameters such that the measured data is fulfilled. This idea is central to the concept of the Helmholtz least-squares (HELS) method. In the HELS method, a spherical wave expansion is used to recover a sound field computed with the BEM [40, 41]. The method of least-squares is then applied to find the best fit of the wave expansion coefficients with respect to the measured sound pressure [42]. In the field of interior acoustics, the HELS method has been investigated for elementary sound sources such as cylinders and spheres [43]. Moreover, a combination of the NAH and the HELS method has been developed for a panel contribution analysis. In that study, the authors have focused on the sound power as a quality criterion [44].

1.1.3 Surface and panel contribution analysis

The first incidence of panel or surface contribution analysis in the scientific literature can be traced back to a research group around Ishiyama [45]. In 1988, the authors implemented ACOUST/BOOM, a BEM-based research code to compute the sound pressure radiated by a vibrating structure. The term 'BOOM' refers to booming noise, which designates the most disturbing noise in vehicle cabins. Booming noise generally occurs at frequencies up to $200\,\mathrm{Hz}$. In their method, the authors compute the sound pressure inside the domain by the product of the velocity excitation and a coefficient vector relating the transfer function from a boundary element to the sound pressure in the domain. They used the so-called contribution ratio as the control objective to perform the contribution analysis. The contribution ratio is defined by the ratio of sound pressure induced by one element to the total sound pressure [46].

Since then, the definition of the coefficient vector has evolved. For instance, Adey et al. [47] have introduced the term acoustic contributions to refer to that quantity. In addition, they have modified the coefficients by a correction factor to account for a phase

shift between the sound pressure on the boundary and the sound pressure at the internal point [48]. In another work [49], these transfer functions have been understood as sensitivities regarding the particle velocity. As such, the authors have introduced them as global acoustic sensitivities. Dong et al. [50] also support this view by interpreting the coefficient vector as sensitivities of the sound pressure at the evaluated position. In their work, the authors have developed a design sensitivity analysis based on the adjoint variable method. In 2000, a recorded patent popularized the term acoustic transfer vector [51]. Marburg [52, 53] provides a further definition of the coefficient vector, describing them as influence coefficients. While various definitions have been proposed, this thesis will use the term influence coefficients, as suggested by Marburg.

As already mentioned, contribution analysis has been of great interest in vehicle interior noise problems. For this reason, it has received considerable attention from developers of commercial software packages. The initial implementation of a panel contribution analysis can be traced back to SYSNOISE developed by Coyette [49, 54]. Since its release in 1993, it has been applied to numerous vehicle interior noise problems ranging from passenger [55], mini-bus [56], and tractor cabins [57]. Nowadays, SYSNOISE is part of Siemens Simcenter and runs under the name LMS Virtual Lab. Another implementation based on the equivalent radiated power (ERP) is supported in LS-DYNA [58]. COMSOL Multiphysics®, on the other hand, has implemented a panel contribution analysis based on the numerical Green's function. For a limited number of evaluation points, the authors have concluded that their method provides an efficient alternative to traditional techniques based on BEM or FEM [59].

Besides numerical methods, surface contributions have also been assessed with experimental methods. In close analogy to [45], Muhlmeier et al. have measured the ratio of the sound pressure of each chassis part with respect to the total sound pressure at the driver's seat [60]. In addition to the air-borne transfer function, structure-borne transfer paths have been considered by measuring the acceleration on various chassis panels [61]. Microflown Technologies has reported another experimental surface contribution analysis. In the first step, the transfer functions are measured from a monopole sound source located at the driver's position to reference microphones at the enveloping surfaces. Secondly, the particle velocity at the surfaces is measured during an operational state. Then, by assuming acoustic reciprocity, the contribution of each panel can be evaluated [62, 63]. In another study, De Bree and Basten replaced the microphones with particle velocity sensors in the reference measurement. The authors have indicated that the analysis procedure is less sensitive to environmental conditions when particle velocity sensors are used [64]. HEAD acoustics have developed a similar measurement technique based on the reversibility of the sound path. In contrast to traditional methods, where sensors are applied on each panel, the authors have sequentially analyzed the response of each panel [65].

1.1.4 Supersonic intensity and non-negative intensity

In a landmark study, Williams introduced the supersonic intensity (SSI) as a control objective for evaluating exterior acoustic problems [66]. As an alternative to the sound intensity,

the SSI considers only the radiation of supersonic wave components, as the subsonic wave components are evanescent in the near-field and are, thus, not contributing to the far-field. By applying the SSI, sound sources on vibrating structures can be directly identified, as the SSI filters out non-radiating wave components. Moreover, the SSI has been formulated for rectangular shaped structures, where the results were concurrent with fundamental corner and edge radiation modes of vibrating planar structures [67]. The SSI has been further extended to vibrating structures of arbitrary shapes [68]. In that study, the authors developed a BEM-based technique in which non-radiating wave components are filtered out using the SVD. Williams [2] uses the radiation circle to distinguish between subsonic and supersonic wave components. Wave components inside the radiation circle are defined as supersonic components. On the other hand, the evanescent subsonic wave components lie outside the radiation circle. However, a transformation to the wave number domain is required because the radiation circle is defined in that domain. To abridge that transformation, Fernandez-Grande et al. have introduced a spatial filter function to transfer the properties of the radiation circle to the spatial domain [69, 70].

Marburg et al. [71] have introduced another control objective related to exterior acoustics. The authors have formulated the non-negative intensity (NNI) with either zero or positive-only contributions. In this way, near-field cancellation effects due to alternating positive and negative signs are avoided. While Marburg et al. have initially focused on sound radiation problems, Liu et al. [72] have extended the NNI to sound scattering problems. Therefore, they computed the NNI on the scattering object and a different far-field receiver surface. In another study [73], the authors have demonstrated that the NNI can effectively determine the directivity of scattered sound waves. Since then, the NNI has been established as a viable control objective in multiple applications. For instance, Wilkes et al. [74] have implemented the NNI for fluid-structure interaction problems at large scale. Liu et al. [75] have used the NNI to reconstruct vibrating patterns on structures with inhomogeneous damping characteristics, while Karimi et al. have focused on systems that are excited by a turbulent boundary layer or a diffuse sound field [76]. In a more recent study, the NNI has been applied to identify the contributions from Antarctic krill to the scattered sound at the target strength of underwater objects [77].

In a cross-sectional study, Williams [78] has derived spatial convolution formulas based on hologram measurements to identify the NNI distributed on a vibrating planar surface. He has pointed out that by using a hologram with a combined microphone and velocity-probe measurements, a smooth intensity distribution can be recovered. Another work deals with the comparison between the SSI and the NNI [79]. The findings from the comparison suggest that both intensity quantities can be used as a viable control objective. A slightly deteriorated performance has been observed for the SSI at lower frequencies. However, this issue has been alleviated by introducing a cut-off coefficient to the spatial convolution formula. Another intensity-based control objective, the useful intensity, has been proposed by Correa and Tenenbaum [80]. Regarding the filtering step, the useful intensity relies on the acoustic radiation modes, whereas the NNI relies on the modal decompostion of the acoustic impedance matrix. As the acoustic radiation modes are closely related to the eigensolution of the acoustic impedance matrix, the useful intensity provides a similar approach to the NNI. The evidence reviewed here highly supports the

idea of an alternative control objective to the sound intensity. The SSI and NNI designate the most prominent approaches, as they avoid cancellation effects in the near-field. These studies outline an essential role for intensity formulas, as they provide efficient techniques to recover sound sources on vibrating structures.

Regarding interior acoustics, a similar control objective has yet to be established. While intensity-type quantities are suitable for outward-radiating problems, Koopmann and Fahnline suggest using the sound energy density as a control objective for inward-radiating problems [3]. Existing research on active noise control recognizes the vital role of sound energy densities. For instance, the sound energy density has been effectively applied to control sound in interior transmission problems [81, 82, 83]. Moreover, the sound energy density has been used as a control objective to treat the noise problem in coupled structural-acoustic cavities [84]. In another study, Sommerfeldt and Nashif [85] have demonstrated that an energy-based control system provides higher robustness than a pure pressure-based technique.

1.1.5 Gaussian processes in acoustics

Early examples of research on Gaussian processes (GPs) include problems in hyrdro-science [86] and geostatistics [87], where GPs have been adopted for interpolations of stochastically variable spatial data. In the early literature, however, the term kriging was used to refer to a GP. For a thorough review of kriging, particularly its origins, the interested reader is referred to [88, 89]. It is only since the works of Mackay [90] and Williams and Rasmussen [91] that the study of GPs has gained momentum. Since then, the term Gaussian process has been widely adopted. Modern studies on GPs involve their application for the solution of linear [92] as well as nonlinear, time-dependent partial differential equations [93].

Awareness of GPs in acoustics is relatively recent, having possibly first been described by Hensman et al. [94], who have implemented GPs to localize sound producing surfaces on an aerospace component. In the field of acoustical oceanography, a great deal of research on GPs has focused on identifying and localizing sources producing sound in the ocean [95, 96, 97, 98, 99]. GPs have been further applied to estimate the direction of arrival [100] and to reduce uncertainties in the predicted sound field [101]. Beyond that, GPs have been specialized for sound field reconstruction problems by introducing a plane wave expansion [102] or the inhomogeneous solution of the Helmholtz equation to the kernel function [103, 104]. More recent research on GPs involves their application as a surrogate in transfer path analyses [105] and identifying rock cracks based on the emitted sound [106].

1.1.6 Multi-fidelity modeling and fast frequency sweeps

Craig et al. [107] have initially articulated the concept of a multi-fidelity model. Multi-fidelity modeling has been then popularized by Kennedy and O'Hagan [108]. In the early

literature, research on multi-fidelity modeling has focused on the approximation of the output of a complex simulation model by using small-scale models, which are fast to evaluate. In particular, Kennedy and O'Hagan have defined a multi-fidelity model as a combination of a model with the highest possible fidelity and its lower fidelity version. For that purpose, they introduced the term autoregressive to refer to their multi-fidelity concept. In their multi-fidelity model, they have used GPs as surrogates for the different fidelity levels, which are linearly correlated. That idea has been extended to multiple fidelity levels utilizing a recursive formulation for the autoregressive model [109, 110]. In more recent studies, multi-fidelity GPs have been applied for the inference of random fields [111] and in the design optimization of super-cavitating hydrofoils [112, 113].

Multi-fidelity models relying on the formulation of Kennedy and O'Hagan, see [108], assume a linear correlation between the fidelity levels. Several studies have explored the extension of multi-fidelity models to nonlinearly correlated levels to assess more complex correlations between the fidelity levels. For instance, by stacking GPs for each fidelity level, deep GPs have been implemented, allowing nonlinear correlations between the levels [114]. Deep GPs have been validated on discontinuous correlation functions [115, 116] and applied to a real-world problem combining numerical and experimental data [117]. As an alternative to GPs, neural networks have been used as surrogates in a multi-fidelity method [118]. Using this approach, nonlinearities in the correlation functions have also been effectively captured [119]. Recent evidence demonstrates that multi-fidelity models are effective in structural health monitoring applications [120, 121].

In general, multi-fidelity models allow approximations of a function by combining the results of computational costly simulations with solutions of small-scale simulations. This concept can be transferred to the efficient solution of parameter-dependent problems, for which multi-fidelity models have demonstrated their effectiveness, see [118]. Turning now to the field of acoustics, the solution of the Helmholtz equation with the BEM implicitly depends on the frequency. Thus, the solution in a specific frequency range requires repetitive assemblies of the system matrices. So far, this problem has been only treated with deterministic methods. For instance, a greedy reduce basis method has been developed for vibroacoustic problems [122, 123]. In another approach, the BEM matrices are decoupled from the frequency. The size of the remaining frequency-independent BEM matrices is then reduced through model order reduction methods. This technique has been successfully applied on acoustic [124, 125] as well as on coupled structural acoustic systems [126, 127].

1.2 Contributions and accomplishments

The present cumulative thesis contributes to the research areas of computational acoustics and uncertainty quantification. It comprises three peer-reviewed publications, which provide efficient and robust techniques to tackle the vehicle interior noise problem stated in the Introduction, see Chapter 1. The remaining part of this thesis proceeds by referring to the publications as Paper A, Paper B, and Paper C. The key contributions and accomplishments of this thesis are summarized as follows:

- In Paper A, the surface contributions based on sound energies are introduced. In particular, the derivation of their formulation and implementation in a BEM framework is presented. The proposed method is validated with an industrial application, the vehicle interior noise problem, with booming noise representing the most prominent source of disturbance.

- While the previous paper focuses on surface contributions regarding a single evaluation point, Paper B provides an extension to multiple field points leading to an approximation of the energy-based surface contributions concerning the entire cavity. The proposed method is studied on two numerical examples, the inward radiating sphere problem and the vehicle cabin noise problem.

- The proposed methods in the first two publications rely on the solution of the Helmholtz equation for each frequency. Thus, Paper C presents an approximation of the frequency sweep for a broad frequency range. For this purpose, a multi-fidelity Gaussian process has been developed and validated for the vehicle cabin noise problem. Moreover, the accuracy and the computational runtime of the proposed approximation has been compared to the fully resolved frequency sweep with the BEM.

Chapter 3 provides detailed summaries of the publications Paper A, Paper B, and Paper C and an accurate description of the contributions of all authors. The reprints of the publications are given in Appendix A.

2 Energy-based surface contributions and multi-fidelity Gaussian processes

This chapter is organized as follows: The first part deals with the interior acoustic problem in the frequency domain governed by the Helmholtz equation, see Sec. 2.1. The next section provides the fundamentals of the BEM in acoustics (Sec. 2.2). The third section, Sec. 2.3, is concerned with the evaluation of acoustic quantities within the computational domain. This involves evaluations at single and multiple field points. Sec. 2.4 introduces the energy quantities in sound waves. In Sec. 2.5, the formulation of the energy-based surface contributions is presented. The theoretical background on GPs is outlined in the following section, Sec. 2.6. The final section in this chapter, Sec. 2.7 involves the formulation of multi-fidelity models using GPs.

2.1 Acoustic Helmholtz equation

In the linear acoustic theory, sound waves are constituted by small perturbations of the sound pressure and density compared to their ambient values. In addition, it is assumed that the ambient flow can be neglected. By this means, the propagation of sound is expressed by the acoustic wave equation [128]

$$\boldsymbol{\nabla}^2 \tilde{p}(\vec{\boldsymbol{x}},t) = \frac{1}{c_0^2}\frac{\partial^2 \tilde{p}(\vec{\boldsymbol{x}},t)}{\partial t^2} \qquad \vec{\boldsymbol{x}} \in \Omega \subset \mathbb{R}^3 \tag{2.1}$$

with the sound pressure $\tilde{p}(\vec{\boldsymbol{x}},t)$ and the speed of sound c_0 in the ambient fluid. The acoustic wave equation underlies the fundamental principles in continuum mechanics, such as conservation of mass, balance of momentum, and the constitutive equation. For details on the derivation of the wave equation, the interested reader is referred to [128, 129].

By assuming a time-harmonic sound pressure, the concept of separation of variables can be applied. This is expressed by

$$\tilde{p}(\vec{\boldsymbol{x}},t) = \Re\left\{ p(\vec{\boldsymbol{x}})\mathrm{e}^{-\mathrm{i}\omega t} \right\} \tag{2.2}$$

with $\mathrm{i} = \sqrt{-1}$ and $\omega = 2\pi f$ denoting the imaginary unit and the angular frequency. Substituting Eq. (2.2) in Eq. (2.1) yields the three-dimensional Helmholtz equation describing the propagation of sound waves in the frequency domain

$$\boldsymbol{\nabla}^2 p(\vec{\boldsymbol{x}}) + k^2 p(\vec{\boldsymbol{x}}) = 0 \qquad \vec{\boldsymbol{x}} \in \Omega \subset \mathbb{R}^3, \tag{2.3}$$

with $k = \omega/c$ denoting the wave number. In the scope of this work, the focus is on interior acoustic problems. A schematic overview of an interior Helmholtz problem is depicted in Fig. 1.
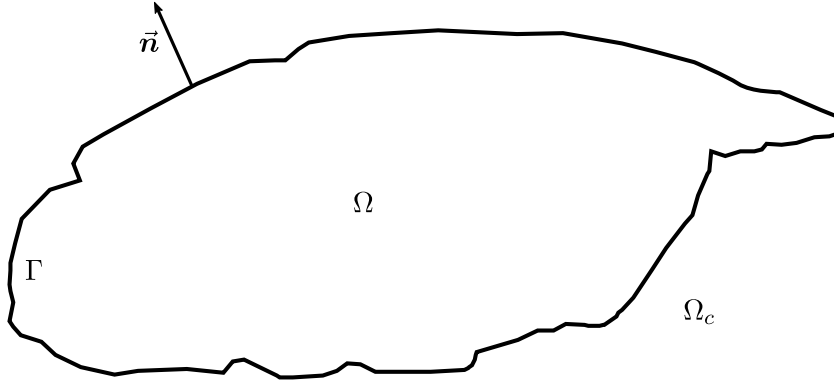

Figure 1: Definition of an interior acoustic problem. The computational acoustic domain Ω is enclosed by its boundary Γ. The normal vector $\vec{n}$ points outward into the complementary domain Ω_c. This figure is adopted from [130].

For the solution of the Helmholtz equation, boundary conditions need to be satisfied. In acoustics, Robin boundary conditions are particularly important, as they allow to model absorbing behavior on the boundaries. The Robin boundary condition is stated as

$$v_f(\vec{x}) - v_s(\vec{x}) = Y(\vec{x})p(\vec{x}) \qquad \vec{x} \in \Gamma \subset \mathbb{R}^2, \tag{2.4}$$

with the normal fluid particle velocity $v_f(\vec{x})$, the normal structural particle velocity $v_s(\vec{x})$, and the boundary admittance $Y(\vec{x})$. Note that, for $Y(\vec{x}) = 0$, the Robin boundary condition degrades to a Neumann boundary condition. The linearized Euler's equation relates the fluid particle velocity $v_f(\vec{x})$ to the derivative of the sound pressure in normal direction

$$v_f(\vec{x}) = \frac{1}{i\omega\rho_0}\frac{\partial p(\vec{x})}{\partial n(\vec{x})} \qquad \vec{x} \in \Gamma \subset \mathbb{R}^2 \tag{2.5}$$

with ρ_0 denoting the density of the ambient fluid [131].

2.2 Boundary element method in acoustics

The method of weighted residuals is applied to obtain the weak formulation of the Helmholtz equation (Eq. 2.3). This implies the multiplication of the Helmholtz equation with the test function $\chi(\vec{x})$ and the integration over the domain Ω

$$\int_\Omega \chi(\vec{x})\left[\boldsymbol{\nabla}^2 p(\vec{x}) + k^2 p(\vec{x})\right]\mathrm{d}\Omega = 0. \tag{2.6}$$

A double partial integration of Eq. (2.6) then yields

$$\int_\Gamma \mathrm{i}\omega\rho_0\chi(\vec{x})v_f(\vec{x}) - p(\vec{x})\frac{\partial\chi(\vec{x})}{\partial n(\vec{x})}\,\mathrm{d}\Gamma + \int_\Omega p(\vec{x})\left[\boldsymbol{\nabla}^2\chi(\vec{x}) + k^2\chi(\vec{x})\right]\mathrm{d}\Omega = 0. \tag{2.7}$$

Eq.(2.7) consists of one boundary integral and one domain integral. By substituting the test function with the fundamental solutions $G(\vec{x},\vec{y})$, the domain integral is rewritten as an integral-free term. The fundamental solutions $G(\vec{x},\vec{y})$ satisfy

$$\boldsymbol{\nabla}^2G(\vec{x},\vec{y}) + k^2G(\vec{x},\vec{y}) = -\delta(\vec{x},\vec{y}), \tag{2.8}$$

where $\delta(\vec{x},\vec{y})$ denotes the Dirac function. The free space Green's function $G(\vec{x},\vec{y})$ relates the sound pressure at the field point $\vec{x}$ to a monopole source located in $\vec{y}$ in a free-field environment. For three-dimensional acoustic fields, the Green's function is specified by

$$G(\vec{x},\vec{y}) = \frac{1}{4\pi}\frac{\mathrm{e}^{\mathrm{i}kr(\vec{x},\vec{y})}}{r(\vec{x},\vec{y})} \qquad \vec{x},\vec{y}\in\mathbb{R}^3 \tag{2.9}$$

with the Euklidean distance $r(\vec{x},\vec{y}) = |\vec{x}-\vec{y}|$ between the field point $\vec{x}$ and the source point $\vec{y}$. Note that the positive exponent assures outward propagating sound waves [128].

With the property in Eq. (2.8), the domain integral term in Eq. (2.7) is reformulated as

$$\int_\Omega p(\vec{x})\left[\boldsymbol{\nabla}^2G(\vec{x},\vec{y}) + k^2G(\vec{x},\vec{y})\right]\mathrm{d}\Omega = \int_\Omega p(\vec{x})\left[-\delta(\vec{x},\vec{y})\right]\mathrm{d}\Omega = -c(\vec{y})p(\vec{y}) \tag{2.10}$$

with the coefficient $c(\vec{y})$ denoting a geometric quantity, which characterizes the contour of the boundary at $\vec{y}$. On smooth surfaces, for instance, the coefficient $c(\vec{y})$ adopts to 0.5. By introducing Eq. (2.10) in Eq. (2.7), the Kirchhoff-Helmholtz boundary integral equation is formulated as

$$c(\vec{y})p(\vec{y}) + \int_\Gamma \frac{\partial G(\vec{x},\vec{y})}{\partial n(\vec{x})}p(\vec{x})\,\mathrm{d}\Gamma(\vec{x}) = \mathrm{i}\omega\rho_0\int_\Gamma G(\vec{x},\vec{y})v_f(\vec{x})\,\mathrm{d}\Gamma(\vec{x}) \tag{2.11}$$

The term representation formula is also commonly used for Eq. (2.11). This definition highlights that the sound pressure can be evaluated at an arbitrary position in Ω or Γ by only considering the solution on the boundary. Prior to the discretization step, the Robin boundary condition posed in Eq. (2.4) is included in the Kirchhoff-Helmholtz boundary integral equation. The resulting equation then reads

$$c(\vec{y})p(\vec{y}) + \int_\Gamma \left[\frac{\partial G(\vec{x},\vec{y})}{\partial n(\vec{x})} - \mathrm{i}\omega\rho_0 G(\vec{x},\vec{y})Y(\vec{x})\right]p(\vec{x})\,\mathrm{d}\Gamma(\vec{x}) = \mathrm{i}\omega\rho_0\int_\Gamma G(\vec{x},\vec{y})v_s(\vec{x})\,\mathrm{d}\Gamma(\vec{x}). \tag{2.12}$$

For the boundary element formulation, the method of weighted residuals is applied once again to Eq. (2.12). In the scope of this work, we use the collocation method to discretize the weak formulation of Eq. (2.12). This means that the additionally introduced test functions are substituted by the Dirac function $\delta(\vec{x},\vec{z})$, where $\vec{z}$ denotes the location of the collocation point. In this way, the boundary integral equation is satisfied at a finite number

of collocation points [128].

In the discretization step, approximation functions for the sound pressure, the structural particle velocity, and the boundary admittance are introduced

$$p(\vec{x}) = \sum_{l=1}^{N} \varphi_l(\vec{x}) p_l = \boldsymbol{\varphi}^{\mathsf{T}}(\vec{x}) \boldsymbol{p}, \tag{2.13}$$

$$v_s(\vec{x}) = \sum_{j=1}^{\bar{N}} \bar{\varphi}_j(\vec{x}) v_{sj} = \bar{\boldsymbol{\varphi}}^{\mathsf{T}}(\vec{x}) \boldsymbol{v_s}, \tag{2.14}$$

$$Y(\vec{x}) = \sum_{k=1}^{\tilde{N}} \tilde{\varphi}_k(\vec{x}) Y_k = \tilde{\boldsymbol{\varphi}}^{\mathsf{T}}(\vec{x}) \boldsymbol{Y}, \tag{2.15}$$

where $\boldsymbol{p}$, $\boldsymbol{v_s}$, and $\boldsymbol{Y}$ denote the discrete sound pressure, the discrete structural particle velocity, and the discrete boundary admittance at the position $\vec{x}$. The number of the basis functions φ, $\bar{\varphi}$, and the $\tilde{\varphi}$ are represented by N, $\bar{N}$, and $\tilde{N}$, respectively. In practice, boundary elements with piecewise discontinuous polynomial functions are widely adopted for the approximation of acoustic quantities. In that case, it can be assumed that $N = \bar{N} = \tilde{N}$ with N representing the number of degrees of freedom. As a consequence, the basis functions are assumed to be identical, i.e., $\varphi = \bar{\varphi} = \tilde{\varphi}$. For more details on the derivation of discontinuous boundary elements, the interested reader is referred to [132, 133].

By applying the collocation method and introducing the discrete representation of the physical quantities, the integral equation adapts to

$$c(\vec{z_l}) p_l + \int_{\Gamma} \left\{ \frac{\partial G(\vec{x}, \vec{z_l})}{\partial n(\vec{x})} - \mathrm{i}\omega\rho_0 G(\vec{x}, \vec{z_l}) \left[\sum_{j=1}^{N} \varphi_j(\vec{x}) Y_j \right] \right\} \left[\sum_{k=1}^{N} \varphi_k(\vec{x}) p_k \right] \mathrm{d}\Gamma(\vec{x})$$

$$= \mathrm{i}\omega\rho_0 \int_{\Gamma} G(\vec{x}, \vec{z_l}) \left[\sum_{m=1}^{N} \varphi_m(\vec{x}) v_{sm} \right] \mathrm{d}\Gamma(\vec{x}). \tag{2.16}$$

Note that the first term in the equation above is analytically integrated according to the relation in Eq. (2.10). After rearranging this equation, the matrix of the single layer potential is introduced as

$$g_{lj} = \mathrm{i}\omega\rho_0 \int_{\Gamma} G(\vec{x}, \vec{z_l}) \varphi_j(\vec{x}) \mathrm{d}\Gamma(\vec{x}). \tag{2.17}$$

Analogously, the matrix of the double layer potential and the integral-free term are expressed by

$$h_{lj} = c(\vec{z_l}) \delta_{lj} + \int_{\Gamma} \frac{\partial G(\vec{x}, \vec{z_l})}{\partial n(\vec{x})} \varphi_j(\vec{x}) \mathrm{d}\Gamma(\vec{x}). \tag{2.18}$$

By this means, the acoustic linear systems of equations can be formulated in matrix form

$$[\mathbf{H}(\omega) - \mathbf{G}(\omega)\mathbf{Y}(\omega)] \, \mathbf{p}(\omega) = \mathbf{G}(\omega)\mathbf{v}_s(\omega) \tag{2.19}$$

with the complex-valued system matrices $\mathbf{G}(\omega)$ and $\mathbf{H}(\omega)$, which are neither positive definite nor Hermitian. The boundary admittance matrix $\mathbf{Y}(\omega)$ contains only diagonal entries

for constant discontinuous approximation functions. The notation of the system matrices with ω as an argument highlights that these matrices implicitly depend on the frequency. As such, they have to be assembled for each discrete frequency. The sound pressure solution becomes, thus, frequency-dependent. For frequency sweep analyses, the linear system of equations in Eq. (2.19) has to be evaluated for each discrete frequency within the frequency range of interest [131].

2.3 Evaluation on single and multiple field points

Once the acoustic linear system of equations in Eq. (2.19) is solved, the sound pressure can be obtained at field points inside the acoustic domain, i.e., $\vec{y} \in \Omega$. For the computation of the sound pressure at a single field point, the representation formula in Eq. (2.11) is adapted to

$$p_i(\vec{y}) = i\omega\rho_0 \int_\Gamma G(\vec{x}, \vec{y}) v_s(\vec{x}) \, d\Gamma(\vec{x}) - \int_\Gamma \left[\frac{\partial G(\vec{x}, \vec{y})}{\partial n(\vec{x})} - i\omega\rho_0 \, G(\vec{x}, \vec{y}) Y(\vec{x}) \right] p(\vec{x}) \, d\Gamma(\vec{x}). \tag{2.20}$$

The subscript i denotes that the sound pressure is evaluated at an interior field point. Note that the integral-free term $c(\vec{y})$ equals to one in the equation above, as the field point $\vec{y}$ is located inside the acoustic domain Ω. In matrix form, Eq. (2.20) reads

$$p_i(\vec{y}) = \boldsymbol{g}^\mathsf{T}(\vec{y}) \boldsymbol{v}_s - \left[\boldsymbol{h}^\mathsf{T}(\vec{y}) - \boldsymbol{g}^\mathsf{T}(\vec{y}) \boldsymbol{Y} \right] \boldsymbol{p} \tag{2.21}$$

with the boundary integral operators $\boldsymbol{g}(\vec{y})$ and $\boldsymbol{h}(\vec{y})$ expressed as

$$g_l(\vec{y}) = i\omega\rho_0 \int_\Gamma G(\vec{x}, \vec{y}) \varphi_l \, d\Gamma(\vec{x}), \tag{2.22}$$

$$h_l(\vec{y}) = \int_\Gamma \frac{\partial G(\vec{x}, \vec{y})}{\partial n(\vec{x})} \varphi_l \, d\Gamma(\vec{x}). \tag{2.23}$$

The operators $\mathbf{g}(\vec{y})$ and $\mathbf{h}(\vec{y})$ can be understood as rows of the system matrices $\mathbf{G}(\omega)$ and $\mathbf{H}(\omega)$ with the field point $\vec{y}$ treated as a collocation point. By inserting the solution from Eq. (2.19) in Eq. (2.21), all matrix-vector products involve the multiplication with the structural particle velocity vector v_s. The sound pressure at a field point can then be equivalently expressed by

$$p_i(\vec{y}) = \left\{ \mathbf{g}^\mathsf{T}(\vec{y}) - \left[\mathbf{h}^\mathsf{T}(\vec{y}) - \mathbf{g}^\mathsf{T}(\vec{y}) \mathbf{Y} \right] (\mathbf{H} - \mathbf{GY})^{-1} \mathbf{G} \right\} \mathbf{v}_s = \mathbf{b}^\mathsf{T}(\vec{y}) \mathbf{v}_s \tag{2.24}$$

where all matrices are comprised in $\mathbf{b}(\vec{y})$, which is of size $N \times 1$. This quantity denotes the influence coefficients of the structural particle velocity regarding the sound pressure at the field point $\vec{y}$. In the literature, the term acoustic transfer vector is commonly used to refer to that quantity [131].

By applying the linearized Euler equation (Eq. (2.5)) on Eq. (2.20), the fluid particle veloc-

ity can also be evaluated at a field point inside the domain Ω [134]

$$\vec{v}_i(\vec{y}) = \int_\Gamma \boldsymbol{\nabla} G(\vec{x}, \vec{y}) v_s(\vec{x}) \mathrm{d}\Gamma(\vec{x}) - \left[\int_\Gamma \boldsymbol{\nabla} \frac{1}{\mathrm{i}\omega\rho_0} \frac{\partial G(\vec{x}, \vec{y})}{\partial n(\vec{x})} - \boldsymbol{\nabla} G(\vec{x}, \vec{y}) Y(\vec{x}) \right] p(\vec{x}) \mathrm{d}\Gamma(\vec{x}). \tag{2.25}$$

Note that the field point particle velocity $\vec{v}_i(\vec{y})$ is a vector-valued quantity, since it is defined in three spatial directions $\{x, y, z\}$. For the sake of compactness, the matrix form is also introduced for the field point particle velocity

$$\vec{v}_i(\vec{y}) = \left\{ \tilde{\mathbf{g}}^\mathsf{T}(\vec{y}) - \left[\tilde{\mathbf{h}}^\mathsf{T}(\vec{y}) - \tilde{\mathbf{g}}^\mathsf{T}(\vec{y}) \mathbf{Y} \right] (\mathbf{H} - \mathbf{GY})^{-1} \mathbf{G} \right\} \mathbf{v}_s = \tilde{\mathbf{b}}^\mathsf{T}(\vec{y}) \mathbf{v}_s \tag{2.26}$$

with the boundary integral operators related to the internal fluid particle velocity

$$\tilde{g}_l(\vec{y}) = \int_\Gamma \boldsymbol{\nabla} G(\vec{x}, \vec{y}) \varphi_l \, \mathrm{d}\Gamma(\vec{x}), \tag{2.27}$$

$$\tilde{h}_l(\vec{y}) = \frac{1}{\mathrm{i}\omega\rho_0} \int_\Gamma \frac{\partial G(\vec{x}, \vec{y})}{\partial n(\vec{x})} \varphi_l \, \mathrm{d}\Gamma(\vec{x}). \tag{2.28}$$

In close analogy to Eq. (2.24), $\tilde{\mathbf{b}}(\vec{y})$ refers to the particle velocity-related influence coefficients. More specifically, this quantity refers to the sensitivities of the field point particle velocity regarding the structural particle velocity. As opposed to that, the quantity $\mathbf{b}(\vec{y})$ is understood as the sensitivities of the field point sound pressure with respect to the structural particle velocity. Since the field point particle velocity is defined in three spatial directions, $\tilde{\mathbf{b}}(\vec{y})$ is of size $N \times 3$ [130].

For the evaluation of the sound pressure on multiple field points, Eq. (2.24) is modified to

$$p_i(\vec{y}_j) = \mathrm{i}\omega\rho_0 \int_\Gamma G(\vec{x}, \vec{y}_j) v_s(\vec{x}) \mathrm{d}\Gamma(\vec{x}) - \int_\Gamma \left[\frac{\partial G(\vec{x}, \vec{y}_j)}{\partial n(\vec{x})} - \mathrm{i}\omega\rho_0 G(\vec{x}, \vec{y}_j) Y(\vec{x}) \right] p(\vec{x}) \mathrm{d}\Gamma(\vec{x}) \tag{2.29}$$

with the index $j = 1, 2, ..., N_p$ denoting the identity of the field point. The total number of field points is represented by N_p. Analogously, Eq. (2.29) can be expressed in a compact matrix form

$$p_i(\vec{y}_j) = \left\{ \mathbf{g}_j^\mathsf{T}(\vec{y}_j) - \left[\mathbf{h}_j^\mathsf{T}(\vec{y}_j) - \mathbf{g}_j^\mathsf{T}(\vec{y}_j) \mathbf{Y} \right] (\mathbf{H} - \mathbf{GY})^{-1} \mathbf{G} \right\} \mathbf{v}_s = \mathbf{b}_j^\mathsf{T}(\vec{y}_j) \mathbf{v}_s \tag{2.30}$$

wit the sound pressure-related influence coefficients $\mathbf{b}_j(\vec{y}_j)$ at multiple field points. Since $\mathbf{b}_j(\vec{y}_j)$ refers to N_p field points, it is of size $N \times N_p$. The particle velocity at multiple field points can be obtained in a similar way. For this purpose, Eq. (2.25) adapts to

$$\vec{v}_i(\vec{y}_j) = \int_\Gamma \boldsymbol{\nabla} G(\vec{x}, \vec{y}_j) v_s(\vec{x}) \mathrm{d}\Gamma(\vec{x}) - \left[\int_\Gamma \boldsymbol{\nabla} \frac{1}{\mathrm{i}\omega\rho_0} \frac{\partial G(\vec{x}, \vec{y}_j)}{\partial n(\vec{x})} - \boldsymbol{\nabla} G(\vec{x}, \vec{y}_j) Y(\vec{x}) \right] p(\vec{x}) \mathrm{d}\Gamma(\vec{x}). \tag{2.31}$$

In compact matrix form, this equation reads

$$\vec{v}_i(\vec{y}_j) = \left\{ \tilde{\mathbf{g}}_j^\top(\vec{y}_j) - \left[\tilde{\mathbf{h}}_j^\top(\vec{y}_j) - \tilde{\mathbf{g}}_j^\top(\vec{y}_j)\mathbf{Y} \right] (\mathbf{H} - \mathbf{GY})^{-1}\mathbf{G} \right\} \mathbf{v}_s = \tilde{\mathbf{b}}_j^\top(\vec{y}_j)\mathbf{v}_s, \qquad (2.32)$$

where $\tilde{\mathbf{b}}_j(\vec{y}_j)$ denotes the particle velocity-related influence coefficients regarding a set of field points. For multiple field points, the size of $\tilde{\mathbf{b}}_j(\vec{y}_j)$ adopts to $N \times 3N_p$ [139].

2.4 Energy in sound waves

For sound waves propagating in fluids, energy appears in two forms [129]: potential and kinetic energy. The potential sound energy designates the stored energy due to the compression of the fluid particles. It is formulated as

$$E_p = \frac{1}{2\rho_0 c_0^2} \int_\Omega p(\vec{y})p^*(\vec{y})\,\mathrm{d}\Omega, \qquad (2.33)$$

where $()^*$ denotes the conjugate complex operation. As such, the potential sound energy is proportional to the sound pressure. The kinetic sound energy, on the other hand, is determined by the motion of the particles. It depends on the fluid particle velocity and is expressed by

$$E_k = \frac{\rho_0}{4} \int_\Omega \vec{v}_f(\vec{y}) \cdot \vec{v}_f^*(\vec{y})\,\mathrm{d}\Omega. \qquad (2.34)$$

The total sound energy transported in sound waves is then defined by the sum of both energy forms

$$E_t = E_p + E_k = \frac{1}{2\rho_0 c_0^2} \int_\Omega p(\vec{y})p^*(\vec{y})\,\mathrm{d}\Omega + \frac{\rho_0}{4} \int_\Omega \vec{v}_f(\vec{y}) \cdot \vec{v}_f^*(\vec{y})\,\mathrm{d}\Omega. \qquad (2.35)$$

As an energy quantity, the unit of the sound energy is $[\mathrm{kg\,m^2/s^2}] = [\mathrm{J}]$.

The sound energy densities are derived by referencing the sound energy to a unit volume. For instance, the potential sound energy density at the position $\vec{y}$ reads

$$e_p(\vec{y}) = \frac{1}{2\rho_0 c_0^2} p_i^*(\vec{y})p_i(\vec{y}). \qquad (2.36)$$

Analogously, the kinetic sound energy density at $\vec{y}$ is expressed by

$$e_k(\vec{y}) = \frac{\rho_0}{4} \vec{v}_i^*(\vec{y})\vec{v}_i(\vec{y}). \qquad (2.37)$$

The total sound energy density composed by the sum of both energy density forms is

then formulated as

$$e_t(\vec{\boldsymbol{y}}) = e_p(\vec{\boldsymbol{y}}) + e_k(\vec{\boldsymbol{y}}) = \frac{1}{2\rho_0 c_0^2}\, p_i^*(\vec{\boldsymbol{y}}) p_i(\vec{\boldsymbol{y}}) + \frac{\rho_0}{4}\, \vec{v}_i^*(\vec{\boldsymbol{y}}) \vec{v}_i(\vec{\boldsymbol{y}}). \qquad (2.38)$$

As the sound energy densities in Eqs. (2.36)–(2.38) are defined at the field point $\vec{y}$, the sound pressure and the particle velocity at the same field point are used. Due to the reference to a unit volume, the sound energy density has the unit $[\mathrm{kg/ms^2}]$. Note that the sound energy, as well as the sound energy density, are real-valued quantities [130].

2.5 Surface contributions based on sound energy

Turning now to the contribution analysis, we initially introduce the formulation of the surface contributions for a single evaluation point. For this purpose, the sound energy densities at the evaluation point are used as control objectives. By substituting the field point sound pressure in Eq. (2.36) with Eq. (2.24), the potential energy density can be equivalently expressed by

$$e_p = \frac{1}{2\rho_0 c_0^2}\, p_i^* p_i = \frac{1}{2\rho_0 c_0^2}(\mathbf{b}^{\mathsf{T}}\mathbf{v}_s)^*(\mathbf{b}^{\mathsf{T}}\mathbf{v}_s) = \frac{1}{2\rho_0 c_0^2}\mathbf{v}_s^{\mathsf{H}}\left(\mathbf{b}^*\mathbf{b}^{\mathsf{T}}\right)\mathbf{v}_s = \mathbf{v}_s^{\mathsf{H}}\mathbf{A}_p\mathbf{v}_s \qquad (2.39)$$

with $()^{\mathsf{H}}$ representing the complex conjugate operation. The matrix $\mathbf{A}_p$, composed of the dyadic product of the influence coefficients $\mathbf{b}$, denotes the coupling matrix related to the potential energy density. The rank of $\mathbf{A}_p$ equals to one when the surface contributions are evaluated for a single field point. For the sake of conciseness, the dependence on $\vec{y}$ is omitted here. In close analogy, the kinetic energy density in Eq. (2.37) can be reformulated by using the expression of the field point particle velocity in Eq. (2.25)

$$e_k = \frac{\rho_0}{4}\, \vec{v}_i^*\vec{v}_i = \frac{\rho_0}{4}(\tilde{\mathbf{b}}^{\mathsf{T}}\mathbf{v}_s)^*(\tilde{\mathbf{b}}^{\mathsf{T}}\mathbf{v}_s) = \frac{\rho_0}{4}\mathbf{v}_s^{\mathsf{H}}\left(\tilde{\mathbf{b}}^*\tilde{\mathbf{b}}^{\mathsf{T}}\right)\mathbf{v}_s = \mathbf{v}_s^{\mathsf{H}}\mathbf{A}_k\mathbf{v}_s, \qquad (2.40)$$

where $\mathbf{A}_k$ denotes the coupling matrix related to the kinetic energy density. Since the field point particle velocity is defined for three spatial directions, the matrix $\mathbf{A}_k$ is of rank three. Consequently, the total sound energy density is obtained by computing the sum of Eq. (2.39) and Eq. (2.40)

$$e_t = e_p + e_k = \mathbf{v}_s^{\mathsf{H}}\left(\frac{1}{2\rho_0 c_0^2}\mathbf{b}^*\mathbf{b}^{\mathsf{T}} + \frac{\rho_0}{4}\tilde{\mathbf{b}}^*\tilde{\mathbf{b}}^{\mathsf{T}}\right)\mathbf{v}_s = \mathbf{v}_s^{\mathsf{H}}\mathbf{A}_t\mathbf{v}_s \qquad (2.41)$$

with $\mathbf{A}_t$ denoting the coupling matrix with respect to the total sound energy density. As the matrix $\mathbf{A}_t$ is formulated as the sum of $\mathbf{A}_p$ and $\mathbf{A}_k$, the rank of $\mathbf{A}_t$ equals to four. In Eqs. (2.39)–(2.41), the sound energy densities are all expressed in a quadratic form. By this means, the resulting surface contributions will be non-negative by definition. As such, surface contributions based on sound energies avoid acoustic short circuits, which alternating signs can cause.

To assess the energy-based surface contributions, the matrix square root of the coupling matrix is required. For this purpose, we perform the eigendecomposition of the coupling matrix

$$\mathbf{A} = \Psi^{\mathsf{H}} \Lambda \Psi \tag{2.42}$$

with $\mathbf{A}$ representing the coupling matrix regarding the potential, the kinetic, and the total sound energy density. The eigenvectors and eigenvalues are stored in Ψ and $\Lambda = \text{diag}\{\lambda_i\}$, respectively. Note that the coupling matrices are Hermitian and complex-valued. As a consequence, the resulting eigenvalues are positive and real-valued. This allows to compute the eigenvalues according to $\sqrt{\Lambda} = \text{diag}\{\sqrt{\lambda_i}\}$. By this means, Eq. (2.42) can be rewritten as

$$\mathbf{A} = \Psi^{\mathsf{H}} \sqrt{\Lambda}^{\mathsf{H}} \sqrt{\Lambda} \Psi. \tag{2.43}$$

By introducing the normalization property of the eigenvectors, $\Psi \Psi^{\mathsf{H}} = \mathbf{I}$ with the identity matrix $\mathbf{I}$, Eq. (2.43) adapts to

$$\mathbf{A} = \Psi^{\mathsf{H}} \sqrt{\Lambda}^{\mathsf{H}} \mathbf{I} \sqrt{\Lambda} \Psi = \Psi^{\mathsf{H}} \sqrt{\Lambda}^{\mathsf{H}} \Psi \Psi^{\mathsf{H}} \sqrt{\Lambda} \Psi = \sqrt{\mathbf{A}}^{\mathsf{H}} \sqrt{\mathbf{A}}. \tag{2.44}$$

Finally, the expression for the matrix square root of the coupling matrix can be derived

$$\sqrt{\mathbf{A}} = \Psi^{\mathsf{H}} \sqrt{\Lambda} \Psi. \tag{2.45}$$

The surface contributions based on the sound energy density can now be defined. For instance, the potential energy density in Eq. (2.39) can be expressed by

$$e_p = \mathbf{v}_s^{\mathsf{H}} \mathbf{A}_p \mathbf{v}_s = \mathbf{v}_s^{\mathsf{H}} \sqrt{\mathbf{A}_p}^{\mathsf{H}} \sqrt{\mathbf{A}_p} \mathbf{v}_s = \sum_{j=1}^{N} \alpha_{p_j}^{\mathsf{H}} \alpha_{p_j} = \sum_{j=1}^{N} \mu_{p_j} \tag{2.46}$$

with μ_{p_j} denoting the surface contributions related to the potential energy density. In the equation above, the index j refers to the contributions of the node j to the potential energy density at the field point. Similarly, the kinetic and the total energy density-based surface contributions are derived

$$e_k = \mathbf{v}_s^{\mathsf{H}} \mathbf{A}_k \mathbf{v}_s = \mathbf{v}_s^{\mathsf{H}} \sqrt{\mathbf{A}_k}^{\mathsf{H}} \sqrt{\mathbf{A}_k} \mathbf{v}_s = \sum_{j=1}^{N} \alpha_{k_j}^{\mathsf{H}} \alpha_{k_j} = \sum_{j=1}^{N} \mu_{k_j}, \tag{2.47}$$

$$e_t = \mathbf{v}_s^{\mathsf{H}} \mathbf{A}_t \mathbf{v}_s = \mathbf{v}_s^{\mathsf{H}} \sqrt{\mathbf{A}_t}^{\mathsf{H}} \sqrt{\mathbf{A}_t} \mathbf{v}_s = \sum_{j=1}^{N} \alpha_{t_j}^{\mathsf{H}} \alpha_{t_j} = \sum_{j=1}^{N} \mu_{t_j} \tag{2.48}$$

with the surface contributions based on the kinetic energy density μ_{k_j} and the total sound energy density μ_{t_j}. As aforementioned, the energy-based surface contributions are unipolar and, thus, non-negative due to their quadratic form. Moreover, they contain only real-valued entries. Note that the present surface contributions μ are discrete entities, as they depend on the resolution of the boundary element mesh. For instance, refining a bound-

ary element mesh with N nodes by a factor of two would halve the values of the surface contributions, i.e., $\mu_j = e/N$. For this purpose, we introduce a continuous version of the surface contributions, which is evaluated by

$$\mu = \sqrt{\Theta}\eta \tag{2.49}$$

with the boundary mass matrix

$$\Theta_{kl} = \int_\Gamma \varphi_k \varphi_l \mathrm{d}\Gamma. \tag{2.50}$$

The continuous surface contributions η are independent of the mesh resolution and are, thus, used to visualize the results [130].

The sound energy is used as a control objective to identify contributing surfaces regarding an entire volume. For this purpose, the volume integral is approximated by the finite sum of the energy density at a field point grid. The field points within this grid are regularly distributed in the domain. The sound energy density at these points can then be understood as integration points. The sum of the related energy densities yields an approximation for the sound energy within the domain

$$\int_\Omega e \, \mathrm{d}\Omega \approx \sum_{i=1}^{N_p} e_i \cdot V_i = V_c \sum_{i=1}^{N_p} e_i \tag{2.51}$$

with the volume cell V_i related to the field point i. The volume of the cells are all constant, i.e., $V_i = V_c$, when the field points are regularly distributed within the cavity. By approximating the total volume of the cavity, i.e., $V \approx N_p \cdot V_c$, the sound energy can be obtained by using its averaged version

$$E \approx V_c \sum_{i=1}^{N_p} e_i. \tag{2.52}$$

In close analogy to Eqs. (2.39)–(2.41), the volume-related sound energy can be expressed in a quadratic form. For the potential sound energy, Eq. (2.33) is rewritten as

$$E_p = \frac{1}{2\rho_0 c_0^2} \sum_{i=1}^{N_p} (\mathbf{b}_i^\mathsf{T} \mathbf{v}_s)^* (\mathbf{b}_i^\mathsf{T} \mathbf{v}_s) = \frac{1}{2\rho_0 c_0^2} \mathbf{v}_s^\mathsf{H} \left(\sum_{i=1}^{N_p} \mathbf{b}_i^* \mathbf{b}_i^\mathsf{T} \right) \mathbf{v}_s = \mathbf{v}_s^\mathsf{H} \left(\sum_{i=1}^{N_p} \mathbf{A}_{p_i} \right) \mathbf{v}_s = \mathbf{v}_s^\mathsf{H} \mathbf{A}_p \mathbf{v}_s. \tag{2.53}$$

In the equation above, $\mathbf{A}_p$ represents the coupling matrix regarding the potential energy, which is approximated by the potential energy density at multiple field points. Thus, the rank of the potential energy-related coupling matrix adapts to N_p. Regarding the kinetic sound energy, the quadratic formulation reads

$$E_k = \frac{\rho_0}{4} \sum_{i=1}^{N_p} (\tilde{\mathbf{b}}_i^\mathsf{T} \mathbf{v}_s)^* (\tilde{\mathbf{b}}_i^\mathsf{T} \mathbf{v}_s) = \frac{\rho_0}{4} \mathbf{v}_s^\mathsf{H} \left(\sum_{i=1}^{N_p} \tilde{\mathbf{b}}_i^* \tilde{\mathbf{b}}_i^\mathsf{T} \right) \mathbf{v}_s = \mathbf{v}_s^\mathsf{H} \left(\sum_{i=1}^{N_p} \mathbf{A}_{k_i} \right) \mathbf{v}_s = \mathbf{v}_s^\mathsf{H} \mathbf{A}_k \mathbf{v}_s, \tag{2.54}$$

where $\mathbf{A}_k$ denotes the coupling matrix regarding the kinetic energy. The rank of this matrix adapts to $3N_p$, as the kinetic energy density is defined in three spatial directions. Since the total sound energy is defined as the sum of the potential and the kinetic energy, the quadratic form of the total sound energy can be expressed by

$$E_t = E_p + E_k = \frac{1}{2\rho_0 c^2} \sum_{i=1}^{N_p} (\mathbf{b}_i^{\mathsf{T}} \mathbf{v}_s)^* (\mathbf{b}_i^{\mathsf{T}} \mathbf{v}_s) + \frac{\rho_0}{4} \sum_{i=1}^{N} (\tilde{\mathbf{b}}_i^{\mathsf{T}} \mathbf{v}_s)^* (\tilde{\mathbf{b}}_i^{\mathsf{T}} \mathbf{v}_s) = \mathbf{v}_s^{\mathsf{H}} \mathbf{A}_p \mathbf{v}_s + \mathbf{v}_s^{\mathsf{H}} \mathbf{A}_k \mathbf{v}_s = \mathbf{v}_s^{\mathsf{H}} \mathbf{A}_t \mathbf{v}_s$$

(2.55)

with the coupling matrix $\mathbf{A}_t = \mathbf{A}_p + \mathbf{A}_k$ related to the total sound energy in the volume. As such, the rank of $\mathbf{A}_t$ is $4N_p$ [139].

Finally, by using the expression for the matrix square root in Eq.(2.45), the volume-related surface contributions based on the sound energy can be similarly derived as

$$E_p = \mathbf{v}_s^{\mathsf{H}} \mathbf{A}_p \mathbf{v}_s = \mathbf{v}_s^{\mathsf{H}} \sqrt{\mathbf{A}_p}^{\mathsf{H}} \sqrt{\mathbf{A}_p} \mathbf{v}_s = \sum_{j=1}^{N_n} \alpha_{p_j}^* \alpha_{p_j} = \sum_{j=1}^{N_n} \mu_{p_j},$$

(2.56)

$$E_k = \mathbf{v}_s^{\mathsf{H}} \mathbf{A}_k \mathbf{v}_s = \mathbf{v}_s^{\mathsf{H}} \sqrt{\mathbf{A}_k}^{\mathsf{H}} \sqrt{\mathbf{A}_k} \mathbf{v}_s = \sum_{j=1}^{N_n} \alpha_{k_j}^* \alpha_{k_j} = \sum_{j=1}^{N_n} \mu_{k_j},$$

(2.57)

$$E_t = \mathbf{v}_s^{\mathsf{H}} \mathbf{A}_t \mathbf{v}_s = \mathbf{v}_s^{\mathsf{H}} \sqrt{\mathbf{A}_t}^{\mathsf{H}} \sqrt{\mathbf{A}_t} \mathbf{v}_s = \sum_{j=1}^{N_n} \alpha_{t_j}^* \alpha_{t_j} = \sum_{j=1}^{N_n} \mu_{t_j},$$

(2.58)

where N_n denotes the number of boundary element nodes. The surface contributions related to the potential, the kinetic, and the total sound energy in the volume are denoted by μ_p, μ_k, and μ_t, respectively. Once again, it should be highlighted that all energy-based surface contributions are non-negative. Consequently, acoustic short circuits caused by bipolar surface contributions are inherently avoided [139].

The entire algorithm for the energy-based contribution analysis is summarized in Algorithm 1. It is not mandatory to explicitly evaluate the acoustic quantities at the field points, e.g., the sound pressure, the particle velocity, or the sound energy density. Since we are interested in the contributions of the enveloping surfaces, our investigations focus on quantities associated with them. These are, in particular, the influence coefficients and the coupling matrices related to the sound energy densities. It should be further noted that the matrix inverse of $(\mathbf{H} - \mathbf{G}\mathbf{Y})^{-1}$ is not explicitly computed. The inverse operation is circumvented by solving the related linear system of equations. For the sake of clarity, the pseudo-algorithm is limited to the presentation of the surface contributions with respect to a single field point. However, by substituting the expressions related to a single evaluation point with their multi-point counterpart, the algorithm can be readily adapted for contribution analyses regarding multiple field points.

Algorithm 1 Surface contribution analysis based on the sound energy density

---

1: **input**
2:     boundary element mesh
3:     boundary conditions $\mathbf{v}_s(\vec{x})$ and $\mathbf{Y}(\vec{x})$
4:     Position of the field point $\vec{y}$
5: **Acoustic quantities on the boundary**
6:     Assemble the single layer potential matrix $\mathbf{G}$ ▷ Eq.(2.17)
7:     ... the double layer potential matrix $\mathbf{H}$ ▷ Eq.(2.18)
8:     ... and the boundary mass matrix Θ ▷ Eq.(2.50)
9: **Acoustic quantities at the field points**
10:     Assemble the boundary integral operator $\mathbf{g}$ ▷ Eq.(2.22)
11:     ... and the boundary integral operator $\mathbf{h}$ ▷ Eq.(2.23)
12:     Evaluate the influence coefficients regarding the sound pressure $\mathbf{b}$ ▷ Eq.(2.24)
13:     Compute the influence coefficients w.r.t the particle velocity $\tilde{\mathbf{b}}$ ▷ Eq.(2.32)
14: **Surface contributions based on sound energy densities**
15:     Assemble the coupling matrix related to the potential energy density $\mathbf{A}_p$ ▷
    Eq.(2.39)
16:     ... the kinetic energy density $\mathbf{A}_k$ ▷ Eq.(2.40)
17:     ... and the total sound energy density $\mathbf{A}_t$ ▷ Eq.(2.41)
18:     Perform the eigendecomposition of $\mathbf{A}_p$, $\mathbf{A}_k$, and $\mathbf{A}_t$ ▷ Eq.(2.42)
19:     Evaluate the discrete surface contributions for the potential energy density μ_p ▷
    Eq.(2.46)
20:     ... the kinetic energy density μ_k ▷ Eq.(2.47)
21:     ... and the total sound energy density μ_t ▷ Eq.(2.48)
22:     Compute the continuous surface contributions η_p, η_k, and η_t ▷ Eq.(2.49)
23: **return**
24:     Surface contributions based on the potential energy density η_p
25:     Surface contributions based on the kinetic energy density η_k
26:     Surface contributions based on the total sound energy density η_t

---

2.6 Gaussian process regression

A finite set of data points x_1, x_2, ..., x_n with a Gaussian distributed marginal density $P\left(y(x_1), y(x_2), ..., y_{(x_n)}\right)$ defines a Gaussian process (GP). By this means, a GP can be understood as the probability distribution of an arbitrary function $y(x)$ [90]. GPs consider aleatoric and epistemic uncertainties. Aleatoric uncertainties are attributed to the random outcome of a data generation process, e.g., the coin flip. As such, they are unaffected by additional knowledge of the system or repetitions of the experiment. Thus, the aleatoric uncertainty is commonly referred to as stochastic uncertainty. On the other hand, epistemic uncertainties refer to limited information on the underlying problem. They may arise when specific effects are neglected in a model or when only limited knowledge of model parameters exists. New information about the system mitigates epistemic uncertainties. They are thus classified as systematic uncertainties. In GPs, aleatoric and epistemic uncertainties can occur at the same time. For instance, the epistemic uncertainty due to limited parameter information may interact with the stochastic outcome of an experiment [135].

In the course of this thesis, GPs are used as surrogates to approximate the system response in the frequency dimension. The related input variables are denoted by $\mathbf{f} = [f_1, f_2, ..., f_n]$ representing a finite set of discrete frequencies. To avoid a clash of notation, the function to be estimated is declared by $h(\mathbf{f})$ with the discrete frequency points as arguments. In this way, $h(\mathbf{f})$ represents the frequency response function of the acoustic system. The related GP

$$h(\mathbf{f}) \sim \mathscr{GP}\left(m(\mathbf{f}), \mathrm{cov}(\mathbf{f}, \mathbf{f}')\right). \tag{2.59}$$

is then specified by a mean function $m(\mathbf{f})$ and a covariance function $\mathrm{cov}(\mathbf{f}, \mathbf{f}')$. The quantities $\mathbf{f}$ and $\mathbf{f}'$ are associated with two frequency input sets. Instead of computing the inner product of the input frequencies, the interaction between frequency points can be expressed by the evaluation of the covariance function, or kernel, $\mathrm{cov}(\mathbf{f}, \mathbf{f}')$. By doing so, the interactions are transferred from the input space to the feature space enabling efficient and practical analyses of the underlying features. In the literature, this procedure is also known as the kernel trick. In this light, the choice of the kernel or covariance function becomes of great importance [91, 140].

In the scope of this work, the squared exponential kernel is adopted for the covariance function

$$\mathrm{cov}(\mathbf{f}, \mathbf{f}') = \sigma_f^2 \exp\left(-\frac{1}{2l^2}(\mathbf{f} - \mathbf{f}')^\mathsf{T}(\mathbf{f} - \mathbf{f}')\right) \tag{2.60}$$

with the characteristic length l and the signal variance σ_f^2 denoting the kernel parameters. Closer inspection on Eq.(2.60) reveals that the covariance function solely depends on the discrete input frequencies. Thus, the related covariance of the output system responses is determined by the input frequencies' covariance. For the squared exponential kernel, it becomes apparent that the covariance increases when the input frequencies approach each other. In contrast to this, larger spacing between the input frequencies results in a

small covariance [91].

By evaluating the covariance function for a set of input frequencies $\mathbf{f}$ and $\mathbf{f'}$, a prior probability distribution can be obtained for the unknown function. The mean function is set to zero in this first step, and no observed data is considered. This defines the GP prior, which is expressed by

$$\mathbf{h} \sim \mathscr{N}\left(\mathbf{0}, \text{cov}(\mathbf{f}, \mathbf{f'})\right) \tag{2.61}$$

with the entity $\mathscr{N}$ representing a multivariate Gaussian distribution. In the course of this thesis, only real-valued quantities such as the sound pressure level or energy density level are investigated. For this purpose, the real-valued multivariate Gaussian distribution is adopted. A schematic representation of the GP prior is depicted in Fig. 2(a). It becomes apparent that without any data, the mean of the GP is zero at each frequency. In addition to this, the uncertainty referring to a 95 % confidence interval remains constant [91].

In that form, GP priors are relatively unspectacular and without practical importance. GPs become particularly useful when information on the underlying problem is incorporated. That information is manifested in observations of the physical process. In the scope of this thesis, the frequency response $\mathbf{h}$ of an acoustic system accounts for the observed data. The frequencies we are interested in the system response are sub-scripted with the asterisk symbol, i.e., $\mathbf{f}_*$. The entity $\mathbf{h}_*$ represents the related unknown frequency responses. The joint probability distribution of the observed and the unknown frequency responses, $\mathbf{h}$ and $\mathbf{h}_*$, can be then formulated as

$$\begin{bmatrix} \mathbf{h} \\ \mathbf{h}_* \end{bmatrix} \sim \mathscr{N}\left(\mathbf{0}, \begin{bmatrix} \mathbf{K}(\mathbf{f}, \mathbf{f}) & \mathbf{K}(\mathbf{f}, \mathbf{f}_*) \\ \mathbf{K}(\mathbf{f}_*, \mathbf{f}) & \mathbf{K}(\mathbf{f}_*, \mathbf{f}_*) \end{bmatrix}\right). \tag{2.62}$$

Evaluating the covariance function for a pair of frequency inputs yields the covariance matrix $\mathbf{K}$. For n frequencies with available observations, the covariance matrix $\mathbf{K}(\mathbf{f}, \mathbf{f})$ is of size $n \times n$. For n_* frequencies, where the corresponding system response is unknown, the covariance matrices $\mathbf{K}(\mathbf{f}, \mathbf{f}_*)$ and $\mathbf{K}(\mathbf{f}_*, \mathbf{f}_*)$ are of size $n \times n_*$ and $n_* \times n_*$, respectively. Note that $\mathbf{K}(\mathbf{f}_*, \mathbf{f})$ is the transpose of the matrix $\mathbf{K}(\mathbf{f}, \mathbf{f}_*)$, i.e. $\mathbf{K}(\mathbf{f}, \mathbf{f}_*)^\mathsf{T} = \mathbf{K}(\mathbf{f}_*, \mathbf{f})$ [91].

By computing the Schur complement of the block matrix $\mathbf{K}(\mathbf{f}, \mathbf{f})$, the conditional probability distribution for $\mathbf{h}_*$ given $\mathbf{f}_*$, $\mathbf{f}$, and $\mathbf{h}$ is introduced by [91, 136]

$$P(\mathbf{h}_*|\mathbf{f}_*, \mathbf{f}, \mathbf{h}) \sim \mathscr{N}(\mathbf{K}(\mathbf{f}_*, \mathbf{f})\mathbf{K}(\mathbf{f}, \mathbf{f})^{-1}\mathbf{h}, \mathbf{K}(\mathbf{f}_*, \mathbf{f}_*) - \mathbf{K}(\mathbf{f}_*, \mathbf{f})\mathbf{K}(\mathbf{f}, \mathbf{f})^{-1}\mathbf{K}(\mathbf{f}, \mathbf{f}_*)) \tag{2.63}$$

with the posterior mean $\bar{\mathbf{h}}_* = \mathbf{K}(\mathbf{f}_*, \mathbf{f})\mathbf{K}(\mathbf{f}, \mathbf{f})^{-1}\mathbf{h}$ and the posterior covariance $\text{cov}(\mathbf{h}_*) = \mathbf{K}(\mathbf{f}_*, \mathbf{f}_*) - \mathbf{K}(\mathbf{f}_*, \mathbf{f})\mathbf{K}(\mathbf{f}, \mathbf{f})^{-1}\mathbf{K}(\mathbf{f}, \mathbf{f}_*)$. With these two entities, the GP posterior is fully specified. Fig. 2(b) visualizes the GP posterior for given observations on the sound pressure level. In this figure, it becomes clear that the posterior mean satisfies the observed SPL values. Moreover, the posterior covariance, which corresponds to a 95 % confidence interval, is small near the observations. For larger distances between the observations, the posterior covariance increases. Note that the smooth profile of the posterior GP is essentially determined by the characteristic length l of the kernel [91].
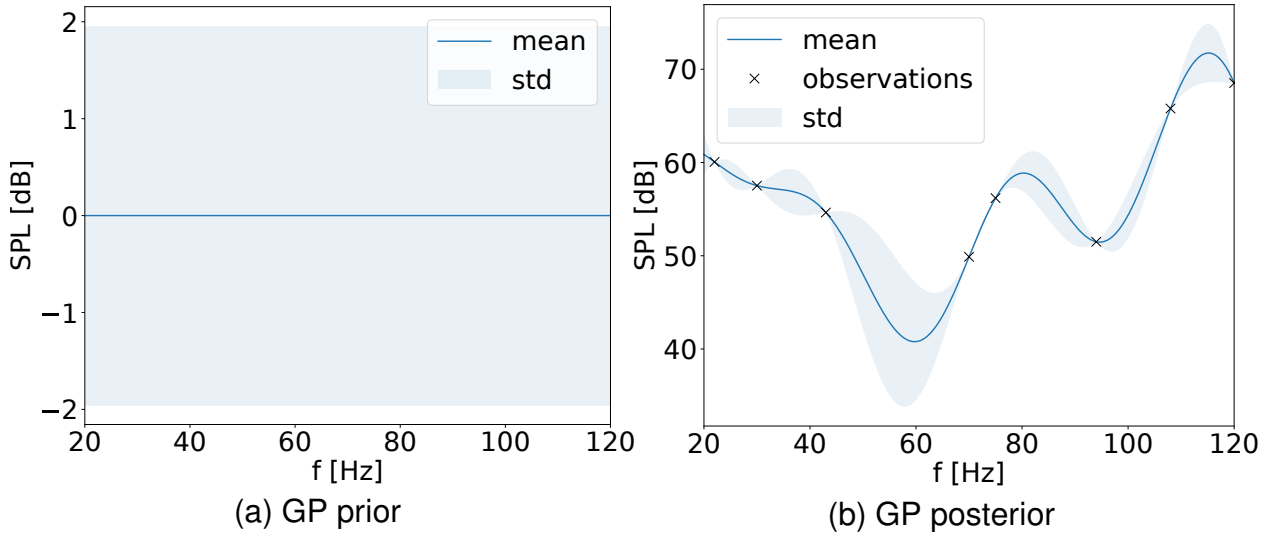
(a) GP prior   (b) GP posterior

Figure 2: GP prior without any observations yields a zero mean (blue) (a). GP posterior with eight observations on the SPL (black crosses) results in a mean (blue), which fulfills the observed data. The posterior covariance (blue-shaded area) is small around the observations and large when the distance between the observed data increases (b). In both figures, the uncertainty corresponds to a 95 % confidence interval (blue-shaded area).

Up to this point, the observed data referred directly to the values of the frequency response function. Although this assumption is reasonable for numerical simulations, in practical applications, observations may contain a considerable amount of additional meaningless information called noise. The observations of noisy data can then be formulated as

$$\mathbf{y} = \mathbf{h}(\mathbf{f}) + \varepsilon \tag{2.64}$$

for additive independent identically distributed Gaussian noise, i.e. $\varepsilon \sim \mathcal{N}(\mathbf{0}, \sigma_n^2 \mathbf{I})$, with σ_n^2 representing the level of noise [137].

The covariance function from Eq.(2.60) can be reformulated for noisy observations

$$\operatorname{cov}(\mathbf{f}, \mathbf{f}') = \mathbf{K}(\mathbf{f}, \mathbf{f}) + \sigma_n^2 \mathbf{I} = \sigma_f^2 \exp\left(-\frac{1}{2l^2}(\mathbf{f} - \mathbf{f}')^{\mathsf{T}}(\mathbf{f} - \mathbf{f}')\right) + \sigma_n^2 \mathbf{I}. \tag{2.65}$$

The noise-related matrix $\sigma_n^2 \mathbf{I}$ contains only entries on the diagonal due to the assumption of independent identically distributed noise. The joint probability distribution of noisy data $\mathbf{y}$ and unknown response function values $\mathbf{h}_*$ then reads

$$\begin{bmatrix} \mathbf{y} \\ \mathbf{h}_* \end{bmatrix} \sim \mathcal{N}\left(\mathbf{0}, \begin{bmatrix} \mathbf{K}(\mathbf{f}, \mathbf{f}) + \sigma_n^2 \mathbf{I} & \mathbf{K}(\mathbf{f}, \mathbf{f}_*) \\ \mathbf{K}(\mathbf{f}_*, \mathbf{f}) & \mathbf{K}(\mathbf{f}_*, \mathbf{f}_*) \end{bmatrix}\right). \tag{2.66}$$

In close analogy to Eq.(2.63), conditioning on the observations yields the posterior GP for noisy observations

$$P(\mathbf{h}_*|\mathbf{f}_*, \mathbf{f}, \mathbf{y}) \sim \mathscr{N}\left(\bar{\mathbf{h}}_*, \text{cov}(\mathbf{h}_*)\right), \tag{2.67}$$

with the posterior mean $\bar{\mathbf{h}}_*$ and the posterior covariance $\text{cov}(\mathbf{h}_*)$

$$\bar{\mathbf{h}}_* = \mathbf{K}(\mathbf{f}_*, \mathbf{f})\left[\mathbf{K}(\mathbf{f}, \mathbf{f}) + \sigma_n^2 \mathbf{I}\right]^{-1}\mathbf{y}, \tag{2.68}$$

$$\text{cov}(\mathbf{h}_*) = \mathbf{K}(\mathbf{f}_*, \mathbf{f}_*) - \mathbf{K}(\mathbf{f}_*, \mathbf{f})\left[\mathbf{K}(\mathbf{f}, \mathbf{f}) + \sigma_n^2 \mathbf{I}\right]^{-1}\mathbf{K}(\mathbf{f}, \mathbf{f}_*)^{\mathsf{T}}. \tag{2.69}$$

Eqs. (2.67)-(2.69) fully specify the posterior GP. At this stage, the GP can be applied for frequency response predictions in presence of noise [91].

An optimization problem is solved to find the parameters of the covariance function. The optimal values for the kernel parameters are obtained by minimizing the negative marginal log likelihood

$$\log P(\mathbf{y}|\mathbf{f}) = -\frac{1}{2}\mathbf{y}^{\mathsf{T}}(\mathbf{K}(\mathbf{f}, \mathbf{f}) + \sigma_n^2 \mathbf{I})^{-1}\mathbf{y} - \frac{1}{2}\log|\mathbf{K}(\mathbf{f}, \mathbf{f}) + \sigma_n^2 \mathbf{I}| - \frac{n}{2}\log 2\pi, \tag{2.70}$$

which is adopted as the objective function. The first term in Eq.(2.70) corresponds to the fit of the data, whereas the second term evaluates the complexity of the model. The third term is understood as a normalizing constant. Thus, the solution of the minimization problem results in parameters, which achieve the optimal trade-off between the quality of the fit and the model complexity. To apply a gradient-based optimization method, the derivatives of the negative log likelihood with respect to the kernel parameters θ_j are required. The related derivatives are expressed by

$$\frac{\partial \log P(\mathbf{y}|\mathbf{f})}{\partial \theta_j} = -\frac{1}{2}\mathbf{y}^{\mathsf{T}}\mathbf{K}_y^{-1}\frac{\partial \mathbf{K}_y}{\partial \theta_j}\mathbf{K}_y^{-1}\mathbf{y} - \frac{1}{2}\text{tr}\left(\mathbf{K}_y^{-1}\frac{\partial \mathbf{K}_y}{\partial \theta_j}\right) = \frac{1}{2}\text{tr}\left(\left(\alpha\alpha^T - \mathbf{K}_y^{-1}\right)\frac{\partial \mathbf{K}_y}{\partial \theta_j}\right) \quad (2.71)$$

with $\mathbf{K}_y = \mathbf{K}(\mathbf{f}, \mathbf{f}) + \sigma_n^2 \mathbf{I}$ and $\alpha = \mathbf{K}_y^{-1}\mathbf{y}$. A note of caution is due here, since the objective function is non-convex. Therefore, it is important to bear in mind that multiple minima can occur [138].

The formulation of a GP is schematically described in a pseudo-algorithm, see Algorithm 2. Note that the covariance sub-matrix $\mathbf{K}(\mathbf{f}, \mathbf{f}) + \sigma_n^2 \mathbf{I}$ is symmetric and positive definite. For this reason, the matrix inverse operation can be replaced by using the Cholesky decomposition of that matrix. For the sake of conciseness, the pseudo-algorithm is only shown for noisy observations.

Algorithm 2 Gaussian Processes for frequency response function analyses

---
1: **input**
2:     Frequencies with known response functions $\mathbf{f}$
3:     Corresponding known frequency response functions $\mathbf{h}$
4:     Covariance function $\mathrm{cov}(\mathbf{f}, \mathbf{f}')$
5:     Noise level σ_n^2
6:     Relevant frequencies with unknown response functions $\mathbf{f}_*$
7: **Assembly of the covariance matrix**
8:     Assemble $\mathbf{K}(\mathbf{f}, \mathbf{f})$, $\mathbf{K}(\mathbf{f}, \mathbf{f}_*)$, and $\mathbf{K}(\mathbf{f}_*, \mathbf{f}_*)$ ▷ Eq.(2.66)
9:     Cholesky decomposition $\mathbf{L} := \mathrm{chol}[\mathbf{K}(\mathbf{f}, \mathbf{f}) + \sigma_n^2 \mathbf{I}]$
10:     Substitute the matrix inverse $\mathbf{L}^{-\mathsf{T}} \mathbf{L}^{-1} = [\mathbf{K}(\mathbf{f}, \mathbf{f}) + \sigma_n^2 \mathbf{I}]^{-1}$
11: **Find the optimal kernel parameters**
12:     Evaluate the negative marginal log likelihood $\log P(\mathbf{y}|\mathbf{f})$ ▷ Eq.(2.70)
13:     Compute the gradient of the likelihood $\partial \log P(\mathbf{y}|\mathbf{f})/\partial \theta_j$ ▷ Eq.(2.71)
14: **Posterior GP mean and covariance**
15:     Evaluate the posterior GP mean $\bar{\mathbf{h}}_*$ ▷ Eq.(2.68)
16:     Compute the posterior GP covariance $\mathrm{cov}(\mathbf{h}_*)$ ▷ Eq.(2.69)
17: **return**
18:     Posterior GP mean $\bar{\mathbf{h}}_*$
19:     Posterior GP covariance $\mathrm{cov}(\mathbf{h}_*)$

2.7 Multi-fidelity modeling using Gaussian processes

In the following, we consider the most accurate model with the highest computational costs as the high-fidelity (HF) model $\mathbf{h}_H(\mathbf{f})$. A representation of that model on a lower fidelity level is assumed as the low-fidelity (LF) model $\mathbf{h}_L(\mathbf{f})$. In contrast to the HF model, the LF model is fast to evaluate but relatively inaccurate. For two distinct input frequencies, i.e., $\mathbf{f} \neq \mathbf{f}'$, it can be assumed that no further information can be gained on $\mathbf{h}_H(\mathbf{f})$ by evaluating $\mathbf{h}_L(\mathbf{f}')$ given the solution $\mathbf{h}_L(\mathbf{f})$. This relation is manifested in a Markov-type property, which can be expressed by [108]

$$\mathrm{cov}\left(\mathbf{h}_H(\mathbf{f}), \mathbf{h}_L(\mathbf{f}') \mid \mathbf{h}_L(\mathbf{f})\right) = 0. \tag{2.72}$$

This property is inherent to autoregressive models, which predict the model response based on previous observations. For two fidelity levels, an autoregressive model can be formulated as [110]

$$\mathbf{h}_H(\mathbf{f}) = \eta\,\mathbf{h}_L(\mathbf{f}) + \delta(\mathbf{f}), \tag{2.73}$$

where the approximation of the HF solution is realized as a surrogate model. This surrogate depends linearly on two distinct GPs

$$\mathbf{h}_L \sim \mathscr{GP}\left(0, \mathrm{cov}_L\left(\mathbf{f}, \mathbf{f}'\right)\right), \tag{2.74}$$

$$\delta \sim \mathscr{GP}\left(0, \mathrm{cov}_H\left(\mathbf{f}, \mathbf{f}'\right)\right). \tag{2.75}$$

with $\text{cov}_L(\mathbf{f}, \mathbf{f}')$ and $\text{cov}_H(\mathbf{f}, \mathbf{f}')$ denoting the covariance function associated with the LF and the HF model, respectively. The relation between the HF and the model is established by the coupling parameter η. By inspecting Eq.(2.73), it becomes apparent that the two fidelity levels are decoupled when $\eta = 0$. In that case, one cannot expect any improvement of the approximation, if additional LF data would have been included [115].

According to [108, 109], the multivariate GP for the multiple fidelity levels $\mathbf{h}_L$ and $\mathbf{h}_H$ can be equivalently expressed by

$$\begin{bmatrix} \mathbf{h}_L \\ \mathbf{h}_H \end{bmatrix} \sim \mathscr{GP} \left(\begin{bmatrix} \mathbf{0} \\ \mathbf{0} \end{bmatrix}, \begin{bmatrix} \text{cov}_L(\mathbf{f}_L, \mathbf{f}_L) & \eta\,\text{cov}_L(\mathbf{f}_L, \mathbf{f}_H) \\ \eta\,\text{cov}_L(\mathbf{f}_L, \mathbf{f}_H) & \eta^2\,\text{cov}_L(\mathbf{f}_L, \mathbf{f}_H) + \text{cov}_H(\mathbf{f}_L, \mathbf{f}_H) \end{bmatrix} \right). \tag{2.76}$$

By substituting $\text{cov}_{LL} = \text{cov}_L$, $\text{cov}_{LH} = \text{cov}_{HL} = \eta\,\text{cov}_L$, and $\text{cov}_{HH} = \eta^2\,\text{cov}_L + \text{cov}_H$, Eq.(2.76) can be rewritten in a simplified form

$$\begin{bmatrix} \mathbf{h}_L \\ \mathbf{h}_H \end{bmatrix} \sim \mathscr{GP} \left(\begin{bmatrix} \mathbf{0} \\ \mathbf{0} \end{bmatrix}, \begin{bmatrix} \text{cov}_{LL}(\mathbf{f}_L, \mathbf{f}_L) & \text{cov}_{LH}(\mathbf{f}_L, \mathbf{f}_H) \\ \text{cov}_{HL}(\mathbf{f}_L, \mathbf{f}_H) & \text{cov}_{HH}(\mathbf{f}_L, \mathbf{f}_H) \end{bmatrix} \right). \tag{2.77}$$

Introducing the unknown system response $\mathbf{h}_*$ at the relevant frequencies $\mathbf{f}_*$ yields the joint probability density [115]

$$\begin{bmatrix} \mathbf{h}_* \\ \mathbf{h}_L \\ \mathbf{h}_H \end{bmatrix} \sim \mathscr{GP} \left(\begin{bmatrix} \mathbf{0} \\ \mathbf{0} \\ \mathbf{0} \end{bmatrix}, \begin{bmatrix} \text{cov}_{**}(\mathbf{f}_*, \mathbf{f}_*) & \text{cov}_{*L}(\mathbf{f}_*, \mathbf{f}_L) & \text{cov}_{*H}(\mathbf{f}_*, \mathbf{f}_H) \\ \text{cov}_{L*}(\mathbf{f}_L, \mathbf{f}_*) & \text{cov}_{LL}(\mathbf{f}_L, \mathbf{f}_L) & \text{cov}_{LH}(\mathbf{f}_L, \mathbf{f}_H) \\ \text{cov}_{H*}(\mathbf{f}_H, \mathbf{f}_*) & \text{cov}_{HL}(\mathbf{f}_L, \mathbf{f}_H) & \text{cov}_{HH}(\mathbf{f}_H, \mathbf{f}_H) \end{bmatrix} \right). \tag{2.78}$$

In close analogy to Eq.(2.63), the conditional probability distribution of the unknown response functions $\mathbf{h}_*$ given the frequencies of interest $\mathbf{f}_*$ and the solutions of the LF and the HF model is expressed by

$$P(\mathbf{h}_* | \mathbf{f}_*, \mathbf{f}_L, \mathbf{h}_L, \mathbf{f}_H, \mathbf{h}_H) = \mathcal{N}(\mathbf{K}_* \mathbf{K}^{-1} \mathbf{h}, \mathbf{K}_{**} - \mathbf{K}_* \mathbf{K}^{-1} \mathbf{K}_*^\mathsf{T}), \tag{2.79}$$

where the posterior mean $\bar{\mathbf{h}}_*$ and the posterior covariance $\text{cov}(\mathbf{h}_*)$ of the multi-fidelity GP are obtained by

$$\bar{\mathbf{h}}_* = \mathbf{K}_* \mathbf{K}^{-1} \mathbf{h}, \tag{2.80}$$

$$\text{cov}(\mathbf{h}_*) = \mathbf{K}_{**} - \mathbf{K}_* \mathbf{K}^{-1} \mathbf{K}_*^\mathsf{T}. \tag{2.81}$$

For the sake of conciseness, the dependencies on the input frequency sets are omitted in the presentation of the mean and the sub-matrices of the covariance. Note that the

compact notation in the equations above results from the following expressions:

$$\mathbf{h} = \begin{bmatrix} \mathbf{h}_L & \mathbf{h}_H \end{bmatrix}^\mathsf{T}, \tag{2.82}$$

$$\mathbf{K}_* = \begin{bmatrix} \mathrm{cov}_{*L}(\mathbf{f}_*, \mathbf{f}_L) & \mathrm{cov}_{*H}(\mathbf{f}_*, \mathbf{f}_H) \end{bmatrix}, \tag{2.83}$$

$$\mathbf{K} = \begin{bmatrix} \mathrm{cov}_{LL}(\mathbf{f}_L, \mathbf{f}_L) & \mathrm{cov}_{LH}(\mathbf{f}_L, \mathbf{f}_H) \\ \mathrm{cov}_{HL}(\mathbf{f}_H, \mathbf{f}_L) & \mathrm{cov}_{HH}(\mathbf{f}_H, \mathbf{f}_H) \end{bmatrix}, \tag{2.84}$$

$$\mathbf{K}_{**} = \begin{bmatrix} \mathrm{cov}_{**}(\mathbf{f}_*, \mathbf{f}_*) \end{bmatrix}. \tag{2.85}$$

In Eqs. (2.79)–(2.81), the multi-fidelity model using GPs is fully specified. However, in these equations, the presence of noise is neglected. For noisy observed data, the conditional probability density adapts to

$$P(\mathbf{h}_*|\mathbf{f}_*, \mathbf{f}_L, \mathbf{y}_L, \mathbf{f}_H, \mathbf{y}_H) = \mathcal{N}(\mathbf{K}_* \mathbf{K}^{-1} \mathbf{y}, \mathbf{K}_{**} - \mathbf{K}_* \mathbf{K}^{-1} \mathbf{K}_*^\mathsf{T}) \tag{2.86}$$

with $\mathbf{y} = [\mathbf{y}_L \ \mathbf{y}_H]^\mathsf{T}$ as the noisy version of the unknown response function values $\mathbf{h} = [\mathbf{h}_L \ \mathbf{h}_H]^\mathsf{T}$. The sub-matrices $\mathbf{K}_*$ and $\mathbf{K}_{**}$ remain the same as in Eq.(2.83) and Eq.(2.85), respectively. As opposed to that, the sub-matrix $\mathbf{K}$ is substituted by its noisy version $\mathbf{K}_y$, which is expressed by

$$\mathbf{K}_y = \begin{bmatrix} \mathrm{cov}_{LL}(\mathbf{f}_L, \mathbf{f}_L) + \sigma_{nL}^2 \mathbf{I} & \mathrm{cov}_{LH}(\mathbf{f}_L, \mathbf{f}_H) \\ \mathrm{cov}_{HL}(\mathbf{f}_H, \mathbf{f}_L) & \mathrm{cov}_{HH}(\mathbf{f}_H, \mathbf{f}_H) + \sigma_{nH}^2 \mathbf{I} \end{bmatrix}, \tag{2.87}$$

where σ_{nL}^2 and σ_{nH}^2 denote the noise level of the LF and the HF data, respectively. Due to the independence assumption, only the diagonal entries of the covariance matrix are affected by the noise levels. To obtain the noise level, the signal-to-noise ratio (SNR) is introduced as

$$\mathrm{SNR} = 10 \cdot \log\left(\frac{\mathbf{y}\mathbf{y}^\mathsf{T}}{\sigma_n^2}\right) \tag{2.88}$$

with $\sigma_n^2 = \begin{bmatrix} \sigma_{nL}^2 & \sigma_{nH}^2 \end{bmatrix}$ representing the noise level of the LF and the HF data. The noise level can then be estimated by prescribing a reasonable value for the SNR.

In the final step, the values of the parameters in the multi-fidelity GP are computed. They are obtained in a similar way to Eq.(2.70), where an optimization problem is solved by minimizing the negative log likelihood function. Regarding the multi-fidelity GP, the negative log likelihood for noisy observations adapts to

$$\log P(\mathbf{y}|\mathbf{f}) = -\frac{1}{2}\mathbf{y}^\mathsf{T}\left[\mathbf{K}_y + \sigma_n^2\mathbf{I}\right]^{-1}\mathbf{y} - \frac{1}{2}\log|\mathbf{K}_y + \sigma_n^2\mathbf{I}| - \frac{n_L + n_H}{2}\log 2\pi \tag{2.89}$$

with n_L and n_H denoting the number of LF and HF data points, respectively. Analogously, the derivative of the likelihood function with respect to the parameters can be computed by Eq.(2.71). The set of parameters in the multi-fidelity GP then adapts to $\theta_j = \left[l_L, \sigma_{fL}, l_H, \sigma_{fH}, \eta\right]$ with $\left[l_L, \sigma_{fL}\right]$ and $\left[l_H, \sigma_{fH}\right]$ related to the covariance function of the LF and the HF model, respectively. Moreover, the coupling parameter η is introduced to the optimization problem.

The implementation of the multi-fidelity GP is depicted in Algorithm 3. The pseudo-algorithm of the multi-fidelity GP and the standard GP are very similar. However, their main difference lies in the implementation of the covariance function. In contrast to the standard GP, the covariance functions in a multi-fidelity GP imply the autoregressive model in Eq.(2.73). This results in additional covariance sub-matrices regarding the different fidelity levels. As a consequence, we obtain an extended version of the total covariance matrix. Note that the expression for the derivative of the negative marginal log likelihood in Eq.(2.71) also holds for multi-fidelity GPs. The only exceptions are that the matrix $\mathbf{K}_y$ is computed according to Eq.(2.87) and that the parameter set in the multi-fidelity model involves $\theta_j = \left[l_L, \sigma_{fL}, l_H, \sigma_{fH}, \eta\right]$ with $\left[l_L, \sigma_{fL}\right]$ and $\left[l_H, \sigma_{fH}\right]$.

Algorithm 3 Multi-fidelity model using Gaussian Processes

1: **input**
2:     Frequencies with known LF response functions $\mathbf{f}_L$
3:     ... and known HF response functions $\mathbf{f}_H$
4:     Available LF frequency response solutions $\mathbf{h}_L$
5:     ... and HF frequency response solutions $\mathbf{h}_H$
6:     LF covariance function $\text{cov}_L(\mathbf{f}, \mathbf{f}')$
7:     HF covariance function $\text{cov}_H(\mathbf{f}, \mathbf{f}')$
8:     Noise level on the LF solutions σ_{nL}^2
9:     Noise level on the HF solutions σ_{nH}^2
10:    Frequencies at which the unknown response functions are approximated $\mathbf{f}_*$
11: **Assembly of the covariance matrix**
12:    Evaluate $\text{cov}_{LL}(\mathbf{f}_L, \mathbf{f}_L)$, $\text{cov}_{LH}(\mathbf{f}_L, \mathbf{f}_H)$, and $\text{cov}_{HH}(\mathbf{f}_H, \mathbf{f}_H)$ for the known inputs
13:    Compute $\text{cov}_{*L}(\mathbf{f}_*, \mathbf{f}_L)\text{cov}_{*H}(\mathbf{f}_*, \mathbf{f}_H)$ with one frequency set of unknown responses
14:    Evaluate $\text{cov}_{**}(\mathbf{f}_*, \mathbf{f}_*)$ with two frequency sets of unknown responses
15:    Assemble the sub-matrix $\mathbf{K}_*$ ▷ Eq.(2.83)
16:    ... the sub-matrix $\mathbf{K}$,   ▷ Eq.(2.84)
17:    ... and the sub-matrix $\mathbf{K}_{**}$ ▷ Eq.(2.85)
18:    Perform the Cholesky decomposition $\mathbf{L} := \text{chol}(\mathbf{K}_y)$
19:    Substitute the matrix inverse $\mathbf{L}^{-\mathsf{T}}\mathbf{L}^{-1} = \mathbf{K}_y^{-1}$
20: **Find the optimal LF and HF kernel parameters**
21:    Evaluate the negative marginal log likelihood $\log P(\mathbf{y}|\mathbf{f})$ ▷ Eq.(2.89)
22:    Compute the gradient of the likelihood $\partial \log P(\mathbf{y}|\mathbf{f})/\partial \theta_j$
23: **Posterior multi-fidelity GP mean and covariance**
24:    Evaluate the posterior multi-fidelity GP mean $\bar{\mathbf{h}}_*$ ▷ Eq.(2.80)
25:    Compute the posterior multi-fidelity GP covariance $\text{cov}(\mathbf{h}_*)$ ▷ Eq.(2.81)
26: **return**
27:    posterior multi-fidelity GP mean $\bar{\mathbf{h}}_*$
28:    posterior multi-fidelity GP covariance $\text{cov}(\mathbf{h}_*)$

---

3 Summary of Appended Publications

This chapter summarizes the findings of the publications Paper A [105], Paper B [139], and Paper C [140]. Moreover, the individual contributions of the authors are listed. Reprints of the full publications are given in Appendix A.

3.1 Paper A

Energy density-based non-negative surface contributions in interior acoustics

Caglar Gurbuz, Johannes Schmid, Marinus Luegmair, Steffen Marburg

Summary

Investigating vibrating surfaces as sound producing mechanisms is a continuing concern for a wide range of interior acoustic problems. In automotive acoustics, vibrations of the vehicle body lead to noise within the passenger cabin. The most prominent incident is booming noise, which occurs in the lower frequencies below $200\,\mathrm{Hz}$. Numerical methods are suitable to treat this problem, as they allow investigations in early design stages and, in contrast to experimental measurements, relatively fast predictions on the response behavior. Remarkably, the boundary element method is highly favorable for this task, since it solely requires the discretization of the cabin boundary, which is the only relevant part for the radiated sound. By this means, a contribution analysis can be performed to identify those surfaces contributing most to the acoustic objective. For that purpose, the influence coefficients, also known as acoustic transfer vectors, are computed, which account for the sensitivity of the acoustic control objective regarding the structural excitation. Typically, the sound pressure around the driver's position is used as the control objective. However, contribution analysis methods based on the sound pressure are prone to spatial variations of the evaluation point, particularly leading to deteriorated performances at either frequencies or locations with low sound pressure values.

Therefore, a contribution analysis method is developed based on sound energy densities. The sound energy density is a point-related quantity referring the energy to a specific volume. As such, it can be evaluated at an arbitrary position in the sound field. The sound energy density comprises the potential and the kinetic sound energy density. The compression of the particles creates the potential sound energy density, while the kinetic sound energy density is related to their motion. This means that the potential sound energy density is a pressure-dependent quantity, whereas the kinetic sound energy density depends on the particle velocity. Consequently, using the sound energy density as a control objective, the contribution analysis method yields accurate and robust results even in regions with low pressure values. An additional advantage of the proposed method is that the surface contributions are non-negative by definition. Acoustic short circuits due to bipolar entities are thus effectively avoided. The proposed contribution analysis is implemented in a three-dimensional boundary element formulation enabling its application to real-world industrial problems.

The booming noise problem in vehicle cabins is studied to validate the proposed method. For that purpose, the boundary element mesh of a BMW cabin is analyzed. Prior to the computation of the surface contributions, a frequency sweep analysis for the pressure response is performed to determine the relevant frequencies, at which the surface contributions are of significant interest. The first relevant frequency is adopted in a region with low sound pressures. In contrast, the second and the third relevant frequency is close

to the resonance frequency of the undamped system and in a region with higher sound pressure values, respectively.

The findings demonstrate that surfaces contributing to the sound energy density are effectively recovered, where purely pressure-based techniques have failed. This has been particularly the case at frequencies with low sound pressure values. As a consequence, the proposed method provides an accurate and, at the same time, robust technique to identify sound producing sources on vibrating structures. Future work should be undertaken to explore surfaces contributing to an entire cavity and surface contributions across a broad frequency range. Further research could also focus on the experimental realization of an energy-based contribution analysis.

Contributions

Caglar Gurbuz conceptualized and implemented the numerical algorithms. Caglar Gurbuz and Steffen Marburg derived the mathematical formulations. Caglar Gurbuz, Johannes Schmid, and Marinus Luegmair prepared the numerical models. Caglar Gurbuz performed the numerical analyses. Caglar Gurbuz drafted the manuscript. Caglar Gurbuz, Johannes Schmid, Marinus Luegmair, and Steffen Marburg discussed the results. All authors gave critical feedback and approved the final version of the manuscript.

Reference

C. Gurbuz, JD. Schmid, M. Luegmair and S. Marburg. Energy density-based non-negative surface contributions in interior acoustics. *Journal of Sound and Vibration*, 527:116824, 2022.

3.2 Paper B

Efficient analysis of energy-based surface contributions for an entire acoustic cavity

Caglar Gurbuz, Steffen Marburg

Summary

The issue of booming noise has received considerable critical attention within the field of noise, vibration, and harshness, as it poses high demands for passenger comfort. It occurs in the lower frequency range and is caused by vehicle body vibrations. The surface contribution analysis provides a valuable tool to identify the noise producing sources on the vehicle body. This technique is incorporated in a boundary element formulation and requires, thus, only a discretization of the cabin boundary. In current contribution analysis methods, the relevant acoustic quantity is evaluated at a single point, typically representing the position of the driver's ear. However, far too little attention has been paid to additional points of interest, such as the remaining passengers and the entire cabin volume. Moreover, traditional contribution analysis methods focus on the sound pressure as the relevant acoustic quantity. By doing so, the predictions of traditional techniques can significantly deviate at positions or frequencies with small sound pressures, as the sound pressure is highly susceptible to variations in the evaluated position.

This paper aims to develop a surface contribution analysis with respect to an entire acoustic cavity. For that purpose, the cumbersome integration over the volume is approximated by adopting multiple evaluation points, which are regularly distributed in the sound field. In contrast to traditional contribution analyses, the sound energy density is used as the acoustic control objective, since it is less sensitive to variations in space. The sound energy densities at distributed positions can be viewed as Gaussian integration points. Thus, the summation of these points approximates the sound energy in the acoustic cavity. Another advantage of using sound energies is that the related surface contributions are defined as a non-negative quantity. Cancellation effects in the near-field are thus inherently avoided. The volume-related contribution analysis is based on a boundary element discretization solving the three-dimensional Helmholtz equation. In this way, the surface contribution analysis can be performed for arbitrarily shaped surfaces making the proposed method readily applicable to industrial problems.

The proposed method is validated on two numerical examples. The first one involves an academic study, the inward radiating sphere. In the second case, the volume-related contribution analysis is transferred to the booming noise problem in a passenger cabin. BMW has provided the related mesh. In both studies, the number of evaluation points gradually increases from a single evaluation point, over a relatively coarse one, to a finely resolved grid of distributed field points. The surface contributions to a single point are compared to the contributions regarding the entire volume. In addition to this, the influence of the number of field points is analyzed. The final step investigates the eigenvalue distribution of the matrices associated to the energy-based surface contributions.

The results show that the surface contribution analysis can successfully identify contributing surfaces for an entire cavity. As the field points are regularly distributed, all surfaces

equally contribute in the radiating sphere problem. Regarding the vehicle booming noise problem, the volume-related contribution analysis has revealed the most active parts in the driver's footwell. In contrast, the contribution analysis related to a single point has recovered surfaces in both the front passenger's footwells and the rear of the cabin. Moreover, evidence from the findings suggests to use relatively coarse field point grids, as sufficiently accurate approximations of the contributions have already been obtained by the analysis on the coarse grid. Finally, it has been demonstrated that the eigenvalues show a decaying behavior in both numerical examples.

Contributions

Caglar Gurbuz conceptualized and implemented the numerical algorithms. Caglar Gurbuz and Steffen Marburg derived the mathematical formulations. Caglar Gurbuz performed the numerical analyses. Caglar Gurbuz drafted the manuscript. Caglar Gurbuz and Steffen Marburg discussed the results. All authors gave critical feedback and approved the final version of the manuscript.

Reference

C. Gurbuz and S. Marburg. Efficient analysis of energy-based surface contributions for an entire acoustic cavity. *Journal of Theoretical and Computational Acoustics*, 2022, accepted for publication.

3.3 Paper C

A multi-fidelity Gaussian process for efficient frequency sweeps in the acoustic design of a vehicle cabin

Caglar Gurbuz, Martin Eser, Johannes Schaffner, Steffen Marburg

Summary

The main challenge faced by many experts is the accurate and, at the same time, fast evaluation of complex acoustic systems. Recent developments in numerical methods enable accurate simulations, but usually for the burden of high computational costs and time expenses. Thus, in engineering practice, accurate numerical simulations can only be performed for a small sample size due to strict limitations on time and resources. As a consequence, highly accurate numerical simulations become impractical in studies, where a large number of simulations is required. This is typically the case in frequency sweep analyses with the boundary element method in acoustics, since the Helmholtz equation implicitly depends on the frequency. To obtain the response of an acoustic system in a broad frequency band, the boundary element simulation needs to be performed for each discrete frequency within the relevant frequency range.

This paper proposes a method for fast and accurate frequency sweep analyses. Therefore, the concept of multi-fidelity modeling, which combines models of different fidelity levels, is used. Within this concept, it is assumed that the models of the fidelity levels are linearly correlated. In a multi-fidelity model with two levels, the model with the highest accuracy is typically considered the high-fidelity model. In contrast, its representation on a lower fidelity level is adopted as the low-fidelity model. Gaussian processes are used as surrogate models for both fidelity levels to approximate the system response functions depending on the frequency. The Gaussian processes are fit to numerical results obtained from boundary element simulations. A boundary element mesh with a fine resolution is used for the high-fidelity model, while a coarse version of the same mesh is adopted as the low-fidelity model. In the spirit of a Bayesian method, Gaussian processes allow quantifying uncertainties potentially caused by limited information on the model parameters.

For the validation of the multi-fidelity Gaussian process, the booming noise problem in vehicle cabins is treated. As aforementioned, a coarse boundary element mesh of the cabin is used for the low-fidelity model, whereas the cabin with a fine mesh resolution is considered the high-fidelity model. Both meshes have been provided by BMW. In the first case, the sound pressure level at the position of the driver's ear is adopted as the control objective, while the sound energy density at the same position is analyzed in the second case. The final study assesses the computational runtime and the influences of the number of low-fidelity and high-fidelity simulations. In all studies, the approximation of the multi-fidelity model is referenced to the solution of the high-fidelity model at each frequency.

This paper's findings demonstrate the proposed method's effectiveness, as the results of the multi-fidelity model are consistent with the reference solution. This result is achieved using only a minimal number of high-fidelity simulations. On the other hand, the number

of low-fidelity simulations is relatively high. However, since the low-fidelity solutions are abundant, repetitive evaluations of the low-fidelity model are nearly negligible in terms of computational costs. By this means, the proposed method drastically reduces the total computational runtime for the entire frequency sweep. In addition, the proposed method considers uncertainties, which typically occur in the parameters of the structural excitation or the boundary admittance. Taken together, multi-fidelity Gaussian processes provide a holistic approach for the efficient and robust approximation of the frequency-dependent solution for the Helmholtz equation. As such, they alleviate the burden of excessive computational costs, while maintaining a high accuracy in the results. So far, the selection of the input frequencies is performed in a semi-empirical way. Future work should elaborate a sophisticated selection strategy for the frequencies relevant for the high-fidelity simulations. Further research should also concentrate on the correlation function between the fidelity levels and may consider the implementation of nonlinear correlations. Finally, the investigation and experimentation with various data generation sources are strongly recommended.

Contributions

Caglar Gurbuz conceptualized and implemented the numerical algorithms. Caglar Gurbuz derived the mathematical formulations. Caglar Gurbuz, Martin Eser, and Johannes Schaffner performed the parameter studies. Caglar Gurbuz drafted the manuscript. Caglar Gurbuz and Martin Eser discussed the results. All authors gave critical feedback and approved the final version of the manuscript.

Reference

C. Gurbuz, M. Eser, J. Schaffner and S. Marburg. A multi-fidelity Gaussian process for efficient frequency sweeps in the acoustic design of a vehicle cabin. *The Journal of the Acoustical Society of America*, vol. 153, no. 4, 2023.

4 Discussion and Conclusions

Vibrating structures radiate sound due to their interaction with the ambient fluid. Apart from musical instruments, the radiated sound is usually disturbing and generally perceived as noise. Consequently, an efficient diagnosis tool is required to detect radiating hot spots on vibrating surfaces. One prominent technique is the surface contribution analysis, which is primarily applied to the booming noise problem in vehicle cabins. As booming noise occurs in the low frequency range, it can be treated with wave-based numerical methods such as the finite element and the boundary element method. For this specific task, it is highly favorable to implement a contribution analysis in a boundary element formulation, since the BEM solely requires a discretization of the structural surface, which is the only relevant part in sound radiation problems. While intensity-type quantities are now well established as control objectives in exterior acoustics, experts in interior acoustic analyses still rely on the sound pressure at a specific position. The following issues are associated with this: Firstly, the sound pressure is susceptible to the position of the evaluation point. Descreased performance is mainly expected at frequencies and locations with low sound pressure values. Secondly, existing surface contribution methods are limited to a single evaluation point. Present techniques do not consider multiple evaluation points and entire volumes. Finally, investigations across a broad frequency range require repetitive evaluations of the underlying acoustic system associated with high computational costs.

The present thesis addresses the issues associated with current contribution analysis methods in interior acoustic problems. Paper A [130] provides a formulation of the surface contributions based on the sound energy density. By this means, contributing surfaces are retrieved in a robust way, as they are identified even at frequencies or locations with low sound pressure values. In addition to this, energy-based surface contributions are always non-negative by definition. This way, cancellation effects caused by positive and negative contributions are effectively avoided. While Paper A focuses on contributions to a single evaluation point, Paper B [139] extends the energy-based surface contributions for an entire volume. Regarding efficiency, the cumbersome volume integral is approximated by a finite sum over multiple evaluation points regularly distributed within the acoustic cavity. Paper C presents a multi-fidelity model in order to accelerate frequency sweep analyses for acoustic systems. In this way, repetitive evaluations of the costly high-fidelity model are approximated by combining a small sample size of high-fidelity simulations with the results of a lower fidelity version. Moreover, the proposed method is based on Gaussian process surrogates, allowing predictions under uncertainties.

Detecting sound producing sources on vibrating structures is a continuing concern in vibroacoustic systems. One prominent representative is the booming noise problem in vehicle cabins, typically treated with a contribution analysis technique. Previous research on this method is based on the influence coefficient vector describing the sensitivities of the field point sound pressure regarding structural excitation [45, 47, 49]. Although well established, this method implies two main disadvantages: Firstly, the sound pressure at a certain position is susceptible to variations of that position. As a result, it is very challenging to detect surface contributions in regions with low sound pressures. Secondly, current

methods can only retrieve contributing surfaces for excited surfaces, as the field point sound pressure is evaluated by the dot product of the influence coefficients and the structural particle velocity on the boundary [131]. The literature on exterior acoustic problems motivates the usage of intensity-type quantities as control objectives to identify sound sources on vibrating structures [66, 71]. Another physical quantity combining pressure and velocity is the sound energy or when referenced per unit volume, the sound energy density. The sound energy density comprising the pressure-proportional potential energy density and the velocity-proportional kinetic energy density has been suggested by multiple authors as a control objective for interior acoustic problems, see [3, 85, 81, 84]. Thus, Paper A introduces a contribution analysis method based on the sound energy density for three-dimensional interior acoustic problems. The energy-based surface contributions are expressed in a quadratic form resulting in only non-negative contributions. By doing so, cancellation effects from bipolar contributions are avoided. In contrast to existing techniques, the proposed method can identify contributing surfaces even in areas or at frequencies with low sound pressures. On top of that, the energy-based contribution analysis allows detecting contributions from surfaces, which are not externally excited. By this means, Paper A proposes an efficient and robust diagnosis tool to trace sound sources on vibrating surfaces. Even though Paper A focuses on the vehicle interior noise problem, the proposed method can be readily transferred to further interior acoustics problems, e.g., fuselages of traditional and electric vertical take-off and landing aircraft. With particle velocity transducers being accessible, future work could concentrate on the experimental validation of the energy-based contributions analysis. Another fruitful area for future research is the transformation of the surface contributions into the time domain enabling investigations on room impulse responses.

Current techniques on contribution analyses merely focus on the surface contributions regarding only one evaluation point. In vehicle interior noise problems, this point is typically fixed at the location of the driver's ear. However, the surface contributions regarding the other passengers still need to be considered. To the best of the author's knowledge, no existing method considers the surface contributions regarding multiple evaluation points or an entire volume. Paper B, thus, extends the surface contributions regarding an entire volume. The cavity volume is effectively approximated by using a grid of multiple regularly distributed field points. In this paper, the surface contributions are again based on the sound energy resulting in robust and, at the same time, non-negative contributions. The proposed method is initially verified with an academic numerical example, the inward radiating sphere, before its application to the vehicle interior noise problem. In both applications, the findings demonstrate that the surface contributions to the sound energy are effectively recovered. In current methods, surface contributions related to the entire cavity volume remain unconsidered. Thus, the volume-related energy surface contribution analysis enables a new perspective into the characteristics of enclosed acoustic systems. Future research should focus on the experimental validation of the proposed method. Beyond that, researchers and practitioners are encouraged to use volume-related energy surface contributions to design cabins with possibly multiple listeners. This may become particularly important in the era of autonomous driving vehicles. Further potential applications include but are not limited to the design of aircraft and train cabins.

Engineers are typically confronted with time and budget constraints in the early design phases of modern product development cycles. Consequently, numerous repeated simulations of highly accurate models, essential in optimization problems and sensitivity analyses, are usually difficult to realize. This brings engineers in very unfavorable situations, since they are challenged to make decisions under limited observations. In typical frequency sweep analyses with the BEM, the acoustic system is repetitively evaluated, as the BEM system matrices implicitly depend on the frequency. The entire analysis is associated with high computational efforts, which are amplified for large frequency bands or high frequency resolutions. One family of current techniques applies a series expansion of the Green's function to obtain frequency-independent system matrices and the model order reduction of these matrices [124, 125, 126, 127]. Another group of methods involves a reduced basis composed of successive solutions of the acoustic system through a greedy algorithm [122, 123]. However, the techniques mentioned earlier do not account for uncertainties. These are particularly important in early design stages, as their quantification enables robust and flexible predictions when only a few system observations are available. Therefore, Paper C introduces a multi-fidelity Gaussian process for accelerated frequency sweep analyses under consideration of uncertainties. In the proposed method, the two fidelity levels are realized as GPs approximating the frequency-dependent response function of the acoustic system. The response functions are obtained by solving the three-dimensional Helmholtz equation with the BEM. For this purpose, two different models are regarded as the fidelity levels: A boundary element model with a coarse mesh resolution is considered the low-fidelity model, whereas a finely resolved boundary element mesh is treated as the model with high-fidelity. By combining the accuracy of the high-fidelity model with the efficiency of its low-fidelity version, the proposed multi-fidelity model effectively reduces the computational efforts while achieving a highly accurate approximation of the frequency sweep analysis. Compared to current methods with frequency-decoupled system matrices, the series expansion of the Green's function, which is strongly dependent on the underlying problem, is avoided. In comparison with greedy reduced basis schemes, the proposed method requires only the storage of one BEM system. Thus, the related memory demands are relatively modest. On top of that, the proposed multi-fidelity model inherently considers uncertainties. These are particularly interesting to engineering applications, as they can account for manufacturing tolerances or limited information on model parameters at early design phases. However, the proposed technique relies on the fact that a lower fidelity representation of a high-fidelity model exists. Moreover, the selection of the frequencies, at which the system responses are relevant, is conducted semi-empirically with a pre-defined number of high-fidelity simulations. Lastly, it is assumed that fidelity levels are linearly correlated. So, multi-fidelity models with non-linearly correlated fidelity levels still need to be addressed in the future. Thus, the natural progression of this paper could be the implementation of non-linear correlation functions to broaden the range of applications. Apart from that, a sophisticated frequency selection strategy in the form of an *a priori* error estimator could leverage the constraints imposed by the pre-defined set of frequencies.

In conclusion, this cumulative thesis provides an efficient and robust diagnosis tool to trace sound sources on vibrating structures for interior acoustic problems. The proposed techniques are implemented in a boundary element formulation. Beyond academic ex-

amples, the proposed method has been transferred to an industrial application, where the vehicle cabin noise problem has been effectively treated. The present thesis introduces a contribution analysis technique on the basis of sound energy densities. Moreover, an extended contribution analysis method is proposed enabling investigations of surface contributions regarding an entire cavity. Finally, this thesis includes an approximation method for accelerated frequency sweep analyses under uncertainties.

Bibliography

[1] World Health Organization, *Burden of disease from environmental noise: Quantification of healthy life years lost in Europe*. World Health Organization. Regional Office for Europe, 2011.

[2] E. G. Williams, *Fourier acoustics: sound radiation and nearfield acoustical holography*. Academic press, 1999.

[3] G. H. Koopmann and J. B. Fahnline, *Designing quiet structures: a sound power minimization approach*. Elsevier, 1997.

[4] D. A. Bies, C. H. Hansen, and C. Q. Howard, *Engineering noise control*. CRC press, 2017.

[5] M. B. S. Magalhães and R. A. Tenenbaum, "Sound sources reconstruction techniques: A review of their evolution and new trends," *Acta Acustica united with Acustica*, vol. 90, no. 2, pp. 199–220, 2004.

[6] J. D. Maynard, E. G. Williams, and Y. Lee, "Nearfield acoustic holography: I. theory of generalized holography and the development of nah," *The Journal of the Acoustical Society of America*, vol. 78, no. 4, pp. 1395–1413, 1985.

[7] W. Veronesi and J. D. Maynard, "Nearfield acoustic holography (nah) ii. holographic reconstruction algorithms and computer implementation," *The Journal of the Acoustical Society of America*, vol. 81, no. 5, pp. 1307–1322, 1987.

[8] E. G. Williams, H. D. Dardy, and K. B. Washburn, "Generalized nearfield acoustical holography for cylindrical geometry: Theory and experiment," *The Journal of the Acoustical Society of America*, vol. 81, no. 2, pp. 389–407, 1987.

[9] F. Jacobsen, G. Moreno-Pescador, E. Fernandez-Grande, and J. Hald, "Near field acoustic holography with microphones on a rigid sphere (l)," *The Journal of the Acoustical Society of America*, vol. 129, no. 6, pp. 3461–3464, 2011.

[10] E. G. Williams, B. H. Houston, P. C. Herdic, S. Raveendra, and B. Gardner, "Interior near-field acoustical holography in flight," *The Journal of the Acoustical Society of America*, vol. 108, no. 4, pp. 1451–1463, 2000.

[11] P. C. Herdic, B. H. Houston, M. H. Marcus, E. G. Williams, and A. M. Baz, "The vibro-acoustic response and analysis of a full-scale aircraft fuselage section for interior noise reduction," *The Journal of the Acoustical Society of America*, vol. 117, no. 6, pp. 3667–3678, 2005.

[12] N. Valdivia and E. G. Williams, "Implicit methods of solution to integral formulations in boundary element method based nearfield acoustic holography," *The Journal of the Acoustical Society of America*, vol. 116, no. 3, pp. 1559–1572, 2004.

[13] N. Valdivia and E. G. Williams, "Krylov subspace iterative methods for boundary element method based near-field acoustic holography," *The Journal of the Acoustical Society of America*, vol. 117, no. 2, pp. 711–724, 2005.

[14] F. Jacobsen and Y. Liu, "Near field acoustic holography with particle velocity transducers," *The Journal of the Acoustical Society of America*, vol. 118, no. 5, pp. 3139–3144, 2005.

[15] G. H. Koopmann, L. Song, and J. B. Fahnline, "A method for computing acoustic fields based on the principle of wave superposition," *The Journal of the Acoustical Society of America*, vol. 86, no. 6, pp. 2433–2438, 1989.

[16] S. Lee, "The use of equivalent source method in computational acoustics," *Journal of Computational Acoustics*, vol. 25, no. 01, p. 1630001, 2017.

[17] C. Bi, X. Chen, J. Chen, and R. Zhou, "Nearfield acoustic holography based on the equivalent source method," *Science in China Ser. E Engineering & Materials Science*, vol. 48, pp. 338–354, 2005.

[18] I.-Y. Jeon and J.-G. Ih, "On the holographic reconstruction of vibroacoustic fields using equivalent sources and inverse boundary element method," *The Journal of the Acoustical Society of America*, vol. 118, no. 6, pp. 3473–3482, 2005.

[19] Y.-B. Zhang, F. Jacobsen, C.-X. Bi, and X.-Z. Chen, "Near field acoustic holography based on the equivalent source method and pressure-velocity transducers," *The Journal of the Acoustical Society of America*, vol. 126, no. 3, pp. 1257–1263, 2009.

[20] C.-X. Bi, X.-Z. Chen, and J. Chen, "Sound field separation technique based on equivalent source method and its application in nearfield acoustic holography," *The Journal of the Acoustical Society of America*, vol. 123, no. 3, pp. 1472–1478, 2008.

[21] C.-X. Bi, D.-Y. Hu, Y.-B. Zhang, and W.-Q. Jing, "Identification of active sources inside cavities using the equivalent source method-based free-field recovery technique," *Journal of Sound and Vibration*, vol. 346, pp. 153–164, 2015.

[22] N. P. Valdivia, "Advanced equivalent source methodologies for near-field acoustic holography," *Journal of Sound and Vibration*, vol. 438, pp. 66–82, 2019.

[23] E. Fernandez-Grande, A. Xenaki, and P. Gerstoft, "A sparse equivalent source method for near-field acoustic holography," *The Journal of the Acoustical Society of America*, vol. 141, no. 1, pp. 532–542, 2017.

[24] E. Fernandez-Grande and L. Daudet, "Compressive acoustic holography with block-sparse regularization," *The Journal of the Acoustical Society of America*, vol. 143, no. 6, pp. 3737–3746, 2018.

[25] J. Hald, "A comparison of iterative sparse equivalent source methods for near-field acoustical holography," *The Journal of the Acoustical Society of America*, vol. 143, no. 6, pp. 3758–3769, 2018.

[26] C.-X. Bi, Y. Liu, Y.-B. Zhang, and L. Xu, "Extension of sound field separation technique based on the equivalent source method in a sparsity framework," *Journal of Sound and Vibration*, vol. 442, pp. 125–137, 2019.

[27] J. Hald, "A comparison of compressive equivalent source methods for distributed sources," *The Journal of the Acoustical Society of America*, vol. 147, no. 4, pp. 2211–2221, 2020.

[28] C.-X. Bi, F.-M. Zhang, X.-Z. Zhang, Y.-B. Zhang, and R. Zhou, "Sound field reconstruction using block sparse bayesian learning equivalent source method," *The Journal of the Acoustical Society of America*, vol. 151, no. 4, pp. 2378–2390, 2022.

[29] M. R. Bai, "Application of bem (boundary element method)-based acoustic holography to radiation analysis of sound sources with arbitrarily shaped geometries," *The Journal of the Acoustical Society of America*, vol. 92, no. 1, pp. 533–549, 1992.

[30] B.-K. Kim and J.-G. Ih, "On the reconstruction of the vibro-acoustic field over the surface enclosing an interior space using the boundary element method," *The Journal of the Acoustical Society of America*, vol. 100, no. 5, pp. 3003–3016, 1996.

[31] A. Schuhmacher, J. Hald, K. B. Rasmussen, and P. C. Hansen, "Sound source reconstruction using inverse boundary element calculations," *The Journal of the Acoustical Society of America*, vol. 113, no. 1, pp. 114–127, 2003.

[32] T. Delillo, V. Isakov, N. Valdivia, and L. Wang, "The detection of the source of acoustical noise in two dimensions," *SIAM Journal on Applied Mathematics*, vol. 61, no. 6, pp. 2104–2121, 2001.

[33] T. DeLillo, V. Isakov, N. Valdivia, and L. Wang, "The detection of surface vibrations from interior acoustical pressure," *Inverse Problems*, vol. 19, no. 3, p. 507, 2003.

[34] N. P. Valdivia and E. G. Williams, "Study of the comparison of the methods of equivalent sources and boundary element methods for near-field acoustic holography," *The Journal of the Acoustical Society of America*, vol. 120, no. 6, pp. 3694–3705, 2006.

[35] J.-G. Ih, "Inverse boundary element techniques for the holographic identification of vibro–acoustic source parameters," *Computational Acoustics of Noise Propagation in Fluids-Finite and Boundary Element Methods*, pp. 547–572, 2008.

[36] C.-X. Bi, Y. Liu, Y.-B. Zhang, and L. Xu, "Sound field reconstruction using inverse boundary element method and sparse regularization," *The Journal of the Acoustical Society of America*, vol. 145, no. 5, pp. 3154–3162, 2019.

[37] R. Anderssohn and S. Marburg, "Nonlinear approach to approximate acoustic boundary admittance in cavities," *Journal of Computational Acoustics*, vol. 15, no. 01, pp. 63–79, 2007.

[38] M. Weber, T. Kletschkowski, and D. Sachau, "Noise source identification in a 2d cavity based on inverse finite element method," *Journal of Low Frequency Noise Vibration and Active Control*, vol. 29, pp. 147–159, 2010.

[39] T. Kletschkowski, M. Weber, and D. Sachau, "Identification of noise sources in an aircraft fuselage using an inverse method based on a finite element model," *Acta Acustica united with Acustica*, vol. 97, pp. 974–983, 2011.

[40] S. F. Wu, "On reconstruction of acoustic pressure fields using the helmholtz equation least squares method," *The Journal of the Acoustical Society of America*, vol. 107, no. 5, pp. 2511–2522, 2000.

[41] S. F. Wu, *The Helmholtz equation least-squares method*. Springer, 2015.

[42] Z. Wang and S. F. Wu, "Helmholtz equation–least-squares method for reconstructing the acoustic pressure field," *The Journal of the Acoustical Society of America*, vol. 102, no. 4, pp. 2020–2032, 1997.

[43] S. F. Wu and J. Yu, "Reconstructing interior acoustic pressure fields via helmholtz equation least-squares method," *The Journal of the Acoustical Society of America*, vol. 104, no. 4, pp. 2054–2060, 1998.

[44] S. F. Wu and L. Kumar Natarajan, "Panel acoustic contribution analysis," *The Journal of the Acoustical Society of America*, vol. 133, no. 2, pp. 799–809, 2013.

[45] S.-i. Ishiyama, M. Imai, S.-i. Maruyama, H. Ido, N. Sugiura, and S. Suzuki, "The applications of acoust/boom—a noise level predicting and reducing computer code," *SAE Transactions*, pp. 976–986, 1988.

[46] S. Suzuki, "Research on boundary element method for structural-acoustic problems," *Doctor Thesis of the Tokyo University*, 1986.

[47] R. Adey, S. Niku, J. Baynham, and P. Burns, "Predicting acoustic contributions and sensitivity. application to vehicle structures," *WIT Transactions on The Built Environment*, vol. 10, 1995.

[48] J. Trevelyan, R. Adey, and S. Niku, "Improvement of sound quality through accurate acoustic diagnostic boundary element analysis," *The Journal of the Acoustical Society of America*, vol. 98, no. 5, pp. 2873–2873, 1995.

[49] J. Coyette, H. Wynendaele, and M. Chargin, "Global acoustic sensitivity tool for improving structural design.," in *the 11 th International Modal Analysis Conference*, pp. 1389–1394, 1993.

[50] J. Dong, K. K. Choi, and N. H. Kim, "Design optimization for structural-acoustic problems using fea-bea with adjoint variable method," *J. Mech. Des.*, vol. 126, no. 3, pp. 527–533, 2004.

[51] L. Cremers, P. Guisset, L. Meulewaeter, and M. Tournour, "A computer–aided engineering method for predicting the acoustic signature of vibrating structures using discrete models," *Great Britain Patent No. GB*, vol. 16259, p. 2000, 2000.

[52] S. Marburg, "Developments in structural-acoustic optimization for passive noise control," *Archives of computational methods in engineering*, vol. 9, pp. 291–370, 2002.

[53] S. Marburg, H.-J. Hardtke, R. Schmidt, and D. Pawandenat, "Application of the concept of acoustic influence coefficients for the optimization of a vehicle roof," *Engineering analysis with boundary elements*, vol. 20, no. 4, pp. 305–310, 1997.

[54] J. Coyette, "Msc/sysnoise user's manual," *Numerical Integration Technologies, Belgium*, 1993.

[55] D.-H. Lee, W.-S. Hwang, and M.-E. Kim, "Booming noise analysis in a passenger car using a hybrid-integrated approach," *SAE transactions*, pp. 1069–1075, 2000.

[56] H. C. Seo, J. H. An, H. Kim, and J. B. Kim, "Interior noise reduction of a mini-bus using panel contribution analysis," tech. rep., 1994.

[57] W. L. Li and K. Zhao, "Prediction of structure-borne noise inside tractor cab," *SAE transactions*, pp. 67–71, 1994.

[58] Y. Huang and Z. Cui, "Recent developments for frequency domain analysis in ls-dyna®," in *Proceedings of the 11th European LS-DYNA Conference*, pp. 121–127, DYNAmore GmbH Salzburg, Austria, 2017.

[59] K. Shaposhnikov and M. J. H. Jensen, "Panel contribution analysis based on fem, bem and numerical green's function approaches," *Journal of theoretical and computational acoustics*, vol. 26, no. 03, p. 1850037, 2018.

[60] M. Mühlmeier, T. Kumbein, and N. Vogler, "Identifikation und reduzierung der flächenbeteiligungen am niederfrequenten innenraumgeräusch," *Berechnung und Simulation im Fahrzeugbau, VDI-Report*, vol. 1153, pp. 221–235, 1994.

[61] G. Koners, "Panel noise contribution analysis: an experimental method for determining the noise contributions of panels to an interior noise," tech. rep., 2003.

[62] E. Tijs, J. Wind, and D. F. Comesaña, "Fast, high resolution panel noise contribution method," tech. rep., 2011.

[63] A. Grosso, D. F. Comesana, and H.-E. De Bree, "Further development of the pnca: New panel noise contribution reference-related (pncar)," *SAE International Journal of Passenger Cars-Mechanical Systems*, vol. 5, no. 2012-01-1539, pp. 1101–1106, 2012.

[64] H.-E. De Bree and T. Basten, "Microflown based monopole sound sources for reciprocal measurements," tech. rep., 2008.

[65] O. Wolff and R. Sottek, "Panel contribution analysis-an alternative window method," tech. rep., 2005.

[66] E. G. Williams, "Supersonic acoustic intensity," *The journal of the acoustical society of America*, vol. 97, no. 1, pp. 121–127, 1995.

[67] E. G. Williams, "Supersonic acoustic intensity on planar sources," *The Journal of the Acoustical Society of America*, vol. 104, no. 5, pp. 2845–2850, 1998.

[68] M. B. S. Magalhães and R. A. Tenenbaum, "Supersonic acoustic intensity for arbitrarily shaped sources," *Acta acustica united with acustica*, vol. 92, no. 2, pp. 189–201, 2006.

[69] E. Fernandez-Grande, F. Jacobsen, and Q. Leclere, "Direct formulation of the supersonic acoustic intensity in space domain," *The journal of the acoustical society of America*, vol. 131, no. 1, pp. 186–193, 2012.

[70] E. Fernandez-Grande and F. Jacobsen, "Conservation of power of the supersonic acoustic intensity," *The Journal of the acoustical society of America*, vol. 136, no. 2, pp. 461–465, 2014.

[71] S. Marburg, E. Lösche, H. Peters, and N. Kessissoglou, "Surface contributions to radiated sound power," *The journal of the acoustical society of America*, vol. 133, no. 6, pp. 3700–3705, 2013.

[72] D. Liu, H. Peters, S. Marburg, and N. Kessissoglou, "Surface contributions to scattered sound power using non-negative intensity," *The Journal of the Acoustical Society of America*, vol. 140, no. 2, pp. 1206–1217, 2016.

[73] D. Liu, Z. Havránek, S. Marburg, H. Peters, and N. Kessissoglou, "Non-negative intensity and back-calculated non-negative intensity for analysis of directional structure-borne sound," *The Journal of the Acoustical Society of America*, vol. 142, no. 1, pp. 117–123, 2017.

[74] D. R. Wilkes, H. Peters, P. Croaker, S. Marburg, A. J. Duncan, and N. Kessissoglou, "Non-negative intensity for coupled fluid–structure interaction problems using the fast multipole method," *The Journal of the Acoustical Society of America*, vol. 141, no. 6, pp. 4278–4288, 2017.

[75] D. Liu, S. Marburg, C. Geweth, and N. Kessissoglou, "Non-negative intensity for structures with inhomogeneous damping," *Journal of Theoretical and Computational Acoustics*, vol. 27, no. 01, p. 1850050, 2019.

[76] M. Karimi, L. Maxit, V. Meyer, S. Marburg, and R. Kirby, "Non-negative intensity for planar structures under stochastic excitation," *Journal of Sound and Vibration*, vol. 488, p. 115652, 2020.

[77] D. Liu, S. Marburg, and N. Kessissoglou, "Non-negative intensity for target strength identification in marine ecosystem research," *Journal of Theoretical and Computational Acoustics*, vol. 30, no. 01, p. 2150023, 2022.

[78] E. G. Williams, "Convolution formulations for non-negative intensity," *The journal of the acoustical society of America*, vol. 134, no. 2, pp. 1055–1066, 2013.

[79] D. Liu, H. Peters, S. Marburg, and N. Kessissoglou, "Supersonic intensity and non-negative intensity for prediction of radiated sound," *The journal of the acoustical society of America*, vol. 139, no. 5, pp. 2797–2806, 2016.

[80] C. C. Junior and R. Tenenbaum, "Useful intensity: A technique to identify radiating regions on arbitrarily shaped surfaces," *Journal of sound and vibration*, vol. 332, no. 6, pp. 1567–1584, 2013.

[81] B. S. Cazzolato and C. H. Hansen, "Active control of sound transmission using structural error sensing," *The Journal of the Acoustical Society of America*, vol. 104, no. 5, pp. 2878–2889, 1998.

[82] B. S. Cazzolato, *Sensing systems for active control of sound transmission into cavities.* Dissertation, 1999.

[83] B. S. Cazzolato and C. H. Hansen, "Errors arising from three-dimensional energy density sensing in one-dimensional sound fields," *Journal of sound and vibration*, vol. 236, no. 3, pp. 375–400, 2000.

[84] N. Tanaka and K. Kobayashi, "Cluster control of acoustic potential energy in a structural/acoustic cavity," *The Journal of the Acoustical Society of America*, vol. 119, no. 5, pp. 2758–2771, 2006.

[85] S. D. Sommerfeldt and P. J. Nashif, "An adaptive filtered-x algorithm for energy-based active control," *The Journal of the Acoustical Society of America*, vol. 96, no. 1, pp. 300–306, 1994.

[86] J. P. Delhomme, "Kriging in the hydrosciences," *Advances in water resources*, vol. 1, no. 5, pp. 251–266, 1978.

[87] M. A. Oliver and R. Webster, "Kriging: a method of interpolation for geographical information systems," *International Journal of Geographical Information System*, vol. 4, no. 3, pp. 313–332, 1990.

[88] N. Cressie, "The origins of kriging," *Mathematical geology*, vol. 22, pp. 239–252, 1990.

[89] N. Cressie, *Statistics for spatial data*. John Wiley & Sons, 2015.

[90] D. J. MacKay, "Introduction to gaussian processes," *NATO ASI series F computer and systems sciences*, vol. 168, pp. 133–166, 1998.

[91] C. K. Williams and C. E. Rasmussen, *Gaussian processes for machine learning*, vol. 2. MIT press Cambridge, MA, 2006.

[92] M. Raissi, P. Perdikaris, and G. E. Karniadakis, "Machine learning of linear differential equations using gaussian processes," *Journal of Computational Physics*, vol. 348, pp. 683–693, 2017.

[93] M. Raissi, P. Perdikaris, and G. E. Karniadakis, "Numerical gaussian processes for time-dependent and nonlinear partial differential equations," *SIAM Journal on Scientific Computing*, vol. 40, no. 1, pp. A172–A198, 2018.

[94] J. Hensman, R. Mills, S. Pierce, K. Worden, and M. Eaton, "Locating acoustic emission sources in complex structures using gaussian processes," *Mechanical Systems and Signal Processing*, vol. 24, no. 1, pp. 211–223, 2010.

[95] Z.-H. Michalopoulou, P. Gerstoft, and D. Caviedes-Nozal, "Matched field source localization with gaussian processes," *JASA Express Letters*, vol. 1, no. 6, p. 064801, 2021.

[96] Z.-H. Michalopoulou and P. Gerstoft, "Matched-field geoacoustic inversion using gaussian processes for field prediction," *The Journal of the Acoustical Society of America*, vol. 150, no. 4, pp. A156–A156, 2021.

[97] C. Frederick and Z.-H. Michalopoulou, "Seabed classification and source localization with gaussian processes and machine learning," *JASA Express Letters*, vol. 2, no. 8, p. 084801, 2022.

[98] Z.-H. Michalopoulou and P. Gerstoft, "Inversion in an uncertain ocean using gaussian processes," *The Journal of the Acoustical Society of America*, vol. 153, no. 3, pp. 1600–1611, 2023.

[99] Z.-H. Michalopoulou and P. Gerstoft, "Waveform modeling with gaussian processes for inversion in ocean acoustics," *The Journal of the Acoustical Society of America*, vol. 153, no. 3_supplement, pp. A177–A177, 2023.

[100] P. Gerstoft, M. Hahmann, W. F. Jenkins, Z.-H. Michalopoulou, E. Fernandez-Grande, and C. Mecklenbrauker, "Direction of arrival estimation using gaussian process interpolation," *The Journal of the Acoustical Society of America*, vol. 152, no. 4, pp. A142–A142, 2022.

[101] Z.-H. Michalopoulou and P. Gerstoft, "Uncertainty reduction in matched field inversion using gaussian processes," *The Journal of the Acoustical Society of America*, vol. 151, no. 4, pp. A66–A66, 2022.

[102] D. Caviedes-Nozal, N. A. Riis, F. M. Heuchel, J. Brunskog, P. Gerstoft, and E. Fernandez-Grande, "Gaussian processes for sound field reconstruction," *The Journal of the Acoustical Society of America*, vol. 149, no. 2, pp. 1107–1119, 2021.

[103] C. G. Albert, "Gaussian processes for data fulfilling linear differential equations," *Multidisciplinary Digital Publishing Institute Proceedings*, vol. 33, no. 1, p. 5, 2019.

[104] C. G. Albert and K. Rath, "Gaussian process regression for data fulfilling linear differential equations with localized sources," *Entropy*, vol. 22, no. 2, p. 152, 2020.

[105] C. Gurbuz, M. Eser, J. D. Schmid, S. Marburg, and M. Luegmair, "Gaussian processes for transfer path analysis applied on vehicle body vibration problems," tech. rep., 2022.

[106] J. Jiang, G. Su, Z. Yan, Z. Zheng, and X. Hu, "Rock crack type identification by gaussian process learning on acoustic emission," *Applied Acoustics*, vol. 197, p. 108926, 2022.

[107] P. S. Craig, M. Goldstein, A. Seheult, and J. Smith, "Constructing partial prior specifications for models of complex physical systems," *Journal of the Royal Statistical Society: Series D*, vol. 47, no. 1, pp. 37–53, 1998.

[108] M. C. Kennedy and A. O'Hagan, "Predicting the output from a complex computer code when fast approximations are available," *Biometrika*, vol. 87, no. 1, pp. 1–13, 2000.

[109] L. Le Gratiet, *Multi-fidelity Gaussian process regression for computer experiments*. PhD thesis, Université Paris-Diderot-Paris VII, 2013.

[110] L. Le Gratiet and J. Garnier, "Recursive co-kriging model for design of computer experiments with multiple levels of fidelity," *International Journal for Uncertainty Quantification*, vol. 4, no. 5, 2014.

[111] L. Parussini, D. Venturi, P. Perdikaris, and G. E. Karniadakis, "Multi-fidelity gaussian process regression for prediction of random fields," *Journal of Computational Physics*, vol. 336, pp. 36–50, 2017.

[112] L. Bonfiglio, P. Perdikaris, G. Vernengo, J. S. de Medeiros, and G. Karniadakis, "Improving swath seakeeping performance using multi-fidelity gaussian process and bayesian optimization," *Journal of Ship Research*, vol. 62, no. 04, pp. 223–240, 2018.

[113] L. Bonfiglio, P. Perdikaris, S. Brizzolara, and G. Karniadakis, "Multi-fidelity optimization of super-cavitating hydrofoils," *Computer Methods in Applied Mechanics and Engineering*, vol. 332, pp. 63–85, 2018.

[114] K. Cutajar, M. Pullin, A. Damianou, N. Lawrence, and J. González, "Deep gaussian processes for multi-fidelity modeling," *arXiv preprint arXiv:1903.07320*, 2019.

[115] M. Raissi and G. Karniadakis, "Deep multi-fidelity gaussian processes," *arXiv preprint arXiv:1604.07484*, 2016.

[116] M. Raissi, P. Perdikaris, and G. E. Karniadakis, "Inferring solutions of differential equations using noisy multi-fidelity data," *Journal of Computational Physics*, vol. 335, pp. 736–746, 2017.

[117] P. Perdikaris, M. Raissi, A. Damianou, N. D. Lawrence, and G. E. Karniadakis, "Nonlinear information fusion algorithms for data-efficient multi-fidelity modelling," *Proceedings of the Royal Society A: Mathematical, Physical and Engineering Sciences*, vol. 473, no. 2198, p. 20160751, 2017.

[118] M. Guo, A. Manzoni, M. Amendt, P. Conti, and J. S. Hesthaven, "Multi-fidelity regression using artificial neural networks: efficient approximation of parameter-dependent output quantities," *Computer methods in applied mechanics and engineering*, vol. 389, p. 114378, 2022.

[119] X. Meng and G. E. Karniadakis, "A composite neural network that learns from multi-fidelity data: Application to function approximation and inverse pde problems," *Journal of Computational Physics*, vol. 401, p. 109020, 2020.

[120] M. Torzoni, A. Manzoni, and S. Mariani, "A deep neural network, multi-fidelity surrogate model approach for bayesian model updating in shm," in *European Workshop on Structural Health Monitoring: EWSHM 2022-Volume 2*, pp. 1076–1086, Springer, 2022.

[121] M. Torzoni, A. Manzoni, and S. Mariani, "A multi-fidelity surrogate model for structural health monitoring exploiting model order reduction and artificial neural networks," *Mechanical Systems and Signal Processing*, vol. 197, p. 110376, 2023.

[122] S. K. Baydoun, M. Voigt, C. Jelich, and S. Marburg, "A greedy reduced basis scheme for multifrequency solution of structural acoustic systems," *International Journal for Numerical Methods in Engineering*, vol. 121, no. 2, pp. 187–200, 2020.

[123] C. Jelich, S. Koji Baydoun, M. Voigt, and S. Marburg, "A greedy reduced basis algorithm for structural acoustic systems with parameter and implicit frequency dependence," *International Journal for Numerical Methods in Engineering*, vol. 122, no. 24, pp. 7409–7430, 2021.

[124] D. Panagiotopoulos, E. Deckers, and W. Desmet, "Krylov subspaces recycling based model order reduction for acoustic bem systems and an error estimator," *Computer Methods in Applied Mechanics and Engineering*, vol. 359, p. 112755, 2020.

[125] D. Panagiotopoulos, W. Desmet, and E. Deckers, "Parametric model order reduction for acoustic boundary element method systems through a multiparameter krylov subspaces recycling strategy," *International Journal for Numerical Methods in Engineering*, vol. 123, no. 22, pp. 5546–5569, 2022.

[126] X. Xie and Y. Liu, "Efficient multi-frequency solutions of fe–be coupled structural–acoustic problems using arnoldi-based dimension reduction approach," *Computer Methods in Applied Mechanics and Engineering*, vol. 386, p. 114126, 2021.

[127] X. Xie and Y. Liu, "An adaptive model order reduction method for boundary element-based multi-frequency acoustic wave problems," *Computer Methods in Applied Mechanics and Engineering*, vol. 373, p. 113532, 2021.

[128] S. Marburg and B. Nolte, *Computational acoustics of noise propagation in fluids: finite and boundary element methods*, vol. 578. Springer, 2008.

[129] L. E. Kinsler, A. R. Frey, A. B. Coppens, and J. V. Sanders, "The acoustic wave equation and simple solutions," *Fundamentals of acoustics. Hoboken: Wiley*, pp. 113–48, 2000.

[130] C. Gurbuz, J. D. Schmid, M. Luegmair, and S. Marburg, "Energy density-based non-negative surface contributions in interior acoustics," *Journal of Sound and Vibration*, vol. 527, p. 116824, 2022.

[131] S. Marburg, *Boundary element method for time-harmonic acoustic problems*. Springer, 2018.

[132] J. R. Silva, L. Wrobel, and J. Telles, "A new family of continuous/discontinuous three-dimensional boundary elements with application to acoustic wave propagation," *International journal for numerical methods in engineering*, vol. 36, no. 10, pp. 1661–1679, 1993.

[133] J. do Rego Silva, *Acoustic and elastic wave scattering using boundary elements*, vol. 18. Computational mechanics, 1994.

[134] T. Wu and A. Seybert, "A weighted residual formulation for the chief method in acoustics," *The Journal of the Acoustical Society of America*, vol. 90, no. 3, pp. 1608–1614, 1991.

[135] E. Hüllermeier and W. Waegeman, "Aleatoric and epistemic uncertainty in machine learning: An introduction to concepts and methods," *Machine Learning*, vol. 110, no. 3, pp. 457–506, 2021.

[136] R. Von Mises, *Mathematical theory of probability and statistics*. Academic press, 2014.

[137] C. M. Bishop and N. M. Nasrabadi, *Pattern recognition and machine learning*, vol. 4. Springer, 2006.

[138] K. P. Murphy, *Machine learning: a probabilistic perspective*. MIT press, 2012.

[139] C. Gurbuz and S. Marburg, "Efficient analysis of energy-based surface contributions for an entire acoustic cavity," *Journal of Theoretical and Computational Acoustics*, 2022.

[140] C. Gurbuz, M. Eser, J. Schaffner, and S. Marburg, "A multi-fidelity gaussian process for efficient frequency sweeps in the acoustic design of a vehicle cabin," *The Journal of the Acoustical Society of America*, vol. 153, no. 4, pp. 2006–2018, 2023.

A Appended Publications

A.1 Paper A

Energy density-based non-negative surface contributions in interior acoustics

Caglar Gurbuz, Johannes D. Schmid, Marinus Luegmair, and Steffen Marburg

Energy density-based non-negative surface contributions in interior acoustics

Caglar Gurbuz [a],[*], Johannes D. Schmid [a], Marinus Luegmair [b], Steffen Marburg [a]

[a] *Chair of Vibroacoustics of Vehicles and Machines, Technical University of Munich, Garching, 85748, Germany*
[b] *BMW AG, Munich, 80333, Germany*

ARTICLE INFO

ABSTRACT

Vibrating structures have received considerable critical attention as they radiate sound into enclosures where it is amplified by reflections. Surface and panel contribution analyses account for a useful tool to identify sound sources on vibrating structures. Current commercial solutions use the sound pressure at a field point inside the acoustic domain as the objective function. Usually, a bar chart of panel contributions to the sound pressure at a single point is supplied. A major drawback consists in the sound pressure strongly depending on the location of the specific field point. This is particularly the case for field point locations in regions with low sound pressure values. It is the aim of this study to formulate sound energy density-based surface contributions to evaluate the energy flow in enclosing structures. These energy-based contributions offer new insights into the properties of acoustic cavities, since they account for an integrative evaluation of the sound pressure and the particle velocity. For this purpose, the boundary element method has been applied to solve the three-dimensional Helmholtz equation for interior acoustics. In analogy to the non-negative intensity, the energy-based contributions are expressed in a quadratic form. By this means, acoustic cancellation effects due to alternating signs are bypassed. The results reveal regions with high contributions to the sound energy density at specific field points. Some of these surface regions appear almost inactive if only the contributions to the sound pressure were analyzed. The findings of this study indicate that energy-based surface contributions provide an effective quantity, particularly in regions with low sound pressure values.

1. Introduction

Vibration patterns on structures are widely considered to be a crucial factor in acoustic noise problems. In particular, interior acoustic problems have been the subject of many engineering applications including vehicle cabins, aircraft fuselages, and closed rooms. Experts in this field are faced with the challenge to identify those surfaces of the structure which contribute most to the radiated sound in certain regions inside the acoustic domain.

Over the past four decades, there has been a growing interest in surface or panel contribution analysis, particularly arising in the automotive industry. The first systematic report on contribution analysis was carried out in 1988 by Ishiyama et al. [1]. They presented a formulation based on boundary element method (BEM) system matrices to determine the sound pressure at a certain location, e.g., at the driver's ear. By this means, the sound pressure was determined by a scalar product of two vectors: the particle velocity vector and the coefficient vector associated with the transfer function between the field point and a particular node of the

boundary element mesh. Note that this transfer function should be understood as a discrete, and thus, mesh dependent function which can be easily transformed into a continuous, and thus, mesh independent function, see for example [2,3].

Many definitions of this coefficient vector can be found, e.g., acoustic contributions [4], global sensitivities with respect to the particle velocity [5], sensitivity associated with the adjoint variable method [6], and influence coefficients [2,3]. Since the patent by Cremers et al. [7] was filed in 2000, the term acoustic transfer vector (ATV) has been widely used. It refers to the discrete coefficient vector, which is associated with the nodal contributions. ATVs are commonly adopted in current finite element method (FEM) codes, e.g., MSC Nastran [8] or LS-DYNA [9], to perform panel contribution analyses. More recent evidence [10] reports on a numerical panel contribution analysis suitable for the BEM and the finite element method (FEM). The authors developed a numerical Green's function approach to evaluate the interaction between the vibrating structure and the sound pressure at an internal field point.

Initial work in this field with experimental techniques focused primarily on the interior noise in car cabins. Muhlmeier et al. [11] developed a method by measuring the contribution of each chassis panel to the sound pressure at the driver's position, whereas Koners [12] reported on a method based on transfer path analysis.

Besides surface or panel contribution analyses, the following approaches have been proposed to tackle the acoustic inverse problem: near-field acoustic holography (NAH), inverse BEM, inverse FEM, equivalent source methods (ESM), and far-field holography. In NAH, sound pressure measurements on a two-dimensional surface, the hologram, are performed to reconstruct the three-dimensional acoustic field. By convolving the measured data with the Green's function, the vibration pattern of the structure can be identified [13]. The inverse BEM designates a technique to recover vibrating surfaces contributing to the measured sound pressure data. However, inverse problems are challenging due to the ill-posed nature of the acoustic transfer matrices. In an attempt to solve this issue, regularization methods such as Tikhonov regularization [14], truncated singular value decomposition [15], or Krylov subspace methods [16] were extensively studied. The principle idea of the equivalent source method (ESM) is to identify surface contributions by replicating arbitrary sound sources with arrays of elementary sound sources [17,18]. As such, ESM methods were integrated in inverse BEM [19,20] and NAH [21] schemes in order to leverage the singularities in the acoustic transfer matrix. In the Helmholtz least-squares (HELS) method, the sound field obtained from a BEM simulation is reconstructed by a spherical wave expansion, whose coefficients are determined by the least-squares method satisfying the sound pressure at the measurement points [22–24]. Magalhaes and Tenenbaum have traced the advances in this topic until 2004 [25].

Regarding interior acoustics, NAH was performed to recover the particle velocity in an aircraft fuselage [26]. The inverse BEM was applied in interior acoustics to reconstruct the vibration pattern in an automotive cabin [27]. Further applications on interior acoustics using the inverse FEM have been reported for two-dimensional cavities [28] and industrial aircraft fuselages [29]. The effectiveness of an ESM-based NAH technique was demonstrated for monopole [30] and dipole sources [31] in enclosed domains. For cylindrical objects, a hybrid scheme combining the HELS method with the NAH was studied [32]. Moreover, a panel contribution analysis based on the HELS was developed for interior acoustic problems [33]. All the studies mentioned above have tended to focus on the sound pressure at an internal field point as the objective function.

In a major advance, Williams [34] introduced the supersonic intensity (SSI) as a new quantity. He concluded that only supersonic wave components contribute to the far field, since subsonic components are evanescent in the near field. As such, he suggests to use the SSI rather than the sound intensity for exterior acoustic problems. This concept has been extended to arbitrarily shaped structures [35] and formulated in the wavenumber [34] as well as in the space domain [36].

Marburg et al. [37] introduced the non-negative contributions for exterior acoustic problems. This quantity can be interpreted as a non-negative intensity (NNI) to evaluate the surface contributions in sound radiation problems. As the NNI is always positive, cancellation effects due to the alternating sign inherent to acoustic intensities are circumvented. Correa and Tenenbaum [38] proposed a similar formulation by introducing a quantity called useful intensity. To determine the relevant regions for radiation, Correa and Tenenbaum used the acoustic radiation modes (ARM) as a filtering operator whereas Marburg et al. used the ARM to compute the square root of the acoustic impedance matrix. Another approach to determine the NNI for planar structures based on convolution formulas was derived by Williams [39]. In contrast to the SSI, data on either sound pressure or particle velocity suffice to compute the NNI. A comparative study has shown that the SSI equals the NNI for certain parameters of the spatial radiation filter [40]. Moreover, the NNI formulation was extended to scattered sound power [41] and back-calculations from partially enveloping surfaces at the far-field [42]. Further applications of the NNI include coupled fluid–structure interactions at large scale [43,44], stochastic excitations due to turbulent boundary layers or acoustic diffuse fields [45], and the reconstruction of vibrating surfaces in the presence of inhomogeneous damping [46].

Regarding interior acoustic problems, Sommerfeldt and Nashif [47] draw our attention to an energy density-based approach for global control. They have highlighted the deteriorated performance of sound pressure measurements when microphones are placed in so-called localized silent zones [47]. The authors bypassed this issue with an energy-based approach, as the sound energy is sensitive to both the sound pressure and the particle velocity [47]. Tanaka and Kobayashi [48] have taken advantage of this fact to develop a control concept for acoustic cavities based on active noise and active vibration control. Energy-based methods have been further applied on acoustically optimized designs [49] and on the active control of sound transmission into cavities [50–52].

Previous work on surface and panel contribution analysis in interior domains only focused on the sound pressure as an objective function. However, sound pressure-based surface contributions are strongly dependent on spatial variation of the field point location. This leads to a deterioration when the sound pressure is analyzed in regions with extremely low sound pressure values [48,50].

To the best of our knowledge, there are no results in the literature regarding a numerical method to evaluate surface contributions on the basis of the sound energy in cavities.

The aim of the present work is to formulate a numerical, energy-based contribution analysis to evaluate the acoustic properties in interior domains. In this context, we present a methodology to determine the sound energy flow in enclosing surfaces regarding
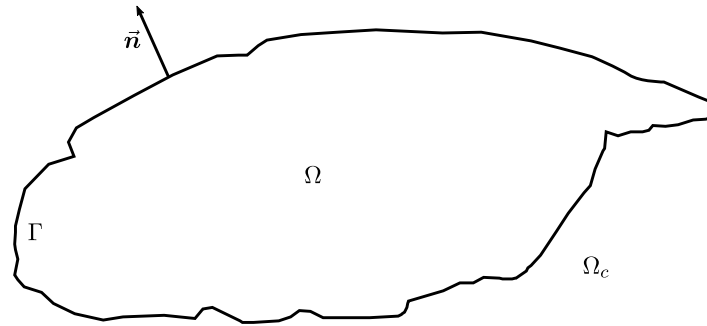
Fig. 1. Helmholtz problem with the interior domain Ω and the boundary Γ. The normal vector $\vec{n}$ points outward into the complementary domain Ω_c.

the sound energy density at an internal field point. Therefore, we have employed the energy density-based concept suggested by Sommerfeldt and Nashif [47] or Koopmann and Fahnline [49]. In analogy to the NNI, we formulated a quadratic expression for the acoustic energy which leads to real-valued, non-negative surface contributions [37].

The results of this method are encouraging, as they show that surface contributions can be identified in regions with low sound pressure values too. The proposed method provides a valuable analysis tool to reconstruct vibration patterns on structures in interior acoustic problems.

The paper is organized as follows: Section 2 briefly surveys the boundary element method to solve the three-dimensional Helmholtz equation. Section 3 outlines the evaluation of the acoustic quantities at a field point. In Section 4, our formulation on energy density-based surface contributions is described. Section 5 presents its application on a numerical example. Our conclusions are drawn in Section 6.

2. Boundary element method

The brief outline of the boundary element method in this section is closely related to former introductions [53,54]. By assuming a harmonic time dependency function $e^{-i\omega t}$, sound radiation problems are governed by the Helmholtz equation

$$\Delta p(\vec{x}) + k^2 p(\vec{x}) = 0 \qquad x \in \Omega \subset \mathbb{R}^3, \tag{1}$$

with $p(\vec{x})$ denoting the scalar, complex-valued sound pressure in the acoustic domain Ω and $k = \omega/c$ the wavenumber, which is composed by the angular frequency ω and the speed of sound c. The regarding Neumann boundary condition is related to the derivative of the sound pressure in normal direction

$$v_f(\vec{x}) = \frac{1}{i\omega\rho} \frac{\partial p(\vec{x})}{\partial n(\vec{x})}, \tag{2}$$

where $v_f(\vec{x})$ represents the fluid particle velocity at the boundary of the acoustic domain Γ and ρ the ambient density of the fluid. The boundary admittance of the acoustic system is posed by the Robin boundary condition as

$$v_f(\vec{x}) - v_s(\vec{x}) = Y(\vec{x}) p(\vec{x}) \qquad x \in \Gamma \subset \mathbb{R}^2, \tag{3}$$

where $v_s(\vec{x})$ and $Y(\vec{x})$ denote the structural particle velocity and the boundary admittance, respectively. Note that the Robin boundary condition degenerates to a Neumann boundary condition for $Y(\vec{x}) = 0$. Fig. 1 illustrates the Helmholtz problem for interior acoustics [54].

By combining the weak form of the Helmholtz equation with the fundamental solution, we deduce the following boundary integral equation:

$$c(\vec{y}) p(\vec{y}) + \int_\Gamma \frac{\partial G(\vec{x}, \vec{y})}{\partial n(\vec{x})} p(\vec{x}) \mathrm{d}\Gamma(\vec{x}) = i\omega\rho \int_\Gamma G(\vec{x}, \vec{y}) v_f(\vec{x}) \mathrm{d}\Gamma(\vec{x}), \tag{4}$$

with $G(\vec{x}, \vec{y})$ denoting the Green's function and $c(\vec{y})$ a quantity representing the geometric composition of the boundary Γ at $\vec{y}$ [53,54]. For three-dimensional Helmholtz problems, the Green's functions is defined by $G(\vec{x}, \vec{y}) = e^{ikr}/(4\pi r)$ with the distance $r = r(\vec{x}, \vec{y})$. By this means, it describes the effect of a monopole source at $\vec{y}$ on a receiver at the position $\vec{x}$. On smooth surfaces, e.g., inside a boundary element, we obtain $c(\vec{y}) = 0.5$ [54].

Finally, substitution of the Robin boundary condition (Eq. (3)) into Eq. (4) and discretization with the collocation boundary element method result in the following linear system of equations:

$$(\boldsymbol{H} - \boldsymbol{G}\boldsymbol{Y})\boldsymbol{p} = \boldsymbol{G}\boldsymbol{v}_s, \tag{5}$$

with $\boldsymbol{G}$ and $\boldsymbol{H}$ denoting the global system matrices derived from the single-layer and the double-layer potential, respectively. Note that $\boldsymbol{G}$ and $\boldsymbol{H}$ are neither Hermitian nor positive definite. By assuming piecewise constant approximation functions for the admittance and discontinuous approximations for the sound pressure, the boundary admittance matrix $\boldsymbol{Y}$ contains only entries on the diagonal [54].
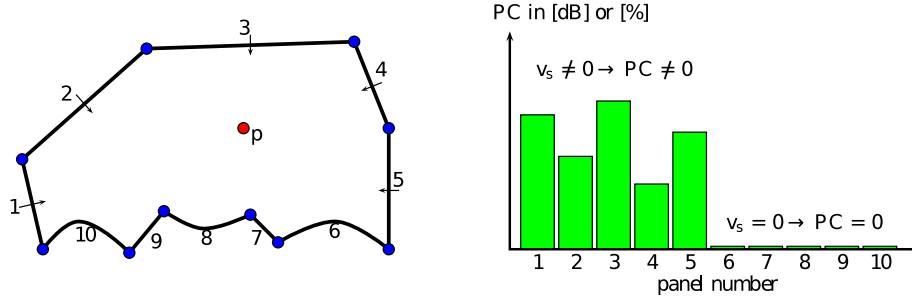
Fig. 2. Two-dimensional cavity surrounded by ten panels (left). The sound pressure is evaluated at the field point (red). The panel contributions are visualized by a bar chart (right). Only panels with non-zero surface particle velocities contribute to the field point. (For interpretation of the references to color in this figure legend, the reader is referred to the web version of this article.)

3. Field point evaluation

Once the matrix system in Eq. (5) is solved, the sound pressure and the particle velocity are known on the boundary. To evaluate the sound pressure inside the domain, we reformulate Eq. (4) including the Robin boundary condition Eq. (3)

$$
\begin{aligned}
p(\vec{y}) = \mathrm{i}\omega\rho \int_{\Gamma} & G(\vec{x}, \vec{y}) v_s(\vec{x}) \mathrm{d}\Gamma(\vec{x}) \\
& - \int_{\Gamma} \left[\frac{\partial G(\vec{x}, \vec{y})}{\partial n(\vec{x})} - \mathrm{i}\omega\rho\, G(\vec{x}, \vec{y}) Y(\vec{x}) \right] p(\vec{x}) \mathrm{d}\Gamma(\vec{x}) \qquad \vec{y} \in \Omega,
\end{aligned}
\tag{6}
$$

where $p(\vec{y})$ expresses the sound pressure at the field point $\vec{y}$. In discrete form, the sound pressure at a field point is evaluated by

$$
p(\vec{y}) = \boldsymbol{g}^T(\vec{y}) \boldsymbol{v}_s - \left[\boldsymbol{h}^T(\vec{y}) - \boldsymbol{g}^T(\vec{y}) \boldsymbol{Y} \right] \boldsymbol{p} \qquad \vec{y} \in \Omega.
\tag{7}
$$

By substituting the sound pressure solution on the boundary (Eq. (5)) in Eq. (7), we obtain

$$
\begin{aligned}
p(\vec{y}) &= \left\{ \boldsymbol{g}^T(\vec{y}) - \left[\boldsymbol{h}^T(\vec{y}) - \boldsymbol{g}^T(\vec{y}) \boldsymbol{Y} \right] (\boldsymbol{H} - \boldsymbol{G}\boldsymbol{Y})^{-1} \boldsymbol{G} \right\} \boldsymbol{v}_s \\
&= \boldsymbol{b}^T(\vec{y}) \boldsymbol{v}_s \qquad \vec{y} \in \Omega,
\end{aligned}
\tag{8}
$$

with the column matrix $\boldsymbol{b}(\vec{y})$ also known as the acoustic transfer vector. [54,55]

To obtain the particle velocity at the field point, we make use of the relation in Eq. (2). By this means, the gradient of the sound pressure in Eq. (6) yields the field point particle velocity [56]

$$
\begin{aligned}
\vec{\boldsymbol{v}}(\vec{y}) &= \frac{1}{\mathrm{i}\omega\rho} \vec{\nabla} p(\vec{y}) \\
&= \int_{\Gamma} \vec{\nabla} G(\vec{x}, \vec{y}) v_s(\vec{x}) \mathrm{d}\Gamma(\vec{x}) \\
&\quad - \left[\int_{\Gamma} \vec{\nabla} \frac{1}{\mathrm{i}\omega\rho} \frac{\partial G(\vec{x}, \vec{y})}{\partial n(\vec{x})} - \vec{\nabla} G(\vec{x}, \vec{y}) Y(\vec{x}) \right] p(\vec{x}) \mathrm{d}\Gamma(\vec{x}) \qquad \vec{y} \in \Omega.
\end{aligned}
\tag{9}
$$

In discrete form, the field point particle velocity reads

$$
\begin{aligned}
v(\vec{y}) &= \left\{ \boldsymbol{g}_j^T(\vec{y}) - \left[\boldsymbol{h}_j^T(\vec{y}) - \boldsymbol{g}_j^T(\vec{y}) \boldsymbol{Y} \right] (\boldsymbol{H} - \boldsymbol{G}\boldsymbol{Y})^{-1} \boldsymbol{G} \right\} \boldsymbol{v}_s \\
&= \boldsymbol{b}_j^T(\vec{y}) \boldsymbol{v}_s \qquad \vec{y} \in \Omega,
\end{aligned}
\tag{10}
$$

with the column matrix $\boldsymbol{b}_j(\vec{y})$ denoting the influence coefficient vector regarding the spatial component j of the particle velocity [54].

These influence coefficients $\boldsymbol{b}$, Eq. (8), and $\boldsymbol{b}_j$, Eq. (10), can be understood as the sensitivity of the sound pressure or the particle velocity at the point $\vec{y}$ with respect to the surface particle velocity.

Note that the traditional panel contribution (PC) analysis is assessed by evaluating Eq. (8)

$$
p(\vec{y}) = \boldsymbol{b}^T(\vec{y}) \boldsymbol{v}_s = \sum_{j=1}^{N_n} \eta_j \qquad \vec{y} \in \Omega,
\tag{11}
$$

with N_n denoting the number of nodes and η_j the surface or panel contribution of an arbitrary node j to the sound pressure at the field point $\vec{y}$. Usually, these panel contributions are visualized by means of a bar chart. A schematic overview of the traditional analysis is depicted in Fig. 2. In this figure, the boundary of the acoustic domain is subdivided in ten panels (left). The contributions of these panels regarding the sound pressure at the field point are illustrated in a bar chart. Note that only panels where the surface particle velocity is non-zero contribute to the sound pressure at the field point, see Eq. (11).

4. Energy density-based surface contributions

Two forms of energy are transported in sound waves: the potential energy due to the compression of the fluid particles and the kinetic energy decisive for the particle motion. The potential energy E_p and the kinetic energy E_k are posed in terms of the sound pressure p and the particle velocity v as follows:

$$E_p = \frac{1}{2\rho c^2} \int_\Omega p(\vec{x})^2 \, \mathrm{d}\Omega, \tag{12}$$

$$E_k = \frac{\rho}{4} \int_\Omega \vec{v}_f(\vec{x}) \cdot \vec{v}_f(\vec{x})^* \, \mathrm{d}\Omega, \tag{13}$$

with $()^*$ denoting the complex conjugate operation. Summation of the potential energy and the kinetic energy results in the total acoustic energy [49,57]

$$E_t = E_p + E_k = \frac{1}{2\rho c^2} \int_\Omega p(\vec{x})^2 \, \mathrm{d}\Omega + \frac{\rho}{4} \int_\Omega \vec{v}_f(\vec{x}) \cdot \vec{v}_f(\vec{x})^* \, \mathrm{d}\Omega. \tag{14}$$

The energy density, which is defined as the energy per unit volume, can be evaluated at discrete positions in the acoustic field. As such, the potential energy density e_p, the kinetic energy density e_k and the total energy density e_t at $\vec{y} \in \Omega$ read

$$e_p(\vec{y}) = \frac{1}{2\rho c^2} p^*(\vec{y}) p(\vec{y}), \tag{15}$$

$$e_k(\vec{y}) = \frac{\rho}{4} \vec{v}^*(\vec{y}) \vec{v}(\vec{y}), \tag{16}$$

$$e_t(\vec{y}) = e_p(\vec{y}) + e_k(\vec{y}). \tag{17}$$

The sound pressure p and the particle velocity vector $\vec{v}$ at the interior field point are evaluated according to Eqs. (8) and (10), respectively. Note that the energy density has units of energy per volume $[\mathrm{kg/ms}^2]$ [47,48,52].

By substituting Eq. (8) into Eq. (15) and omitting the indication of $\vec{y}$-dependence, we can rewrite the potential energy density in a quadratic form

$$e_p = \frac{1}{2\rho c^2} (\boldsymbol{b}^T \boldsymbol{v}_s)^* (\boldsymbol{b}^T \boldsymbol{v}_s) = \frac{1}{2\rho c^2} \boldsymbol{v}_s^H \boldsymbol{b}^* \boldsymbol{b}^T \boldsymbol{v}_s = \boldsymbol{v}_s^H \boldsymbol{A}_p \boldsymbol{v}_s, \tag{18}$$

with $()^H$ denoting the complex conjugate transpose operation. The coupling matrix $\boldsymbol{A}_p$ regarding the potential energy density is of rank one leading to only one non-zero eigenvalue. Combining Eq. (16) with Eq. (10) yields the quadratic form for the kinetic energy density

$$e_k = \frac{\rho}{4} (\boldsymbol{b}_j^T \boldsymbol{v}_s)^* (\boldsymbol{b}_j^T \boldsymbol{v}_s) = \frac{\rho}{4} \boldsymbol{v}_s^H \boldsymbol{b}_j^* \boldsymbol{b}_j^T \boldsymbol{v}_s = \boldsymbol{v}_s^H \boldsymbol{A}_k \boldsymbol{v}_s, \tag{19}$$

where $\boldsymbol{A}_k$ identifies the coupling matrix regarding the kinetic energy density. With a rank of three, the matrix $\boldsymbol{A}_k$ has exactly three non-zero eigenvalues. We obtain the quadratic form for the total energy density by adding Eqs. (18) and (19)

$$e_t = e_p + e_k = \frac{1}{2\rho c^2} p_i^* p_i + \frac{\rho}{4} \vec{v}_i^H \vec{v}_i = \boldsymbol{v}_s^H \boldsymbol{A}_p \boldsymbol{v}_s + \boldsymbol{v}_s^H \boldsymbol{A}_k \boldsymbol{v}_s = \boldsymbol{v}_s^H \boldsymbol{A}_t \boldsymbol{v}_s \tag{20}$$

with the coupling matrix $\boldsymbol{A}_t$ with respect to the total energy density. The matrix $\boldsymbol{A}_t$ is of rank four resulting in four non-zero eigenvalues. Note that the coupling matrices $\boldsymbol{A}_p$, $\boldsymbol{A}_k$, and $\boldsymbol{A}_t$ are all Hermitian and complex-valued. The related eigenvalues are thus positive and real-valued.

To compute the energy density based surface contributions μ_j, we need to decompose the coupling matrix $\boldsymbol{A}$

$$e = \boldsymbol{v}_s^H \boldsymbol{A} \boldsymbol{v}_s = \boldsymbol{v}_s^H \sqrt{\boldsymbol{A}}^H \sqrt{\boldsymbol{A}} \boldsymbol{v}_s = \sum_{j=1}^{N_n} \alpha_j^* \alpha_j = \sum_{j=1}^{N_n} \mu_j, \tag{21}$$

with α_j denoting a discrete entity on an arbitrary interpolation node j. Note that the energy density e and the coupling matrix $\boldsymbol{A}$ from the equation above are representative for the potential, the kinetic, and the total sound energy. Regarding the matrix square root $\sqrt{\boldsymbol{A}}$, we first solve the following eigenvalue problem

$$\boldsymbol{A} = \boldsymbol{\Psi}^H \boldsymbol{\Lambda} \boldsymbol{\Psi} \tag{22}$$

with the eigenvectors $\boldsymbol{\Psi}$ and eigenvalues $\boldsymbol{\Lambda} = \mathrm{diag}\{\lambda_k\}$. Second, we make use of the fact that the eigenvalues of the Hermitian matrix $\boldsymbol{A}$ are real-valued and positive. This allows the formal expression $\sqrt{\boldsymbol{\Lambda}} = \mathrm{diag}\{\sqrt{\lambda_k}\}$. By exploiting the normalization condition for eigenvectors $\boldsymbol{\Psi} \boldsymbol{\Psi}^H = \boldsymbol{I}$, Eq. (22) can be then reformulated to

$$\boldsymbol{A} = \boldsymbol{\Psi}^H \sqrt{\boldsymbol{\Lambda}}^H \sqrt{\boldsymbol{\Lambda}} \boldsymbol{\Psi} = \boldsymbol{\Psi}^H \sqrt{\boldsymbol{\Lambda}}^H \boldsymbol{\Psi} \boldsymbol{\Psi}^H \sqrt{\boldsymbol{\Lambda}} \boldsymbol{\Psi} = \sqrt{\boldsymbol{A}}^H \sqrt{\boldsymbol{A}}. \tag{23}$$

The square root of the matrix $\boldsymbol{A}$ can be now computed by $\sqrt{\boldsymbol{A}} = \boldsymbol{\Psi}^H \sqrt{\boldsymbol{\Lambda}} \boldsymbol{\Psi}$. In the final step, we formulate the energy density-based surface contributions by incorporating Eq. (23) in Eqs. (18)–(20)

$$e_p = \boldsymbol{v}_s^H \boldsymbol{A}_p \boldsymbol{v}_s = \boldsymbol{v}_s^H \sqrt{\boldsymbol{A}_p}^H \sqrt{\boldsymbol{A}_p} \boldsymbol{v}_s = \sum_{j=1}^{N_n} \alpha_{p_j}^* \alpha_{p_j} = \sum_{j=1}^{N_n} \mu_{p_j}, \tag{24}$$
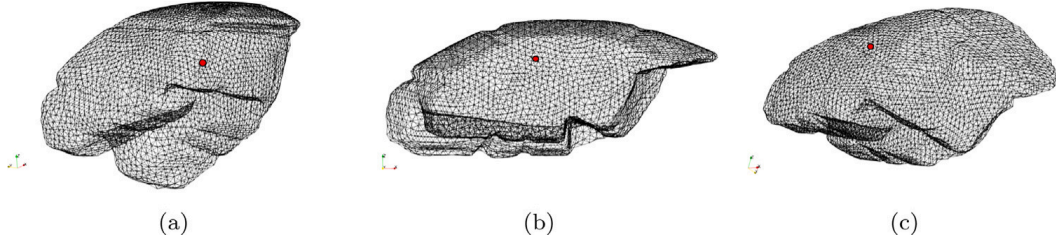
Fig. 3. Field point at the position of the driver's ear (red) from the front (a), the lateral (b) and rear view (c). (For interpretation of the references to color in this figure legend, the reader is referred to the web version of this article.)

$$e_k = \boldsymbol{v}_s^H \boldsymbol{A}_k \boldsymbol{v}_s = \boldsymbol{v}_s^H \sqrt{\boldsymbol{A}_k}^H \sqrt{\boldsymbol{A}_k} \boldsymbol{v}_s = \sum_{j=1}^{N_n} \alpha_{k_j}^* \alpha_{k_j} = \sum_{j=1}^{N_n} \mu_{k_j}, \tag{25}$$

$$e_t = \boldsymbol{v}_s^H \boldsymbol{A}_t \boldsymbol{v}_s = \boldsymbol{v}_s^H \sqrt{\boldsymbol{A}_t}^H \sqrt{\boldsymbol{A}_t} \boldsymbol{v}_s = \sum_{j=1}^{N_n} \alpha_{t_j}^* \alpha_{t_j} = \sum_{j=1}^{N_n} \mu_{t_j}, \tag{26}$$

with μ_{p_j}, μ_{k_j}, and μ_{t_j} identifying the potential, the kinetic, and the total energy density surface contributions, respectively. All surface contributions are real-valued and non-negative. Note that the formulation presented here is only for the discrete surface contributions. For visualization purposes, however, we will refer to the continuous surface contributions, as they are independent of the topology of the underlying boundary element mesh. For more details on this topic, the interested reader is referred to the article. [37]

An alternative solution for the sound energy density can be obtained with the FEM. However, as we are primarily interested in the solution at the boundary, we favor a formulation based on the BEM. Another reason to use the BEM is the fact that the particle velocity in the sound field can be determined analytically, see Eq. (10).

5. Numerical results

The numerical model to be investigated represents the cavity of a vehicle. which was provided by BMW. The density of air and the related speed of sound were assumed to be $\rho = 1.21 \, \text{kg/m}^3$ and $c = 343 \, \text{m/s}$. The numerical model of the cavity consisted of 8012 linear, discontinuous boundary elements resulting in 24 036 boundary element nodes. Following [58], we have chosen twenty boundary elements per wavelength. We are aware that this discretization leads to a very fine resolved mesh. However, in further analyses, e.g. fully coupled vibro-acoustic problems, a sufficiently fine mesh size is required. The cavity mesh is uniformly distributed leading to minimal element edge length of $0.05 \, \text{m}$, a maximal edge length of $0.104 \, \text{m}$, and an average edge length of $0.065 \, \text{m}$. In comparison, the car cabin exhibits the dimensions of length $3.032 \, \text{m}$, width $1.554 \, \text{m}$, and height $1.283 \, \text{m}$. Regarding the boundary admittance, we either imposed sound hard boundary conditions, $Y_0 = 0$, everywhere or the Robin boundary condition $\rho c Y_1 = f/f_{\text{ref}}$ with $f_{\text{ref}} = 2800 \, \text{Hz}$ according to the reverberation time measurements published by Marburg and Hardtke [59]. The numerical model was excited by vibrations at the footwell of the cabin, which were realized as Neumann boundary conditions with the real-valued, normal particle velocity $v_s = 0.001 \, \text{m/s}$. Moreover, we chose to evaluate the acoustic field quantities at the position of the driver's ear, as comfort requirements play a crucial role in the early vehicle design [60]. Fig. 3 shows the location of the field point, which represents the position of the driver's ear, from three different perspectives.

As certain vibroacoustic problems in vehicles, particularly booming noise, dominate at lower frequencies, the frequency range was considered from $20 \, \text{Hz}$ to $150 \, \text{Hz}$ [60,61]. A schematic overview of the numerical model and its excitation is depicted in Fig. 4.

In the initial phase, we performed harmonic analyses in order to determine the frequencies to be investigated in more depth. Therefore, we evaluated the sound pressure level, $\text{SPL} = 20 \log(p/p_{\text{ref}})$ with the reference sound pressure $p_{\text{ref}} = 2.0 \cdot 10^{-5}$ Pa, at the location of the driver's ear. The harmonic analyses were performed for Y_0 and Y_1. The resulting sound pressure levels for both cases are displayed in Fig. 5. For hard reflecting walls, Y_0, the sound pressure level at the driver's position is on average around $60 \, \text{dB}$. While the SPL is minimal at $71 \, \text{Hz}$ and $99 \, \text{Hz}$, resonance peaks occur at $78 \, \text{Hz}$, $109 \, \text{Hz}$, or $130 \, \text{Hz}$ resulting in sound pressure levels theoretically going to infinity. For Y_1, the sound pressure level at the location of the driver is around $60 \, \text{dB}$ below $110 \, \text{Hz}$. In the frequency range from $110 \, \text{Hz}$ to $150 \, \text{Hz}$, higher sound pressure levels can be observed around $75 \, \text{dB}$. Minima and resonance peaks do not occur due to the damping characteristics of the chosen boundary admittance parametrization. Fig. 5 indicates the following frequencies of interest for the upcoming contributions analysis. The choice of the relevant frequencies is based on the Y_0 configuration. The first frequency can be spotted at $f_1 = 71 \, \text{Hz}$, where the SPL is very low. The resonance peak suggests a second relevant frequency at $f_2 = 109 \, \text{Hz}$, whereas a third interesting frequency can be identified in the region of higher SPL values, for instance $f_3 = 120 \, \text{Hz}$. The chosen frequency snapshots are illustrated by the vertical lines in Fig. 5.

Prior to the contribution analysis, a modal analysis up to $f = 150 \, \text{Hz}$ is carried out in order to examine the mode shapes and the eigenfrequencies of the cabin with respect to the sound pressure, see Fig. 6. In the modal analysis, the boundary admittance is adopted to Y_0 on each element. The first mode shape occurring at $\tilde{f}_1 = 75 \, \text{Hz}$ shows the sound pressure in the first axial mode pattern (Fig. 6(a)). In the second mode shape at $\tilde{f}_2 = 109 \, \text{Hz}$ the sound pressure is strongly pronounced in the footwell of the driver (Fig. 6(b)), whereas the third mode shape at $\tilde{f}_3 = 130 \, \text{Hz}$ can be identified as the second axial mode pattern (Fig. 6(c)). Note that a

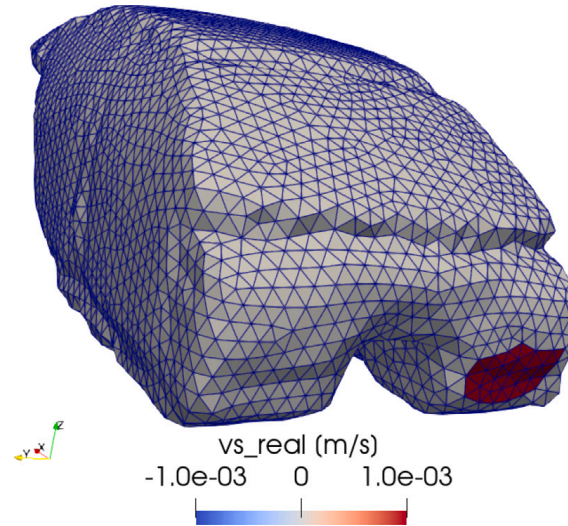vs_real (m/s)

-1.0e-03   0   1.0e-03

Fig. 4. Boundary mesh of the sedan cabin compartment excited by a real-valued, normal particle velocity on the left side of the footwell (red). (For interpretation of the references to color in this figure legend, the reader is referred to the web version of this article.)
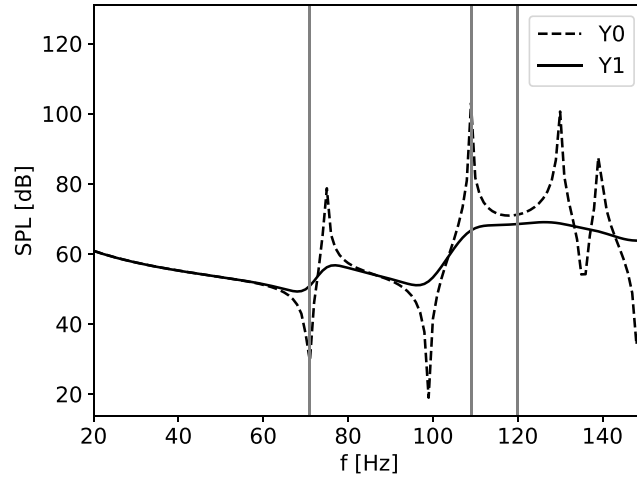

Fig. 5. Sound pressure level at the driver's ear evaluated for sound hard boundary conditions, $Y_0 = 0$ (dotted), and the boundary admittance $\rho c Y_1 = f / f_{\mathrm{ref}}$ with $f_{\mathrm{ref}} = 2800\,\mathrm{Hz}$ (solid). The snapshots at $71\,\mathrm{Hz}$, $109\,\mathrm{Hz}$ and $120\,\mathrm{Hz}$ are denoted by the vertical lines (gray).

p (Pa) @ lambda_1 = 75 Hz
-2.2e+00 -1 0 1 2.1e+00

p (Pa) @ lambda_2 = 109 Hz
-2.0e+00 0 1 2 3.6e+00

p (Pa) @ lambda_3 = 130 Hz
-2.1e+00 -1 0 1 2 3.2e+00

(a)   (b)   (c)
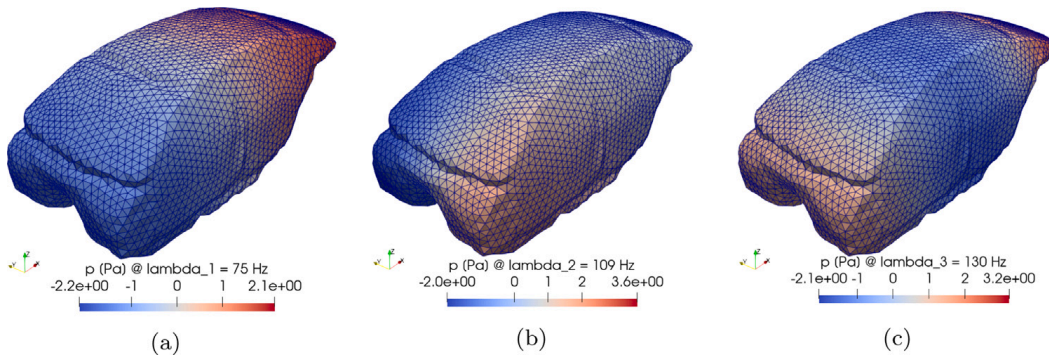
Fig. 6. Mode shapes of the cabin at the eigenfrequencies $\tilde{f}_1 = 75\,\mathrm{Hz}$ (a), $\tilde{f}_2 = 109\,\mathrm{Hz}$ (b), and $\tilde{f}_3 = 130\,\mathrm{Hz}$ (c) with respect to the sound pressure. The boundary admittance is adopted to Y_0 on each element.

further eigenfrequency occurs at $\tilde{f}_4 = 139\,\mathrm{Hz}$. However, as this eigenfrequency lies far enough away from the considered frequencies, we have omitted the presentation of its mode shape for the sake of clarity.

Fig. 7 shows the sound energy density levels evaluated at the driver's position for the potential, the kinetic, and the total energy density. The results obtained from a harmonic analysis with hard reflecting walls are presented in Fig. 7(a), whereas Fig. 7(b) shows
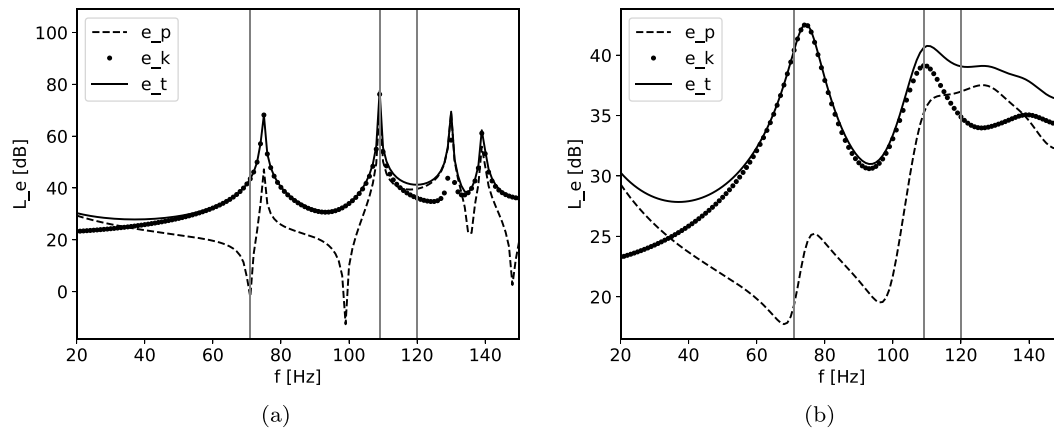
Fig. 7. Potential energy density (dashed), kinetic energy density (dotted), and total energy density (solid) evaluated at the location of the driver's ear for sound hard boundary conditions, Y_0 (a), and the boundary admittance Y_1 (b). The vertical lines denote the frequency snapshots at 71 Hz, 109 Hz, and 120 Hz.

the results regarding absorbing boundary admittances. The sound energy density level was computed according to $L_e = 10 \log(e/e_{\text{ref}})$ with the reference energy density $e_{\text{ref}} = 10^{-12}$ W/m³.

Regarding the scenario with hard reflecting walls (Fig. 7(a)), there is a clear correlation between the potential energy density levels and the sound pressure level in Fig. 5: The potential energy density is minimal at 71 Hz and 99 Hz and has resonance peaks at 78 Hz, 109 Hz, 130 Hz, and 139 Hz. Below 110 Hz, the potential energy level is on average 20 dB, while it amounts to 40 dB in the frequency range from 110 Hz to 150 Hz. The kinetic energy density level, however, is around 40 dB over the entire frequency range with peaks at 78 Hz, 109 Hz, and 130 Hz as well. The total energy density level is nearly identical to the kinetic energy density level in the frequency range from 20 Hz to 110 Hz. Above 110 Hz, the total energy density level is higher than the kinetic energy density level with peaks matching those with the potential energy density level, e.g., at 130 Hz and 140 Hz.

By applying absorbing boundary conditions (Fig. 7(b)), one can observe a potential energy density level around 20 dB for frequencies below 100 Hz. In the frequency range between 100 Hz and 150 Hz it reaches values around 37 dB. On average, the kinetic energy density level exhibits higher values than the potential energy density for frequencies up to 115 Hz. Above 115 Hz, the kinetic energy density level is approximately 33 dB. The total energy density level is nearly identical with the kinetic energy density level in the frequency range from 60 Hz to 110 Hz. Outside this range, the total energy density level is higher than both, the potential and the kinetic energy density level. As stated in Eq. (20), the total energy density is determined by the sum of the potential and kinetic energy density. Thus, it becomes natural that the total energy density level is always higher than the potential and kinetic energy density at the same position.

Returning to the aim posed at the beginning of this paper, the energy-based surface contributions are studied to evaluate acoustic cavities, especially in areas where the SPL is very low. For this purpose, contribution analyses have been conducted in three case studies based on the frequency snapshots resulting from the SPL (Fig. 5) and the sound energy density levels (Fig. 7) at the driver's position. In the initial case study, the frequency of interest was chosen from a frequency range with low SPL values, e.g., $f_1 = 71$ Hz. With the kinetic energy mainly contributing to the total energy, the particle velocity at the driver's position was inspected more closely at f_1. Second, the energy density-based surface contributions were analyzed at the resonance frequency, $f_2 = 109$ Hz. By the fact that both the potential and kinetic energy contribute equally to the total energy density level, the effect of the absorbing boundary conditions was further investigated at f_2. The third case study dealt with a frequency snapshot from a frequency range with intermediate SPL values between two mode shapes. Thus, the third relevant frequency was adopted to $f_3 = 120$ Hz. At this frequency, the potential energy-based surface contributions were additionally compared to the traditional, sound pressure-based surface contributions.

5.1. Surface contributions in a frequency range with low sound pressure

Fig. 8 shows the results for the potential (a), the kinetic (b), and the total energy density-based surface contributions (c) at $f_1 = 71$ Hz with respect to the driver's position. In this case, the contribution analysis was performed for hard reflecting walls, i.e., the boundary admittance being Y_0. The resulting surface contributions to the potential energy density are nearly zero everywhere, whereas surfaces contributing to the kinetic energy density are detected in the front footwell and in the rear of the vehicle. Regarding the surface contributions to the total energy density, sensitive regions are identified again in the front footwell and in the rear of the vehicle.

As already stated in Fig. 5, a frequency range with low sound pressure regarding the driver's position was detected at $f_1 = 71$ Hz. At the same frequency, the potential energy density at the driver is nearly zero, while the kinetic energy density is very high. Thus, surface contributions to the potential energy density are negligible at $f_1 = 71$ Hz. As a consequence, the total energy density surface contributions are essentially determined by the kinetic energy density surface contributions. However, it is interesting to note that the total energy density at the driver's ear is considerably high at $f_1 = 71$ Hz in spite of a very low SPL value.
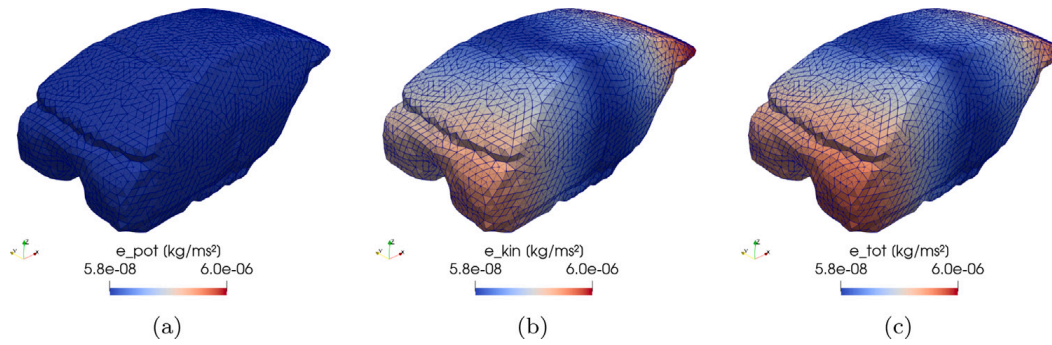
Fig. 8. Potential energy density (a), kinetic energy density (b), and total energy density (c) surface contributions at 71 Hz regarding the driver's position. The boundary admittance is adopted to Y_0 on each element.

The fact that the kinetic energy surface contributions are predominant at $f_1 = 71$ Hz motivates a closer inspection on the influence coefficients regarding the particle velocity at the driver's location, see Eq. (16). In Fig. 9, the resulting influence coefficients in the three spatial directions are compared with the kinetic energy surface contributions at $f_1 = 71$ Hz. The boundary admittance Y_0 is adopted on each element. The influence coefficients with respect to the particle velocity in x-direction are high in the front and in the rear of the vehicle, while they are very low around the B-pillars (Fig. 9(a)). As far as the influence coefficients in y- and z-direction are concerned, only a small region above the driver seat appears sensitive with respect to structural vibrations in this region. The influence coefficients in y- and z-direction of the remaining surfaces are nearly zero (Fig. 9(b), Fig. 9(c)). For the sake of clarity, the kinetic energy surface contributions are displayed again in Fig. 9. As already discussed, surfaces contributing to the kinetic energy density at the driver's ear were identified in the front footwell and in the rear of the vehicle, see Fig. 9(d). The results in this figure reveal that the kinetic energy surface contributions at this frequency and for an excitation in the lower left footwell are essentially driven by the influence coefficients regarding the particle velocity in x-direction. This finding is further substantiated by considering the axial mode pattern at the first eigenfrequency $\tilde{f}_1$, see Fig. 6(a). The influence coefficients with respect to the particle velocity in y- and z-direction play no role in the present load case.

5.2. Surface contributions at the resonance

The next part of this paper deals with the energy surface contributions at the resonance frequency $f_2 = 109$ Hz, see Figs. 5 and 7. The resulting potential, kinetic, and total energy density surface contributions are presented in Fig. 10. The upper row shows the results for hard reflecting walls, i.e., for Y_0, whereas the lower row presents the results with the absorbing boundary, i.e. for Y_1.

Regarding the potential energy surface contributions for hard reflecting walls, active regions only become apparent in the footwells of the front passenger seats, see Fig. 10(a). The same surfaces contribute in a similar way to the kinetic and to the total energy density at the driver's location (Figs. 10(b), 10(c)). In comparison with the second mode shape of the cavity (Fig. 6(b)), it becomes apparent that especially the left part of the footwell is activated at $f = 109$ Hz. By imposing absorbing boundary conditions, surfaces above the driver seat additionally contribute to the potential energy density, see Fig. 10(d). Kinetic and total energy surface contributions are observed in the footwell of the driver seat, see Figs. 10(e) and 10(f), respectively.

For the case Y_0, the most surprising aspect of this result is that almost the same surfaces, namely the footwells in the front seats, contribute to the potential and the kinetic energy density at the driver's position. Regarding absorbing boundary conditions, a high correlation is found between the kinetic energy and the total energy surface contributions at $f_2 = 109$ Hz, since surfaces contributing to the total energy density are essentially covered by the kinetic energy surface contributions. Curiously, the total energy surface contributions appear to be unaffected by the potential energy contributions, as surfaces contributing to the potential energy density, e.g., the right front footwell or the roof lining above the driver, are not recovered in the total energy contribution analysis.

Closer inspection at Fig. 7 reveals that the composition of the total energy density at the resonance $f_2 = 109$ Hz changes when absorbing boundary conditions are applied. For instance, in the undamped case, the potential energy and the kinetic energy contribute equally to the total energy. However, by imposing more realistic, absorbing boundary conditions, we observe that the potential energy density remains lower than the kinetic energy density. This shifts the energy composition in favor of the kinetic energy, which leads to the fact that the kinetic energy dominates in the total energy balance at $f_2 = 109$ Hz. Similar to what was already observed in Section 5.1, surfaces, which only contribute to the potential energy, are not necessarily contributing to the total energy.

5.3. Surface contributions in a frequency range with intermediate sound pressure

Fig. 11 shows the results obtained from the contribution analysis at $f_3 = 120$ Hz for sound hard boundary conditions. The potential (Fig. 11(a)), the kinetic (Fig. 11(b)), and the total energy density surface contributions (Fig. 11(c)) are compared with the magnitudes of the sound pressure related influence coefficients (Fig. 11(d)), which are evaluated according to Eq. (8). Surfaces contributing to the potential energy density are mainly apparent in the area of the driver's footwell. Minor potential energy contributions can
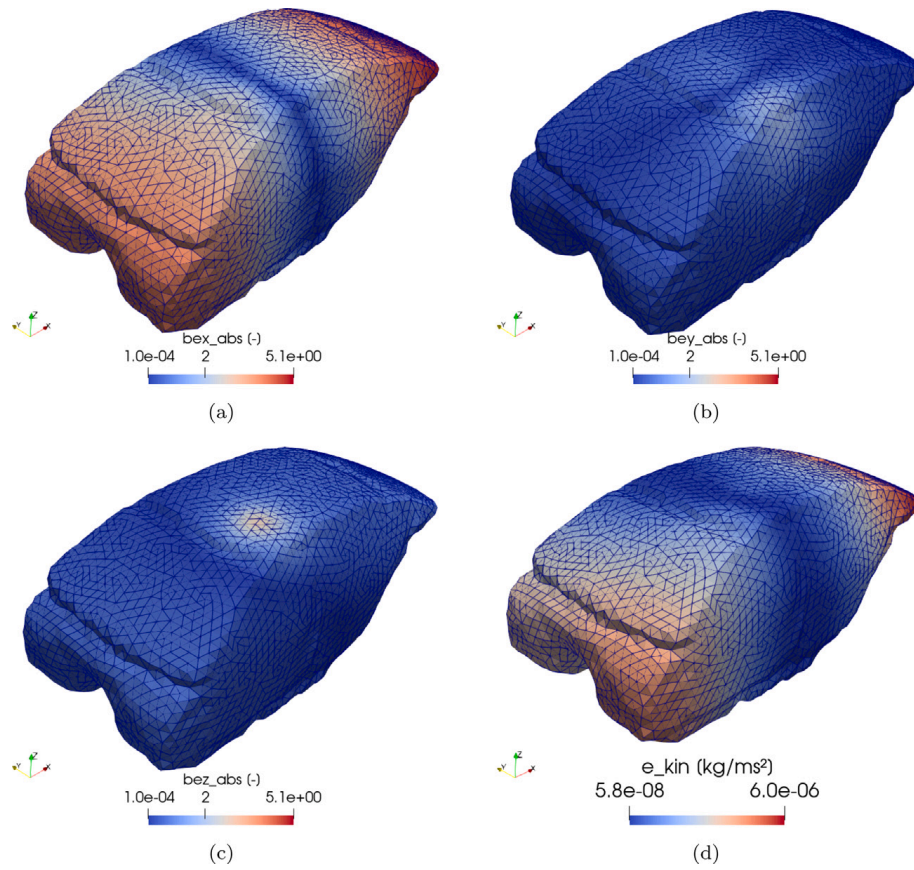
Fig. 9. Influence coefficients regarding the particle velocity in *x*-direction (a), *y*-direction (b), and *z*-direction (c) at 71 Hz with respect to the driver's position and the kinetic energy density surface contributions (d). The boundary admittance is adopted to Y_0 on each element.
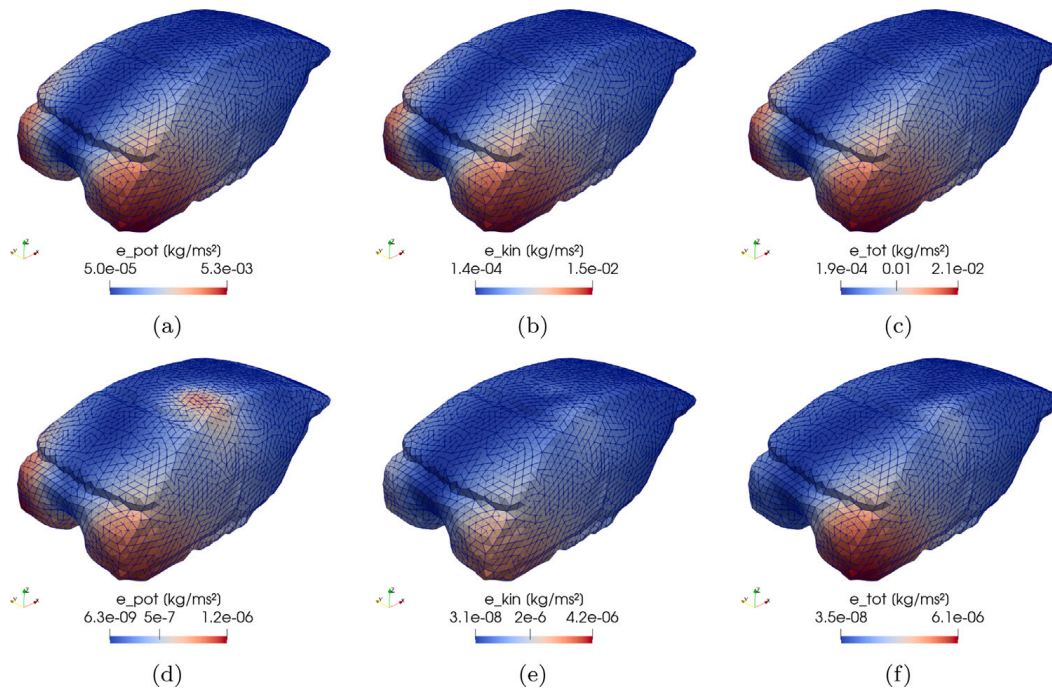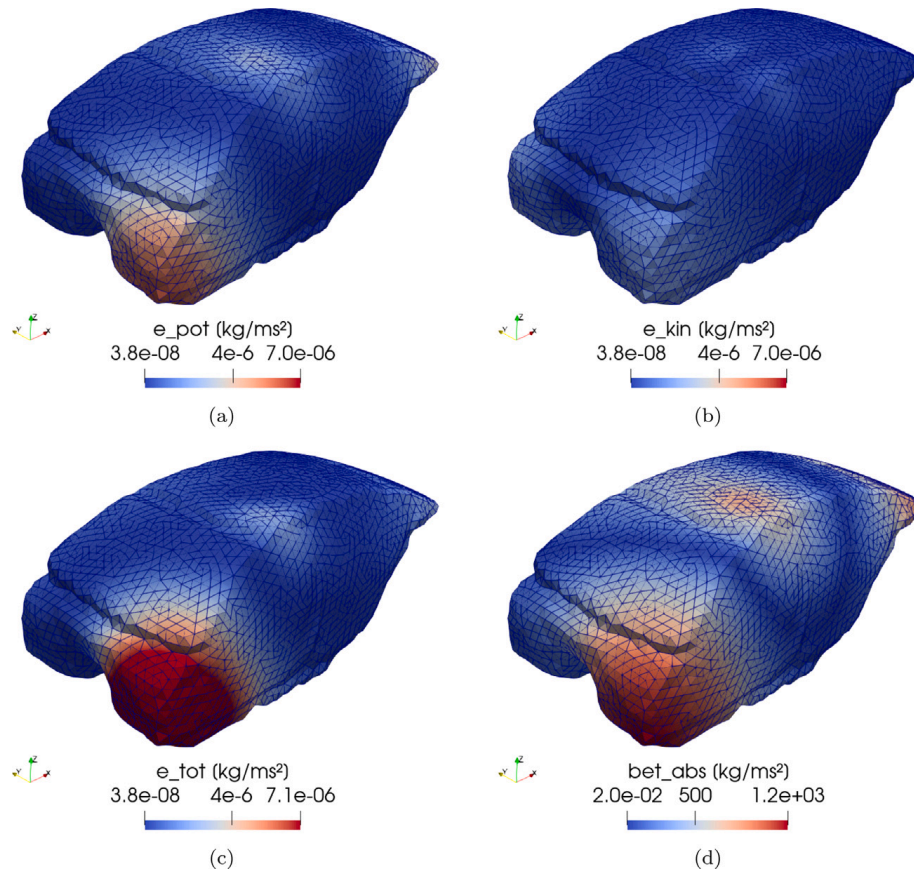

Fig. 10. Potential, kinetic, and total energy density surface contributions at 109 Hz with respect to the driver's location for sound hard boundary conditions, i.e., the case of Y_0 (a–c), and the boundary admittance, i.e., the case of Y_1 (d–f).

Fig. 11. Surface contributions based on the potential energy density (a), the kinetic energy density (b), and on the total energy density (c) and the influence coefficients regarding the sound pressure at the driver's position (d) at 120 Hz. Sound hard boundary conditions are imposed on each element.

be detected on the roof liner above the driver seat and on the rear part of the vehicle. The kinetic energy surface contributions, however, are nearly zero everywhere. As far as the total energy contributions are concerned, highly active regions are spotted again in the driver's footwell. Further marginal total energy contributions are identified above the driver's position and in the rear of the vehicle. The same active surfaces can be identified in the case of the sound pressure related influence coefficients. A comparison with the mode shapes at $\tilde{f}_2 = 109$ Hz (Fig. 6(b)) and $\tilde{f}_3 = 130$ Hz (Fig. 6(c)) reveals that active regions occur at the driver's footwell and at the rear of the cabin, respectively. As we have selected the third relevant frequency, $f_3 = 120$ Hz, in between these two eigenfrequencies, the active regions obtained with the contribution analysis concur very well with those in the second and third mode shape. The distribution of the surface contributions is further supported by the chosen excitation, which is imposed at the driver's footwell and acts in the axial x-direction, see Fig. 4. As discussed in Section 5.1, the contribution analysis revealed that the kinetic energy contributions dominate in frequency ranges with low sound pressure, e.g., at $f_1 = 71$ Hz. In contrast to this, we now observe that the potential energy surface contributions are predominant in a frequency range with intermediate sound pressure. The results obtained for the sound pressure related influence coefficients concur very well with the potential energy contributions. This becomes natural as the potential energy density is formulated by the square of the sound pressure, see Eq. (15).

In summary, our results suggest an important role for energy density-based surface contributions. Active surfaces were efficiently determined by the traditional, sound pressure related contribution analysis in a frequency range with high sound pressure, see the results in Section 5.3. At frequencies with low sound pressure, however, we observed that contributing surfaces cannot be recovered by purely considering the potential energy density or the associated sound pressure level, see Section 5.1. The reason for this is that the potential energy density and the associated SPL were extremely low in these frequency ranges, which leads to negligible surface contributions. Nevertheless, this weak spot was leveraged by analyzing the total energy density, particularly by the kinetic energy density. As presented in Fig. 8, only an energy-based contribution analysis was able to recover the sound radiating surfaces.

Remark that a traditional, sound pressure-based contribution analysis would yield panel contributions only for panels where the surface particle velocity is non-zero. Thus, panels which are not externally excited would be considered as insensitive. However, our results clearly demonstrate that all surfaces can contribute to the acoustic energy density at the field point, even if they are not externally excited. Moreover, cancellation effects are bypassed, as the energy-based surface contributions are non-negative by definition. These findings therefore confirm the usefulness of an energy density-based contribution analysis, particularly at frequencies with low sound pressure levels.

6. Conclusion

In this paper, the aim has been to develop a methodology which enables the evaluation of an acoustic cavity by observing sound energy densities. For this purpose, we have introduced a formulation for energy density-based surface contributions. To validate our method, we performed BEM simulations of a car cabin from BMW. The results of this study show that sensitive surfaces were effectively recovered by the energy-based contribution analysis. This was particularly the case at frequencies with low SPL values. In the present study, we focused on surface contributions with respect to a single field point at single frequencies. Thus, a natural progression of this work is an energy-based contribution analysis regarding multiple field points over several frequency bands. Future work will further concentrate on extensions with respect to multiple load cases and more realistic excitation models. As the total sound energy is sensitive to both, the sound pressure and the particle velocity, we think that our method could provide an alternative approach to evaluate acoustic fields in interior domains.

CRediT authorship contribution statement

Caglar Gurbuz: Conceptualization, Methodology, Software, Visualization, Investigation, Writing – original draft, Writing – review & editing. **Johannes D. Schmid:** Investigation, Data curation, Visualization. **Marinus Luegmair:** Resources, Data curation. **Steffen Marburg:** Conceptualization, Methodology, Software, Supervision.

Declaration of competing interest

The authors declare that they have no known competing financial interests or personal relationships that could have appeared to influence the work reported in this paper.

Acknowledgment

References

[1] S.-I. Ishiyama, M. Imai, S.-I. Maruyama, H. Ido, N. Sugiura, S. Suzuki, The Applications of Acoust/Boom—a Noise Level Predicting and Reducing Computer Code, SAE Technical Paper, 1988.

[2] S. Marburg, H.-J. Hardtke, R. Schmidt, D. Pawandenat, Application of the concept of acoustic influence coefficients for the optimization of a vehicle roof, Eng. Anal. Bound. Elem. 20 (1997) 305–310.

[3] S. Marburg, Efficient optimization of a noise transfer function by modification of a shell structure geometry-part i: Theory, Struct. Multidiscip. Optim. 24 (1) (2002) 51–59.

[4] R.A. Adey, S.M. Niku, J. Baynham, P. Burns, Predicting acoustic contributions and sensitivity. application to vehicle structures, WIT Trans. Built Environ. 11 (1995).

[5] J.P. Coyette, H. Wynendaele, C. M. K, A global acoustic sensitivity tool for improving structural design, in: Proceedings - SPIE the International Society for Optical Engineering, No. 1923, 1993, pp. 1389–1394.

[6] J. Dong, K.K. Choi, N.-H. Kim, Design optimization of structural–acoustic problems using fea–bea with adjoint variable method, ASME J. Mech. Des. 126 (2004) 527–533.

[7] L. Cremers, P. Guisset, L. Meulewaeter, M. Tournour, A Computer–Aided Engineering Method for Predicting the Acoustic Signature of Vibrating Structures Using Discrete Models, Great Britain Patent No. GB 2000–16259, 2000.

[8] C.A. Joachim, D.J. Nefske, J.A. Wolf, Application of a Structural-Acoustic Diagnostic Technique to Reduce Boom Noise in a Passenger Vehicle, SAE Technical Paper, 1981.

[9] Y. Huang, Z. Cui, Recent developments for frequency domain analysis in LS-DYNA®, in: 11th European LS-DYNA Conference, 2017.

[10] K. Shaposhnikov, M.J. Herring, Panel contribution analysis based on FEM, BEM and numerical green's function approaches, J. Theor. Comput. Acoust. 26 (3) (2018) 1850037.

[11] M. Mühlmeier, T. Kumbeim, N. Vogler, Identifikation und reduzierung der flächenbeteiligungen am niederfrequenten innenraumgeräusch, in: Berechnung Und Simulation Im Fahrzeugbau VDI Berichte, Vol. 1153, 1994, pp. 221–235.

[12] G. Koners, Panel Noise Contribution Analysis: An Experimental Method for Determining the Noise Contributions of Panels To an Interior Noise, SAE Technical Paper, 2003.

[13] E.G. Williams, Fourier Acoustics: Sound Radiation and Nearfield Acoustical Holography, Academic Press, 1999.

[14] N. Valdivia, E.G. Williams, Implicit methods of solution to integral formulations in boundary element method based nearfield acoustic holography, J. Acoust. Soc. Am. 116 (3) (2004) 1559–1572.

[15] T. DeLillo, V. Isakov, N. Valdivia, L. Wang, The detection of surface vibrations from interior acoustical pressure, Inverse Probl. 19 (2003) 507–524.

[16] N. Valdivia, E.G. Williams, Krylov subspace iterative methods for boundary element method based near-field acoustic holography, J. Acoust. Soc. Am. 117 (2) (2005) 711–724.

[17] G.H. Koopmann, L. Song, J.B. Fahnline, A method for computing acoustic fields based on the principle of wave superposition, J. Acoust. Soc. Am. 86 (6) (1989) 2433–2438.

[18] M. Ochmann, The complex equivalent source method for sound propagation over an impedance plane, J. Acoust. Soc. Am. 116 (6) (2004) 3304–3311.

[19] I.-Y. Jeon, J.-G. Ih, On the holographic reconstruction of vibroacoustic fields using equivalent sources and inverse boundary element method, J. Acoust. Soc. Am. 118 (6) (2005) 3473–3482.

[20] N.P. Valdivia, E.G. Williams, Study of the comparison of the methods of equivalent sources and boundary element methods for near-field acoustic holography, J. Acoust. Soc. Am. 120 (6) (2006) 3694–3705.

[21] C. Bi, X. Chen, J. Chen, R. Zhou, Nearfield acoustic holography based on the equivalent source method, Sci. China Ser. E Eng. Mater. Sci. 48 (3) (2005) 338–354.

[22] S.F. Wu, On reconstruction of acoustic pressure fields using the helmholtz equation least squares method, J. Acoust. Soc. Am. 107 (5) (2000) 2511–2522.

[23] S.F. Wu, The helmholtz equation least-squares method, in: The Helmholtz Equation Least Squares Method, Springer, 2015, pp. 27–62.

[24] Z. Wang, S.F. Wu, Helmholtz equation–least-squares method for reconstructing the acoustic pressure field, J. Acoust. Soc. Am. 102 (4) (1997) 2020–2032.

[25] M.B.S. Magalhaes, R.A. Tenenbaum, Sound sources reconstruction techniques: A review of their evolution and new trends, Acta Acust. United Acust. 90 (2) (2004) 199–220.

[26] E.G. Williams, P.C. Houston, S.T. Herdic, B.H. Raveendra, B. Gardner, Interior near-field acoustical holography in flight, J. Acoust. Soc. Am. 108 (4) (2000) 1451–1463.

[27] B.-K. Kim, J.-G. Ih, On the reconstruction of the vibro-acoustic field over the surface enclosing an interior space using the boundary element method, J. Acoust. Soc. Am. 100 (5) (1996) 3003–3016.

[28] M. Weber, T. Kletschkowski, D. Sachau, Noise source identification in a 2d cavity based on inverse finite element method, J. Low Freq. Noise Vib. Active Control 29 (2010) 147–159.

[29] T. Kletschkowski, M. Weber, D. Sachau, Identification of noise sources in an aircraft fuselage using an inverse method based on a finite element model, Acta Acust. United Acust. 97 (2011) 974–983.

[30] C.-X. Bi, D.-Y. Hu, Y.-B. Zhang, W.-Q. Jing, Identification of active sources inside cavities using the equivalent source method-based free-field recovery technique, J. Sound Vib. 346 (2015) 153–164.

[31] N.P. Valdivia, Advanced equivalent source methodologies for near-field acoustic holography, J. Sound Vib. 438 (2019) 66–82.

[32] X. Zhao, S.F. Wu, Reconstruction of vibro-acoustic fields using hybrid nearfield acoustic holography, J. Sound Vib. 282 (3–5) (2005) 1183–1199.

[33] S.F. Wu, L.K. Natarajan, Panel acoustic contribution analysis, J. Acoust. Soc. Am. 133 (2013) 799–809.

[34] E.G. Williams, Supersonic acoustic intensity, J. Acoust. Soc. Am. 97 (1) (1995) 121–127.

[35] M.B.S. Magalhaes, R.A. Tenenbaum, Supersonic acoustic intensity for arbitrary shaped sources, Acta Acust. United Acust. 92 (2006) 189–201.

[36] E. Fernandez-Grande, F. Jacobsen, Q. Leclere, Direct formulation of the supersonic acoustic intensity in space domain, J. Acoust. Soc. Am. 131 (1) (2012) 186–193.

[37] S. Marburg, E. Lösche, H. Peters, N. Kessissoglou, Surface contributions to radiated sound power, J. Acoust. Soc. Am. 133 (6) (2013) 3700–3705.

[38] C.A. Corrêa Junior, R.A. Tenenbaum, Useful intensity: A technique to identify radiating regions on arbitrarily shaped surfaces, J. Sound Vib. 332 (6) (2013) 1567–1584.

[39] E.G. Williams, Convolution formulations for non-negative intensity, J. Acoust. Soc. Am. 134 (2) (2013) 1055–1066.

[40] D. Liu, H. Peters, S. Marburg, N. Kessissoglou, Supersonic intensity and non-negative intensity for prediction of radiated sound, J. Acoust. Soc. Am. 139 (5) (2016) 2797–2806.

[41] D. Liu, H. Peters, S. Marburg, N. Kessissoglou, Surface contributions to scattered sound power using non-negative intensity, J. Acoust. Soc. Am. 140 (2) (2016) 1206–1217.

[42] D. Liu, Z. Havránek, S. Marburg, H. Peters, N. Kessissoglou, Non-negative intensity and back-calculated non-negative intensity for analysis of directional structure-borne sound, J. Acoust. Soc. Am. 142 (1) (2017) 117–123.

[43] D.R. Wilkes, H. Peters, P. Croaker, S. Marburg, A.J. Duncan, N. Kessissoglou, Non-negative intensity for coupled fluid–structure interaction problems using the fast multipole method, J. Acoust. Soc. Am. 141 (6) (2017) 4278–4288.

[44] D. Liu, S. Marburg, N. Kessissoglou, Nonnegative intensity for target strength identification in marine ecosystem research, J. Theor. Comput. Acoust. (2021) 2150023.

[45] M. Karimi, L. Maxit, V. Meyer, S. Marburg, R. Kirby, Non-negative intensity for planar structures under stochastic excitation, J. Sound Vib. 488 (2020) 115652.

[46] D. Liu, S. Marburg, C. Geweth, N. Kessissoglou, Non-negative intensity for structures with inhomogeneous damping, J. Theor. Comput. Acoust. 27 (01) (2019) 1850050.

[47] S.D. Sommerfeldt, P.J. Nashif, An adaptive filtered-x algorithm for energy-based active control, J. Acoust. Soc. Am. 96 (1) (1994) 300–306.

[48] N. Tanaka, K. Kobayashi, Cluster control of acoustic potential energy in a structural/acoustic cavity, J. Acoust. Soc. Am. 119 (5) (2006) 2758–2771.

[49] G.H. Koopmann, J.B. Fahnline, Designing Quiet Structures: A Sound Power Minimization Approach, Academic Press, 1997, pp. 201–226.

[50] B.S. Cazzolato, C.H. Hansen, Active control of sound transmission using structural error sensing, J. Acoust. Soc. Am. 104 (5) (1998) 2878–2889.

[51] B.S. Cazzolato, Sensing systems for active control of sound transmission into cavities, typedissertation, 1999.

[52] B.S. Cazzolato, C.H. Hansen, Errors arising from three-dimensional energy density sensing in one-dimensional sound fields, J. Sound Vib. 236 (3) (2000) 375–400.

[53] S. Marburg, B. Nolte, A Unified Approach to Finite and Boundary Element Discretization in Linear Time-Harmonic Acoustics, Springer, Wien, 2008, pp. 1–34.

[54] S. Marburg, Boundary element method for time–harmonic acoustic problems, in: M. Kaltenbacher (Ed.), Computational Acoustics, Springer, Cham, 2018, pp. 69–158.

[55] S. Marburg, Developments in structural-acoustic optimization for passive noise control, Arch. Comput. Methods Eng. 9 (4) (2002) 291–370.

[56] T. Wu, A. Seybert, A weighted residual formulation for the chief method in acoustics, J. Acoust. Soc. Am. 90 (3) (1991) 1608–1614.

[57] L.E. Kinsler, A.R. Frey, A.B. Coppens, J.V. Sanders, Fundamentals of Acoustics, John wiley & sons, 1999.

[58] S. Marburg, S. Schneider, Influence of element types on numeric error for acoustic boundary elements, J. Comput. Acoust. 11 (3) (2003) 363–386.

[59] S. Marburg, H.-J. Hardtke, A study on the acoustic boundary admittance. determination, results and consequences, Eng. Anal. Bound. Elem. 23 (9) (1999) 737–744.

[60] M. Luegmair, J.D. Schmid, Challenges in Vibroacoustic Vehicle Body Simulation Including Uncertainties, SAE Technical Paper 2020-01-1571, 2020.

[61] J.D. Schmid, M. Luegmair, K. Sepahvand, S. Marburg, Uncertainty Quantification in Vibroacoustic Analysis of a Vehicle Body using Generalized Polynomial Chaos Expansion, SAE Technical Paper 2020-01-1572, 2020.

A.2 Paper B

Efficient analysis of energy-based surface contributions for an entire acoustic cavity

Caglar Gurbuz, and Steffen Marburg

Efficient Analysis of Energy-Based Surface Contributions for an Entire Acoustic Cavity

Caglar Gurbuz[*] and Steffen Marburg[†]

Department of Engineering Physics and Computation
Technical University of Munich, Garching 85748, Germany
[*]caglar.guerbuez@tum.de
[†]steffen.marburg@tum.de

Sound radiation from vibrating structures is a crucial concern in the vehicle design process. One effective tool to recover vibration patterns on surfaces is the surface contribution analysis. Recent implementations, however, focus on surface contributions with respect to single evaluation points. For a contribution analysis regarding an entire volume, the tedious volume integration is required. This study aims to develop an efficient contribution analysis technique for the acoustic evaluation of an entire cavity. In order to circumvent the cumbersome volume integral, the acoustic quantities are evaluated at regularly distributed field points. For this purpose, the three-dimensional Helmholtz equation is solved by using the boundary element method. Moreover, the eigendecomposition of the accompanying coupling matrices is involved in the proposed method. In contrast to traditional techniques, the sound energy is deployed as the objective function, since the sound energy is not only sensitive to the sound pressure but also to the particle velocity. Another beneficial aspect is that the energy-based contributions are nonnegative. In this way, acoustic short circuits are avoided. The proposed method is validated for two numerical examples: the inward radiating sphere and the vehicle interior noise problem. Initial findings already reveal that entire volumes can be analyzed with the energy-based contribution analysis. By this means, our method designates an efficient method to evaluate contributing surfaces with regard to entire cavities. This research emphasizes the relevance of an energy-based contribution analysis, since they provide deep insights into the acoustic behavior of cavities.

Keywords: Boundary element method; surface contribution analysis; sound energy.

1. Introduction

In recent years, there has been an increasing interest in surface or panel contribution analysis, which is mainly driven by the automotive industry. A first study on contribution analysis can be traced back to Ishiyama *et al.* in 1988.[1] In that study, the authors reported on a technique based on the boundary element method (BEM) to evaluate the sound pressure at the driver's position. By this means, they computed the product of the particle velocity and a coefficient vector, which refers to the transfer function between a BEM node and the field point of interest. In recent literature, multiple terms were introduced in an attempt to define the coefficient vector. For instance, the coefficient vector is referred to influence coefficients,[2] global sensitivities regarding the particle velocity[3] or sensitivities computed with the adjoint variable method.[4] In 2000, a patent was recorded introducing the term acoustic transfer vector (ATV). Surface contribution analyses based on ATVs can be found in various commercial finite element method (FEM) software packages, e.g. in MSC,[5] LS-DYNA[6] or in COMSOL.[7] However, throughout this paper, the term influence coefficients as introduced by Marburg *et al.*[8,9] will refer to the coefficient vector.

Contribution analyses based on experimental measurements were primarily conducted in the field of vehicle interior noise problems. For instance, an experimental technique was introduced, in which the contribution of each chassis panel to the sound pressure at the driver's ear location was measured.[10] Another experimental method based on transfer path analyses was reported in the paper.[11] Moreover, Microflown proposed a technique, which focuses on panel contributions based on measurements of the particle velocity.[12]

Beyond that, vibrating surfaces can also be recovered by using the near-field acoustic holography (NAH).[13] This technique has been also applied in interior problems. For instance, vibrating surfaces were identified for an aircraft fuselage by using the NAH.[14] Another method to reconstruct vibrating patterns on structures is the inverse BEM. Regarding interior problems, the inverse BEM has been applied to recover vibrating patterns in vehicle cabins.[15] As an alternative to the inverse BEM, inverse FEM methods were studied for an industrial aircraft fuselage[16] and a spatial sound field.[17] Further techniques to reconstruct vibrating surfaces are the equivalent source method (ESM)[18,19] and the Helmholtz equation least-squares (HELS) method.[20–22] The HELS method was also integrated in a panel contribution analysis for interior as well as exterior acoustic problem.[23] The literature by 2004 in this field has been reviewed by Magalhaes and Tenenbaum.[24]

For exterior acoustic problems, Williams[25] noted that only the supersonic wave component radiates to the far field, as the subsonic wave components are evanescent in the near field regime. Based on that finding, he derived the supersonic intensity (SSI). He suggested to prefer the SSI to the sound intensity as an objective function in exterior acoustic applications. The idea of the SSI was expanded for structures with arbitrary shapes and derived for analyses in the wavenumber domain[25] and space domain.[26] As an alternative to the SSI, Marburg *et al.*[27] formulated the nonnegative intensity (NNI) for exterior acoustics problems. The NNIs are inherently positive by definition. By this means, acoustic short circuits caused by alternating signs are abridged. Similarly, the useful intensity has been introduced by Corrêa Junior and Tenenbaum.[28] While these authors used the acoustic

radiation modes (ARMs) for filtering purposes, Marburg *et al.* computed the square root of the acoustic impedance matrix based on the ARMs. Further developments of the NNI involve sound scattering problems,[29] far-field analyses,[30] coupled fluid–structure problems at large-scale,[31,32] stochastic excitation models[33] and structures with inhomogeneous damping properties.[34] For planar structures, the NNIs can be alternatively computed analytically by using the convolution formulas from the paper.[35] Lastly, a spatial radiation filter was developed to determine the correlation between SSI and the NNI.[36]

Regarding interior acoustic problems, Sommerfeldt and Nashif[37] emphasized that purely sound pressure-based methods show a poor performance in regions, where the sound pressure values are low. To alleviate this issue, these authors suggested to use sound energy densities as an objective function, as these quantities are sensitive to both, the sound pressure and the particle velocity. This concept has been widely adopted in the field of active control, where it has been applied for vibrating structures[38] and sound transmission problems in cavities.[39–41] In a recent study, a nonnegative surface contribution analysis using sound energy densities as an objective function was developed for interior acoustic problems.[42] In close analogy to Sommerfeldt and Nashif,[37] the authors have demonstrated that an energy density-based method was able to identify contributing surface regions, which appeared inactive when solely the sound pressure was analyzed. Their proposed framework is based on a BEM formulation and is, thus, a purely numerical technique.

Koopmann and Fahnline published a book to better understand the design mechanisms for silent structures.[43] For exterior acoustic problems, they suggested the radiated sound power as a global quantity for the objective function, see also Ref. 44. However, they have pointed out that the radiated sound power is inappropriate for interior acoustic problems. Since there is no widely adopted quantity in interior acoustics, the authors have suggested to use the sound energy as the objective function.[43]

It is the aim of this study to implement the concept of the sound energy into a surface contribution analysis scheme in order to identify vibration patterns on structures. The sound energy, which is composed by the potential energy and the kinetic energy, is determined by the volume integral over the sound energy density. In contrast to previous research, where the sound pressure or the sound energy density has only been evaluated at single positions, this study introduces global quantities to acoustically characterize entire cavities. A thorough discussion on that topic is provided in the recent review paper.[45]

In this work, we approximate the cumbersome volume integral by evaluating a grid with multiple regularly distributed field points. By this means, the energy density at the field points can be interpreted as functional values for the integration. Thus, a finer grid resolution yields a more accurate prediction of the sound energy in the cavity. Within this context, we investigate how many field points are required for a plausible approximation of the sound energy. In this way, we present a technique which allows to identify the energy flow in structures by considering acoustic quantities observed only at a limited number of field points. Moreover, the energy-based contribution analysis is accompanied with the eigenvalue problem of the coupling matrices. Part of the aim of this study is to analyze the related eigenvalues and check if they show a similar decaying behavior as those of the ARMs.[46,47]

This paper is organized as follows. Section 2 briefly surveys the BEM for three-dimensional Helmholtz equation in the frequency domain. Section 3 outlines the approximation of the energy-related volume integral. In Sec. 4, the formulation on energy-based surface contributions is presented. Section 5 shows the results for two numerical examples, a sphere and an industrial vehicle cabin. Our conclusions are drawn in Sec. 6.

2. Boundary Element Method

Acoustic problems with the harmonic time dependence $\mathrm{e}^{-\mathrm{i}\omega t}$ are governed by the Helmholtz equation

$$\Delta p(\vec{\boldsymbol{x}}) + k^2 p(\vec{\boldsymbol{x}}) = 0, \quad \boldsymbol{x} \in \Omega \subset \mathbb{R}^3, \tag{1}$$

where $p(\vec{\boldsymbol{x}})$ denotes the scalar, complex-valued sound pressure in the acoustic field Ω. The wavenumber $k = \omega/c$ is composed by the angular frequency ω and the speed of sound c. For interior acoustics, the most relevant boundary conditions (BCs) are the Neumann BC

$$v_f(\vec{\boldsymbol{x}}) = \frac{1}{\mathrm{i}\omega\rho} \frac{\partial p(\vec{\boldsymbol{x}})}{\partial n(\vec{\boldsymbol{x}})}, \quad \boldsymbol{x} \in \Gamma \subset \mathbb{R}^2 \tag{2}$$

to consider vibration patterns on a rigid boundary Γ and the Robin BC

$$v_f(\vec{\boldsymbol{x}}) - v_s(\vec{\boldsymbol{x}}) = Y(\vec{\boldsymbol{x}})p(\vec{\boldsymbol{x}}), \quad \boldsymbol{x} \in \Gamma \subset \mathbb{R}^2, \tag{3}$$

to model the boundary admittance.[48] The entities $v_f(\vec{\boldsymbol{x}})$ and $v_s(\vec{\boldsymbol{x}})$ denote the normal fluid particle velocity and the normal structural particle velocity, respectively. The boundary admittance is denoted by $Y(\vec{\boldsymbol{x}})$, whereas the ambient density of the fluid is represented by ρ. Note that, for $Y(\vec{\boldsymbol{x}}) = 0$, the Robin BC degenerates to a Neumann BC.

Following Ref. 49, the boundary integral equation for Helmholtz problems can be expressed by

$$c(\vec{\boldsymbol{y}})p(\vec{\boldsymbol{y}}) + \int_\Gamma \frac{\partial G(\vec{\boldsymbol{x}}, \vec{\boldsymbol{y}})}{\partial n(\vec{\boldsymbol{x}})} p(\vec{\boldsymbol{x}})\mathrm{d}\Gamma(\vec{\boldsymbol{x}}) = \mathrm{i}\omega\rho \int_\Gamma G(\vec{\boldsymbol{x}}, \vec{\boldsymbol{y}})v_f(\vec{\boldsymbol{x}})\mathrm{d}\Gamma(\vec{\boldsymbol{x}}), \tag{4}$$

where $G(\vec{\boldsymbol{x}}, \vec{\boldsymbol{y}}) = \mathrm{e}^{\mathrm{i}kr}/(4\pi r)$ with the distance $r = r(\vec{\boldsymbol{x}}, \vec{\boldsymbol{y}})$ denotes Green's function and $c(\vec{\boldsymbol{y}})$ a geometric quantity determined by the contour on the boundary Γ at $\vec{\boldsymbol{y}}$. For instance, $c(\vec{\boldsymbol{y}}) = 0.5$ on smooth boundary elements.[49] Substituting Eq. (3) in Eq. (4) and discretizing with the collocation BEM yield the linear system of equations as

$$(\boldsymbol{H} - \boldsymbol{GY})\boldsymbol{p} = \boldsymbol{Gv}_s, \tag{5}$$

where $\boldsymbol{G}$ and $\boldsymbol{H}$ denote the global acoustic system matrices. These system matrices are neither Hermitian nor positive definite. For constant discontinuous interpolation functions, the boundary admittance matrix $\boldsymbol{Y}$ contains only entries on the diagonal. For higher-order polynomials, $\boldsymbol{Y}$ contains additional off-diagonal elements but is still a sparse matrix.[49]

3. Approximation of the Energy-Related Volume Integral

To obtain the sound pressure $p_i(\vec{y}_i)$ at N field points $\vec{y}_i$ inside the acoustic field, Eq. (4) is evaluated in the domain Ω

$$p_i(\vec{y}_i) = \mathrm{i}\omega\rho \int_\Gamma G(\vec{x}, \vec{y}_i) v_s(\vec{x}) \mathrm{d}\Gamma(\vec{x})$$

$$- \int_\Gamma \left[\frac{\partial G(\vec{x}, \vec{y}_i)}{\partial n(\vec{x})} - \mathrm{i}\omega\rho G(\vec{x}, \vec{y}_i) Y(\vec{x}) \right] p(\vec{x}) \mathrm{d}\Gamma(\vec{x}), \quad \vec{y}_i \in \Omega \tag{6}$$

or in discretized form[8,9]

$$p_i(\vec{y}_i) = \boldsymbol{g}_i^T(\vec{y}_i) \boldsymbol{v}_s - [\boldsymbol{h}_i^T(\vec{y}_i) - \boldsymbol{g}_i^T(\vec{y}_i) \boldsymbol{Y}] \boldsymbol{p}, \tag{7}$$

with the column matrices

$$\boldsymbol{g}_i(\vec{y}_i) = \mathrm{i}\omega\rho \int_\Gamma G(\vec{x}, \vec{y}_i) \boldsymbol{\varphi}(\vec{x}) \mathrm{d}\Gamma(\vec{x}), \tag{8}$$

$$\boldsymbol{h}_i(\vec{y}_i) = \int_\Gamma \frac{\partial G(\vec{x}, \vec{y}_i)}{\partial n(\vec{x})} \boldsymbol{\varphi}(\vec{x}) \mathrm{d}\Gamma(\vec{x}). \tag{9}$$

These column matrices denote the boundary integral operators to compute the sound pressure in Ω with the interpolation functions $\boldsymbol{\varphi}(\vec{x})$ representing the approximations for the sound pressure and the normal particle velocity. By substituting the sound pressure data with $\boldsymbol{p} = (\boldsymbol{H} - \boldsymbol{GY})^{-1} \boldsymbol{G} \boldsymbol{v}_s$, we obtain

$$p_i(\vec{y}_i) = \{ \boldsymbol{g}_i^T(\vec{y}_i) - [\boldsymbol{h}_i^T(\vec{y}_i) - \boldsymbol{g}_i^T(\vec{y}_i) \boldsymbol{Y}] (\boldsymbol{H} - \boldsymbol{GY})^{-1} \boldsymbol{G} \} \boldsymbol{v}_s$$

$$= \boldsymbol{b}_i^T(\vec{y}_i) \boldsymbol{v}_s, \quad \vec{y}_i \in \Omega \tag{10}$$

where the column matrices $\boldsymbol{b}_i(\vec{y}_i)$ represent the influence coefficients with respect to the sound pressure at N field points.

The particle velocity inside the acoustic field is computed in a similar way. We apply therefore the relation in Eq. (2) to Eq. (6) in order to obtain the particle velocity at N field points[50]

$$\vec{v}_i(\vec{y}_i) = \int_\Gamma \vec{\nabla}_{\vec{y}_i} G(\vec{x}, \vec{y}_i) v_s(\vec{x}) \mathrm{d}\Gamma(\vec{x})$$

$$- \left[\int_\Gamma \vec{\nabla}_{\vec{y}_i} \frac{1}{\mathrm{i}\omega\rho} \frac{\partial G(\vec{x}, \vec{y}_i)}{\partial n(\vec{x})} - \vec{\nabla}_{\vec{y}_i} G(\vec{x}, \vec{y}_i) Y(\vec{x}) \right] p(\vec{x}) \mathrm{d}\Gamma(\vec{x}), \quad \vec{y}_i \in \Omega, \tag{11}$$

or in matrix-form

$$\vec{v}_i(\vec{y}_i) = \{ \tilde{\boldsymbol{g}}_i^T(\vec{y}_i) - [\tilde{\boldsymbol{h}}_i^T(\vec{y}_i) - \tilde{\boldsymbol{g}}_i^T(\vec{y}_i) \boldsymbol{Y}] (\boldsymbol{H} - \boldsymbol{GY})^{-1} \boldsymbol{G} \} \boldsymbol{v}_s$$

$$= \tilde{\boldsymbol{b}}_i^T(\vec{y}_i) \boldsymbol{v}_s, \quad \vec{y}_i \in \Omega, \tag{12}$$

C. Gurbuz & S. Marburg

with the column matrices

$$\tilde{\boldsymbol{g}}_i(\vec{\boldsymbol{y}}_i) = \int_\Gamma \vec{\nabla}_{\vec{\boldsymbol{y}}_i} G(\vec{\boldsymbol{x}}, \vec{\boldsymbol{y}}_i) \boldsymbol{\varphi}(\vec{\boldsymbol{x}}) \mathrm{d}\Gamma(\vec{\boldsymbol{x}}), \tag{13}$$

$$\tilde{\boldsymbol{h}}_i(\vec{\boldsymbol{y}}_i) = \int_\Gamma \vec{\nabla}_{\vec{\boldsymbol{y}}_i} \frac{1}{\mathrm{i}\omega\rho} \frac{\partial G(\vec{\boldsymbol{x}}, \vec{\boldsymbol{y}}_i)}{\partial n(\vec{\boldsymbol{x}})} \boldsymbol{\varphi}(\vec{\boldsymbol{x}}) \mathrm{d}\Gamma(\vec{\boldsymbol{x}}) \tag{14}$$

denoting the boundary integral operator to compute the particle velocity in Ω. Analogously, the column matrices $\tilde{\boldsymbol{b}}_i(\vec{\boldsymbol{y}}_i)$ represent the influence coefficient vector with respect to the particle velocity at N field points. Note that $\boldsymbol{v}_i$ is expressed in bold letters, as it contains data in three spatial dimensions $\{x, y, z\}$. The same holds for the entities $\tilde{\boldsymbol{g}}_i, \tilde{\boldsymbol{h}}_i$ and $\tilde{\boldsymbol{b}}_i$. The term influence coefficient vector is generally understood as the sensitivity regarding the surface particle velocity. Note that in Eq. (10), $\boldsymbol{b}_i$ denotes the sensitivities of the sound pressure to the surface particle velocity, while $\tilde{\boldsymbol{b}}_i$ in Eq. (12) expresses the sensitivities of the particle velocity at N field point with respect to the surface particle velocity.

4. Energy-Based Surface Contributions

Energy in sound waves is transported in two forms: potential and kinetic energy. The potential energy is generated by the compression of the fluid particles, whereas the kinetic energy is produced when the fluid particles are moving. The potential energy E_p can be expressed in terms of the sound pressure, while the kinetic energy E_k term is based on the fluid particle velocity:

$$E_p = \frac{1}{2\rho c^2} \int_\Omega p(\vec{\boldsymbol{x}}) p^*(\vec{\boldsymbol{x}}) \mathrm{d}\Omega, \tag{15}$$

$$E_k = \frac{\rho}{4} \int_\Omega \vec{\boldsymbol{v}}_f(\vec{\boldsymbol{x}}) \cdot \vec{\boldsymbol{v}}_f^*(\vec{\boldsymbol{x}}) \mathrm{d}\Omega. \tag{16}$$

Note that the operator $()^*$ denotes the complex conjugate form of the related quantity. On this basis, the total sound energy is obtained by the sum of the potential energy and the kinetic energy[43,51]

$$E_t = E_p + E_k = \frac{1}{2\rho c^2} \int_\Omega p(\vec{\boldsymbol{x}}) p^*(\vec{\boldsymbol{x}}) \mathrm{d}\Omega + \frac{\rho}{4} \int_\Omega \vec{\boldsymbol{v}}_f(\vec{\boldsymbol{x}}) \cdot \vec{\boldsymbol{v}}_f^*(\vec{\boldsymbol{x}}) \mathrm{d}\Omega. \tag{17}$$

As explained in Sec. 1, this study aims a contribution analysis to evaluate the total sound energy in a cavity, see Eq. (17). To circumvent the cumbersome integration over the entire volume, the energy density is investigated at multiple field points. Therefore, a field point grid is required inside the cavity. For a considerable amount of field points, the average energy density is qualitatively equivalent to the sound energy. The energy density represents the energy concentrated on a zero reference volume. It is, thus, defined as energy per unit

volume [kg/ms^2] and can be evaluated at discrete locations in the acoustic domain.[37,38,41] As such, the potential energy density e_p, the kinetic energy density e_k and the total energy density e_t are expressed by

$$e_{p_i}(\vec{\boldsymbol{y}}_i) = \frac{1}{2\rho c^2} p_i^*(\vec{\boldsymbol{y}}_i) p_i(\vec{\boldsymbol{y}}_i), \tag{18}$$

$$e_{k_i}(\vec{\boldsymbol{y}}_i) = \frac{\rho}{4} \vec{\boldsymbol{v}}_i^*(\vec{\boldsymbol{y}}_i) \vec{\boldsymbol{v}}_i(\vec{\boldsymbol{y}}_i), \tag{19}$$

$$e_{t_i}(\vec{\boldsymbol{y}}_i) = e_{p_i}(\vec{\boldsymbol{y}}_i) + e_{k_i}(\vec{\boldsymbol{y}}_i), \tag{20}$$

where the index $i = 1, 2, \ldots, N$ refers to the identity of the field point. The field point values of the sound pressure p and the particle velocity $\vec{\boldsymbol{v}}$ are obtained according to Eqs. (10) and (12).

The integration of the energy density over the acoustic domain can be approximately obtained by the sum of the energy density at multiple field points regularly distributed within the cavity

$$\int_\Omega e \, \mathrm{d}\Omega \approx \sum_{i=1}^{N} e_i \cdot V_i = V_f \sum_{i=1}^{N} e_i, \tag{21}$$

with N and V_i denoting the total number of field points and the volume cell associated with the field point i. For regularly spaced field points, the volume cells are equal, i.e. $V_i = V_f$. The volume cell V_f can be then used to approximate the total volume $V \approx V_f \cdot N$. In this way, the averaged sound energy E can be expressed by

$$E \approx V_f \sum_{i=1}^{N} e_i. \tag{22}$$

In a next step, the potential energy can be expressed in a quadratic form by substituting Eqs. (10) and (18) into Eq. (22)

$$E_p = \frac{V_f}{2\rho c^2} \sum_{i=1}^{N} (\boldsymbol{b}_i^T \boldsymbol{v}_s)^* (\boldsymbol{b}_i^T \boldsymbol{v}_s) = \frac{V_f}{2\rho c^2} \boldsymbol{v}_s^H \left(\sum_{i=1}^{N} \boldsymbol{b}_i^* \boldsymbol{b}_i^T \right) \boldsymbol{v}_s$$

$$= \boldsymbol{v}_s^H \left(\sum_{i=1}^{N} \boldsymbol{A}_{p_i} \right) \boldsymbol{v}_s = \boldsymbol{v}_s^H \boldsymbol{A}_p \boldsymbol{v}_s, \tag{23}$$

where $()^H$ denotes the complex conjugate transpose operation. The quadratic form is established by the matrix $\boldsymbol{A}_p$, which denotes the coupling matrix regarding the potential energy densities at the field points. The matrix $\boldsymbol{A}_p$ is of rank N with N again denoting the total number of field points. Note that the indication of $\vec{\boldsymbol{y}}$-dependence is omitted here. The quadratic expression for the kinetic energy is obtained analogously by rearranging Eq. (22)

with Eqs. (19) and (12)

$$
E_k = V_f \frac{\rho}{4} \sum_{i=1}^{N} (\tilde{\boldsymbol{b}}_i^T \boldsymbol{v}_s)^* (\tilde{\boldsymbol{b}}_i^T \boldsymbol{v}_s) = V_f \frac{\rho}{4} \boldsymbol{v}_s^H \left(\sum_{i=1}^{N} \tilde{\boldsymbol{b}}_i^* \tilde{\boldsymbol{b}}_i^T \right) \boldsymbol{v}_s
$$

$$
= \boldsymbol{v}_s^H \left(\sum_{i=1}^{N} \boldsymbol{A}_{k_i} \right) \boldsymbol{v}_s = \boldsymbol{v}_s^H \boldsymbol{A}_k \boldsymbol{v}_s, \tag{24}
$$

with $\boldsymbol{A}_k$ denoting the coupling matrix regarding the kinetic energy densities at the field points. The rank of the matrix $\boldsymbol{A}_k$ is $3N$, since $\boldsymbol{A}_k$ contains information in the three spatial dimensions. The sum of the potential energy equation (23) and the kinetic energy equation (24) then yields the total energy

$$
E_t = E_p + E_k = \frac{V_f}{2\rho c^2} \sum_{i=1}^{N} (\boldsymbol{b}_i^T \boldsymbol{v}_s)^* (\boldsymbol{b}_i^T \boldsymbol{v}_s) + V_f \frac{\rho}{4} \sum_{i=1}^{N} (\tilde{\boldsymbol{b}}_i^T \boldsymbol{v}_s)^* (\tilde{\boldsymbol{b}}_i^T \boldsymbol{v}_s)
$$

$$
= \boldsymbol{v}_s^H \boldsymbol{A}_p \boldsymbol{v}_s + \boldsymbol{v}_s^H \boldsymbol{A}_k \boldsymbol{v}_s = \boldsymbol{v}_s^H \boldsymbol{A}_t \boldsymbol{v}_s \tag{25}
$$

with $\boldsymbol{A}_t$ denoting the coupling matrix with respect to the total energy densities at the field points. As the matrix $\boldsymbol{A}_t$ is composed by the sum of $\boldsymbol{A}_p$ and $\boldsymbol{A}_k$, the rank of $\boldsymbol{A}_t$ equals to $4N$. Note that the coupling matrices $\boldsymbol{A}_p$, $\boldsymbol{A}_k$ and $\boldsymbol{A}_t$ are all Hermitian and complex-valued. The resulting eigenvalues are thus real-valued and positive.

To assess the energy-based surface contributions, the square root of the coupling matrix $\boldsymbol{A}$ is required

$$
E = \boldsymbol{v}_s^H \boldsymbol{A} \boldsymbol{v}_s = \boldsymbol{v}_s^H \sqrt{\boldsymbol{A}}^H \sqrt{\boldsymbol{A}} \boldsymbol{v}_s = \sum_{j=1}^{N_n} \alpha_j^* \alpha_j = \sum_{j=1}^{N_n} \mu_j, \tag{26}
$$

with α_j denoting a discrete entity on the interpolation node j and μ_j the energy-based surface contribution from the node j. Note that the equation above holds for the surface contributions regarding the potential, the kinetic and the total energy. To compute the square root of matrix $\boldsymbol{A}$, the following eigenvalue problem has to be solved:

$$
\sqrt{\boldsymbol{A}} = \boldsymbol{\Psi}^H \sqrt{\boldsymbol{\Lambda}} \boldsymbol{\Psi}, \tag{27}
$$

where $\sqrt{\boldsymbol{\Lambda}}$ and $\boldsymbol{\Psi}$ denote the diagonal matrix containing the square root of the eigenvalues λ_i and the related eigenvectors, respectively. For the sake of conciseness, the detailed derivation of the matrix square root $\sqrt{\boldsymbol{A}}$ is omitted here. For more details, the interested reader is referred to Ref. 42. In the final step, the energy-based surface contributions can be formulated by incorporating Eq. (27) in Eqs. (23)–(25)

$$
E_p = \boldsymbol{v}_s^H \boldsymbol{A}_p \boldsymbol{v}_s = \boldsymbol{v}_s^H \sqrt{\boldsymbol{A}_p}^H \sqrt{\boldsymbol{A}_p} \boldsymbol{v}_s = \sum_{j=1}^{N_n} \alpha_{p_j}^* \alpha_{p_j} = \sum_{j=1}^{N_n} \mu_{p_j}, \tag{28}
$$

$$E_k = \boldsymbol{v}_s^H \boldsymbol{A}_k \boldsymbol{v}_s = \boldsymbol{v}_s^H \sqrt{\boldsymbol{A}_k}^H \sqrt{\boldsymbol{A}_k} \boldsymbol{v}_s = \sum_{j=1}^{N_n} \alpha_{k_j}^* \alpha_{k_j} = \sum_{j=1}^{N_n} \mu_{k_j}, \tag{29}$$

$$E_t = \boldsymbol{v}_s^H \boldsymbol{A}_t \boldsymbol{v}_s = \boldsymbol{v}_s^H \sqrt{\boldsymbol{A}_t}^H \sqrt{\boldsymbol{A}_t} \boldsymbol{v}_s = \sum_{j=1}^{N_n} \alpha_{t_j}^* \alpha_{t_j} = \sum_{j=1}^{N_n} \mu_{t_j}, \tag{30}$$

where μ_{p_j}, μ_{k_j} and μ_{t_j} denote the potential, the kinetic and the total energy surface contributions, respectively. Note that all energy surface contributions are real-valued and non-negative. It should be further noted that the formulation above considers only a discrete representation of the surface contributions. However, for visualization purposes, a continuous version of the surface contributions is deployed, as they are independent from the topology of the boundary element mesh. The continuous surface contributions η can be obtained by solving the linear system of equations $\boldsymbol{\eta} = \boldsymbol{\Theta}\boldsymbol{\mu}$, where $\boldsymbol{\Theta}$ denotes the boundary mass matrix. For more details on that topic, the interested reader is referred to the paper.[27]

5. Numerical Results

In this work, two numerical models are to be investigated: At first, the academic example of a sphere is analyzed. The second example focuses on an industrial application, a vehicle interior noise problem. In both examples, the acoustic medium is air with a density of $\rho = 1.21 \, \text{kg/m}^3$ and speed of sound of $c = 343 \, \text{m/s}$. In the final part of this study, the eigenvalue decay of the coupling matrices is examined.

5.1. *Sound radiation of a sphere*

The numerical model of the sphere is of radius $1 \, \text{m}$ and consists of 384 boundary elements with piecewise constant interpolation functions. Regarding the BCs, we impose sound hard BCs, $Y = 0$, on each element. A monopole excitation is imposed on the sphere. The related normal particle velocity is real-valued and amounts to $v_s = 1.0 \, \text{m/s}$. The frequency of interest is chosen to be $f = 100 \, \text{Hz}$. Figure 1 shows the numerical model of the sphere.

First, we consider a dense grid of field points in order to find an accurate approximation of the sound energy. Therefore, 504 field points are regularly distributed inside the sphere, see Fig. 2. Note that locating the field points close to the boundary may cause numerical issues. Thus, we suggest a minimum length of two elements between the boundary and the field points in order to avoid any undesirable events.

The resulting energy-based surface contributions at $100 \, \text{Hz}$ are shown in Fig. 3. The potential energy surface contributions are high on every boundary element, see Fig. 3(a). In contrast to this, we observe nearly no surface contributions with respect to the kinetic energy (Fig. 3(b)). The total energy surface contributions, in turn, exhibit high values on each element (Fig. 3(c)). In this case, the total energy contributions appear slightly higher than those related to potential energy. This study already indicates that the potential energy contributions are predominant in the present load case. The kinetic energy contributions
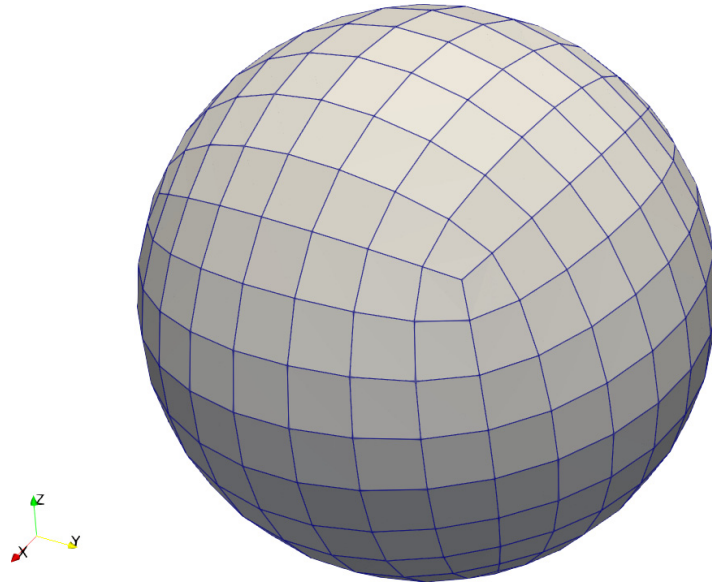
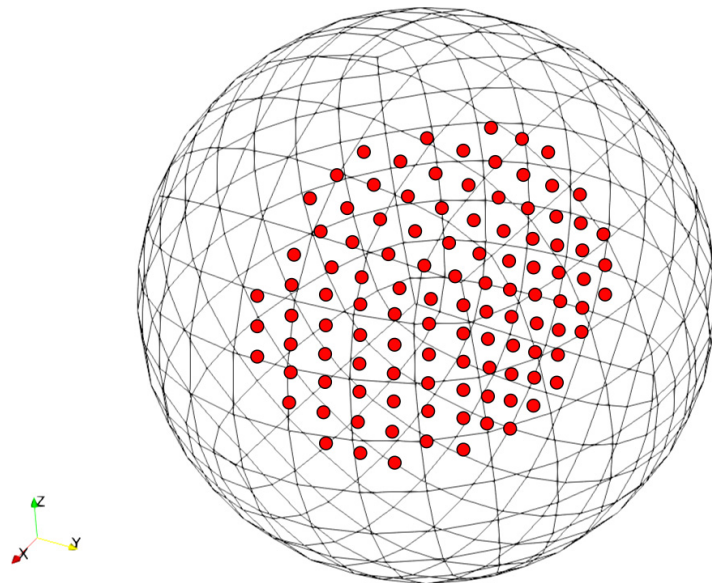Fig. 1. Mesh of the unit sphere with 384 constant, discontinuous boundary elements.

Fig. 2. Grid with 504 regularly distributed field points. The field points are distributed in a cuboid form. For the sake of clarity, not all field points are shown.

are negligible here. Thus, surfaces contributing to the total energy can be retrieved by solely analyzing the potential energy contributions.

In the next phase, the contribution analysis is performed regarding a single field point, which is located in the vicinity of the center. Subsequently, the number of field points is increased in order to analyze the convergence behavior of the energy surface contributions. For this purpose, two relatively coarse field point grids are investigated. The first coarse

(a) Potential   (b) Kinetic   (c) Total
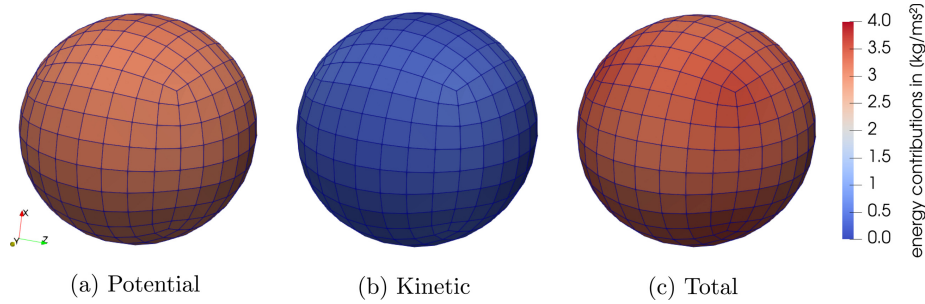
Fig. 3. Surface contributions regarding the potential (a), kinetic (b) and total (c) energy at 100 Hz. The contributions are evaluated for the dense grid with 504 field points.

(a)   (b)   (c)
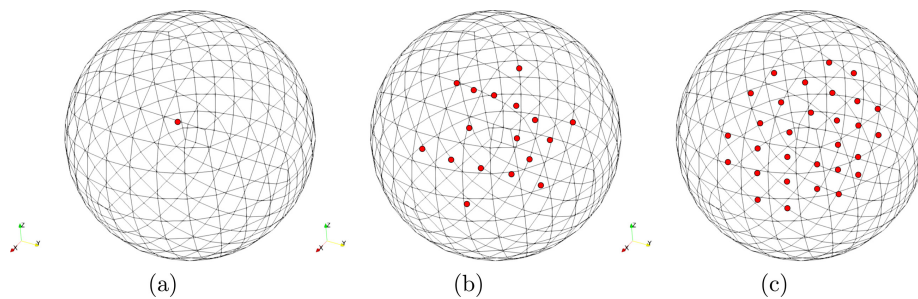
Fig. 4. (Color online) Three configurations for the field point grids (red). The first configuration contains one field point (a). The second and the third grids consist of 19 (b) and 117 (c) regularly distributed field points.

grid contains 19 field points, whereas 117 field points are regularly distributed in the second grid. The single field point and the coarse field point grids are depicted in Fig. 4.

To study the convergence behavior of the energy-based contributions regarding the entire cavity, the surface contributions are initially evaluated with respect to a single field point located at $[-0.1, -0.1, -0.1]$. The resulting energy-based surface contributions at 100 Hz are shown in Fig. 5(a). The potential energy contributions show a pronounced dipole pattern with active surfaces on one hemisphere (Fig. 5(I)(a)). At the same time, the kinetic energy contributions are nearly zero everywhere on the sphere (Fig. 5(I)(b)). The total energy contributions, in turn, exhibit a similar pattern as the energy contributions regarding the potential energy, see Fig. 5(I)(c). In this case, the values of the surface contributions are slightly smaller. For the present load case, the single field point analysis shows that the kinetic energy contributions are negligible. In this case, the surface contributions to the potential energy density are predominant, particularly, at the hemisphere, which is close to the field point. The same surfaces can be identified in the total energy contribution analysis, although they are less pronounced there.

In a next step, the surface contributions are studied on a coarse grid with 19 field points. The resulting energy-based contributions are depicted in Fig. 5(II). The field points are distributed according to Fig. 4(b). The surfaces contributing to the potential energy densities can be identified on all elements, see Fig. 5(II)(a). The kinetic energy contributions,
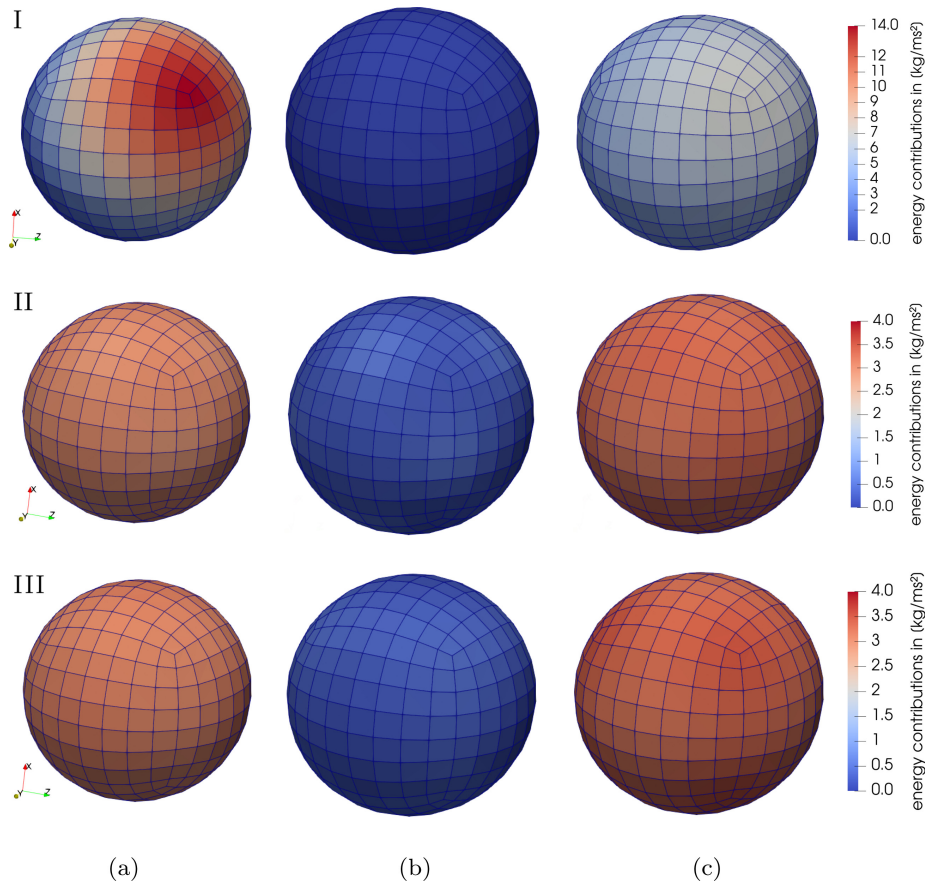
Fig. 5. Surface contributions regarding the potential (a), kinetic (b) and total (c) energy. The surface contributions for a single field point are visualized in row (I). The contributions for 19 and 117 field points are shown in rows (II) and (III), respectively. The contribution analysis is performed at 100 Hz.

on the other hand, are nearly zero everywhere on the sphere (Fig. 5(II)(b)). The total energy contributions are also identified for all elements. In comparison to the potential contributions, the total energy contributions achieve slightly lower values (Fig. 5(II)(c)). The multi-point analysis with 19 field points reveals contributing surfaces to the total energy at every boundary element. The same elements can be also retrieved by solely investigating the contributions to the potential energy, as the kinetic energy contributions are negligible in this case.

Moreover, the energy-based contributions are analyzed for a the second coarse representation of the volume. In this case, the coarse grid contains 117 field points, as shown in Fig. 4(c). The results of the energy-based surface contributions for 117 field points at 100 Hz are visualized in Fig. 5(III). The results of the contribution analysis with 117 field points are very similar to those with 19 field points. We again observe that all surfaces contribute to the potential as well as to the total energy, see Figs. 5(III)(a) and 5(III)(c). No surface contributions are detected regarding the kinetic energy (Fig. 5(III)(b)).

The results for this academic example already indicate that the concept of energy contributions can be transferred from a single point to a multi-point analysis. The most interesting

aspect of these results is that the composition of the potential and the kinetic energy contributions to the total energy contributions nearly remains constant. This is observed in the contribution analyses for the dense grid, the single field point and the coarse grids with 19 and 117 field points. Another interesting aspect is the allocation of the energy contributions. For instance, in the single point analysis, we observe active regions at one pole of the sphere (Fig. 5(I)(a)). With increasing number of field points, it becomes apparent that the energy contributions are shifted to all elements, see Figs. 5(II)(a) and 5(III)(a). Moreover, the comparison of the multi-point results with the dense field grid reveals that the same surfaces contribute to the total sound energy. This result is significant, as it shows that the surface contributions regarding the total sound energy already converge for a grid with 19 or 117 field points. By this means, the volume integral can be approximated by using a relatively coarse grid within the cavity. As such, the multi-point analysis provides important insights for the interior acoustic problem in an efficient way. Note that the surface contributions are always nonnegative. The reason for this is the quadratic expression in the formulation of the energy contributions, see Eqs. (28)–(30).

5.2. *Vehicle interior noise problem*

Turning now to an industrial application, a vehicle interior noise problem is examined in the second numerical example. The numerical model of the vehicle cabin has been provided by BMW.[42] It is discretized by 4420 boundary elements with constant pressure approximation. The cabin is meshed with an average edge length of $0.09\,\mathrm{m}$. In relation to this, the vehicle cabin is $3.032\,\mathrm{m}$ long, $1.554\,\mathrm{m}$ wide and $1.283\,\mathrm{m}$ high. This leads to approximately 10 elements per wavelength at $400\,\mathrm{Hz}$, which is in accordance with Ref. 52. The boundary admittance is modeled according to the reverberation time measurements reported in Ref. 53. Therefore, the Robin BC $\rho c Y = f/f_{\mathrm{ref}}$ with $f_{\mathrm{ref}} = 2800\,\mathrm{Hz}$ is imposed on each element. Moreover, a Neumann BC with the real-valued, normal particle velocity $v_s = 0.001\,\mathrm{m/s}$ is imposed at the left footwell to excite the numerical model. Following Ref. 42, the frequency of interest is chosen to be $71\,\mathrm{Hz}$. The mesh of the vehicle cabin is shown in Fig. 6.

Prior to the analysis with coarse field point grids, the energy contributions are initially analyzed for a grid with densely arranged field points. Therefore, 441 regularly distributed field points are employed. In this way, we obtain a sufficiently accurate approximation for the energy surface contributions with regard to the cabin volume. The distribution of the field points is depicted in Fig. 7.

The results of the contribution analysis are depicted in Fig. 8. The potential energy surface contributions are nearly zero on each boundary element, see Fig. 8(a). Only trace amounts can be observed in the front footwell of the driver's seat. The kinetic surface contributions, on the other hand, expose high values in the driver's footwell as well as in the rear of the vehicle cabin (Fig. 8(b)). Similarly, the total energy surface contributions are also high in the driver's footwell and in the rear (Fig. 8(c)). In comparison with the kinetic energy, the total energy contributions appear slightly higher. In contrast to the sphere problem in Sec. 5.1, the total energy contributions are here mainly determined by
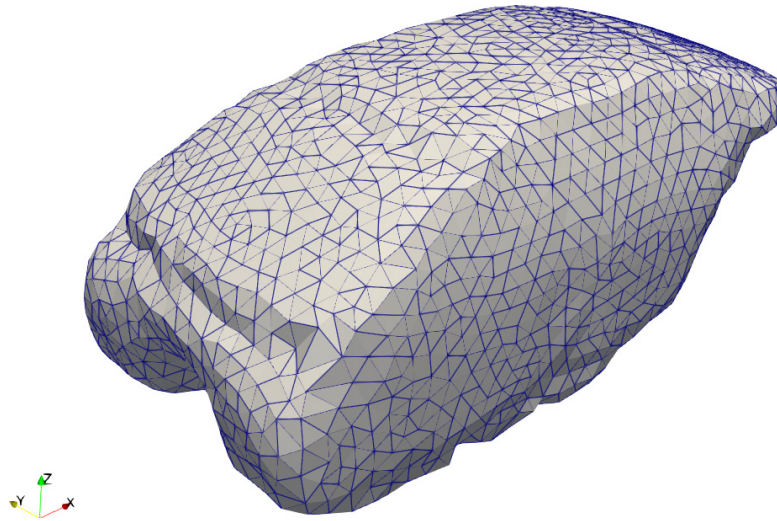
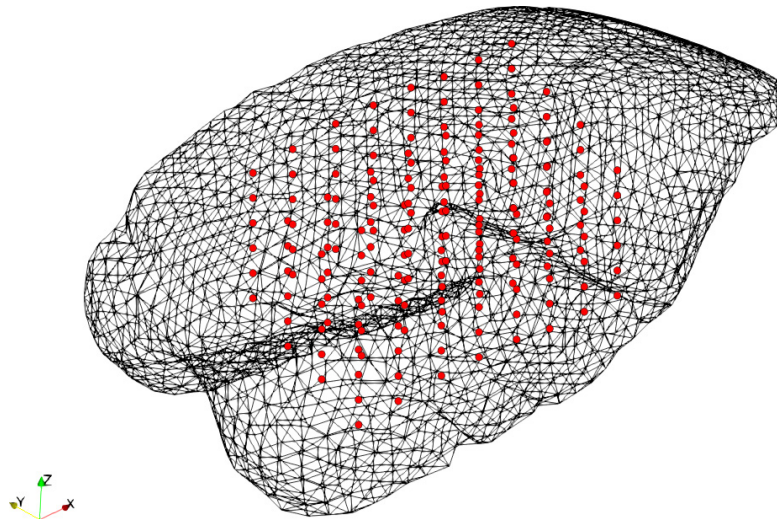Fig. 6. Vehicle cabin mesh with 4420 constant, discontinuous boundary elements.

Fig. 7. Grid with 441 regularly distributed field points inside the vehicle cabin. For the sake of clarity, not all field points are visualized.

the kinetic energy. This finding emphasizes the importance of the sound energy as the objective function, since contributing surfaces would remain undetected in a pure sound pressure-based contribution analysis.

In the next studies, the number of field points is incrementally increased from one single point over 36 to 140 field points. Regarding the single field point analysis, the location of the driver's ear is adopted as the field point position. The surface contributions to this particular position are crucial due to increasing comfort requirements on the design of the vehicle.[54–56] In the multi-point analyses, 36 and 140 field points are regularly distributed inside the cabin. As mentioned in Sec. 5.1, we use again a minimum length of two elements between the boundary and the field points in order to avoid any undesirable events. The position

(a) Potential   (b) Kinetic   (c) Total
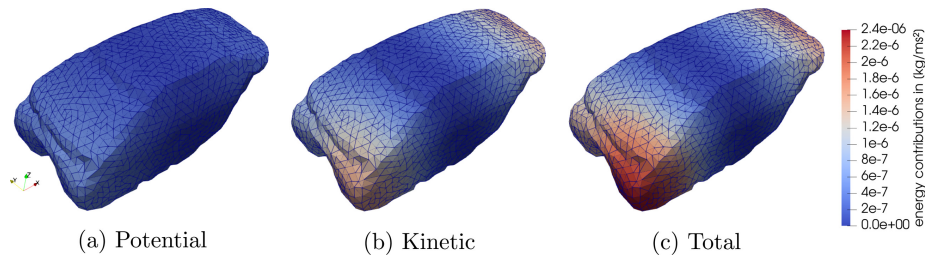
Fig. 8. Surface contributions regarding the potential (a), kinetic (b) and total (c) energy density at 441 field points. The analyses are performed at 71 Hz.
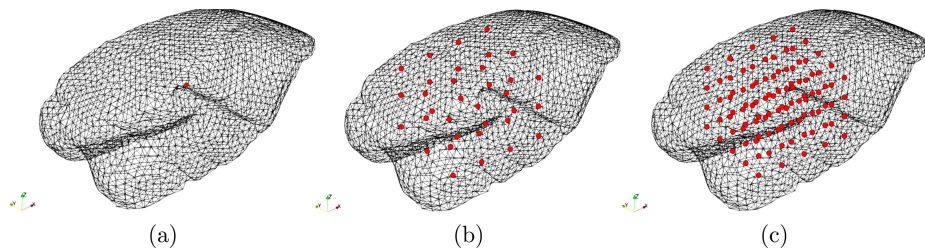

(a)   (b)   (c)

Fig. 9. (Color online) Three configurations for the field point grids (red). The first configuration contains only a single field point at the driver's ear (a). The second and third grids contain 36 (b) and 140 (c) regularly distributed field points. For the sake of clarity, not all 140 field points are visualized.

of the field points regarding the single point and the multi-point analyses is schematically depicted in Fig. 9.

The resulting energy surface contributions regarding a single field point are depicted in Fig. 10(I). Even though the results for a single point are extensively discussed in Ref. 42, a brief outline of them is provided here for the sake of completeness. The potential energy contributions are nearly zero on the entire boundary of the cabin, see Fig. 10(I)(a). On the other hand, the surface contributions to the kinetic energy density expose high values in the front footwells and in the rear of the cabin (Fig. 10(I)(b)). Similar results can be observed for the total energy contributions. Contributing surfaces are also identified in the front and rear part of the cabin. In comparison with the kinetic energy contributions, the total energy contributions in the front part are even slightly higher (Fig. 10(I)(c)).

The energy contributions in the multi-point analysis with 36 evaluation points are depicted in Fig. 10(II). Regarding the potential energy, no significant surface contributions can be identified. Only trace amounts of surface contributions are detected in the region of the front footwell, see Fig. 10(II)(a). The contribution analysis with respect to the kinetic energy reveals contributing surfaces in the front footwell. Further contributing surfaces are detected in the rear of the cabin (Fig. 10(II)(b)). The total energy contribution analysis also indicates active regions in the front footwell and in the rear of the cabin. Compared to the kinetic energy contributions, the total energy contributions are significantly higher in the front part of the cabin, see Fig. 10(II)(c). The results of the multi-point analysis with 36 field points show that the surfaces contributing to total energy density are mainly driven by the kinetic energy contributions. Although trace amounts of surface contributions can
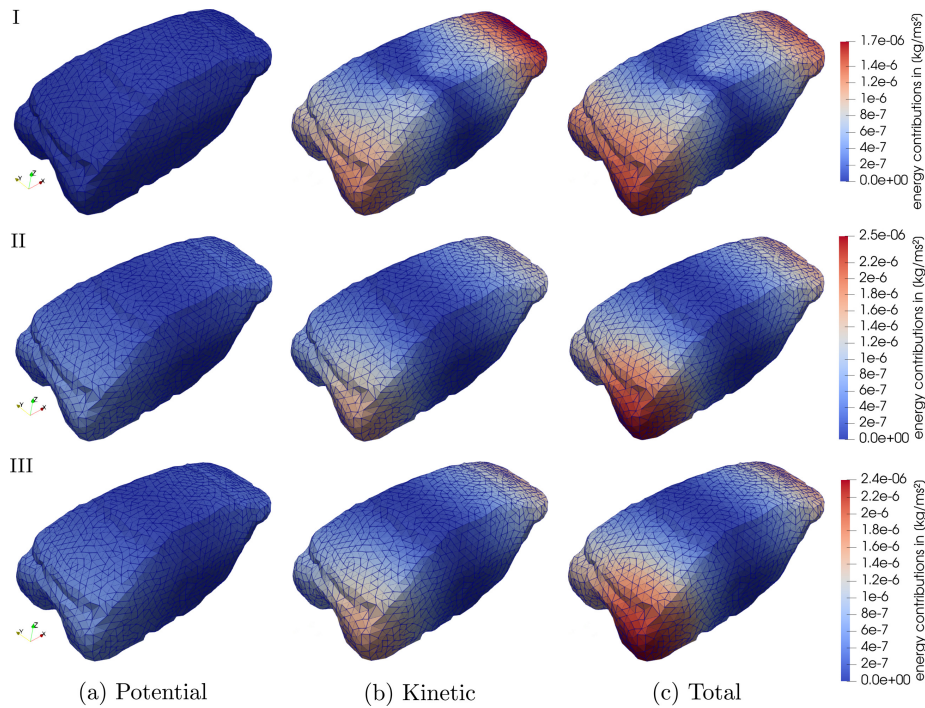
Fig. 10. Surface contributions in a vehicle cabin regarding the potential (a), kinetic (b) and total (c) energy. The surface contributions to a single field point are depicted in the first row (I). The contributions for 36 and 140 field points are shown in rows (II) and (III), respectively. The analyses are performed at 71 Hz.

be observed in the potential energy contribution analysis, the total energy contributions appear to be unaffected by the potential energy contributions. The kinetic energy surface contributions are also predominant here.

In the final part of this example, the energy contribution analysis is performed for 140 evaluation points. The resulting surface contributions are presented in Fig. 10(III). It becomes apparent that the results with 140 field points are very similar to those with 36 field points. Regarding the potential energy contributions, nearly no active regions are identified (Fig. 10(III)(a)), while the kinetic energy contributions expose contributing surfaces in the front footwell and in the cabin rear (Fig. 10(III)(b)). The same contributing surfaces are again identified in the total energy contribution analysis, see Fig. 10(III)(c).

Taken together, the analyses with a single and multiple evaluation points already provide important insights into the acoustic behavior of a vehicle cabin. Regarding the potential energy, significant surfaces are neither identified in the single point nor in the multi-point analyses. This is concurrent with the resulting potential energy contributions for the dense grid with 441 field points. The more interesting finding is related to the kinetic energy contributions. For instance, the single point analysis clearly indicates active surfaces in the front and in the rear part of the cabin. The multi-point analyses with 36 and 140 field points reveal the same regions, although they are less pronounced there. By comparing the results from the coarse grids with the dense grid, the same contributing surfaces are identified. Very similar results are also observed in the total energy contribution analysis. By increasing the

number of field points from 1 to 140, one can observe that the contributing surfaces to the sound energies are consistent with the surfaces in the analysis with 441 field points. These findings demonstrate that a grid with 36 field points already suffices to recover the essential surface contributions for the vehicle cabin. Thus, our results suggest that entire cabins can be efficiently analyzed by evaluating the surface contributions only a for relatively coarse grid. By this means, the cumbersome evaluation of the volume integral can be effectively circumvented.

5.3. *Study of eigenvalue decay of the coupling matrices*

Lastly, the eigenvalues of the coupling matrices $\boldsymbol{A}_p$, $\boldsymbol{A}_k$ and $\boldsymbol{A}_t$ are analyzed. The eigenvalues are computed for the radiating sphere and the vehicle cabin. The results for the first 20 eigenvalues are shown in Fig. 11. For the sphere, the resulting eigenvalues of the coupling matrices with respect to the potential (blue), the kinetic (orange) and the total (green) energy are shown in Fig. 11(a). The eigenvalue decomposition is performed at 100 Hz for the grid with 117 regularly distributed field points, as shown in Fig. 4(c). The eigenvalue decomposition for the radiating sphere reveals four marginal eigenvalues with respect to the potential energy. Regarding the kinetic energy, three significant eigenvalues can be observed. The eigenvalue analysis for the total energy exposes four distinct eigenvalues. The first three eigenvalues are very close to each other, whereas the fourth eigenvalue is relatively small. Since the coupling matrix regarding the total energy is composed by the sum of the matrices regarding the potential and kinetic energy, the eigenvalues related to the total energy cover the eigenvalues related to the potential and the kinetic energy. In particular, the first three eigenvalues are related to the kinetic energy, while the fourth eigenvalue can be assigned to the potential energy. Surprisingly, the eigenvalues with respect
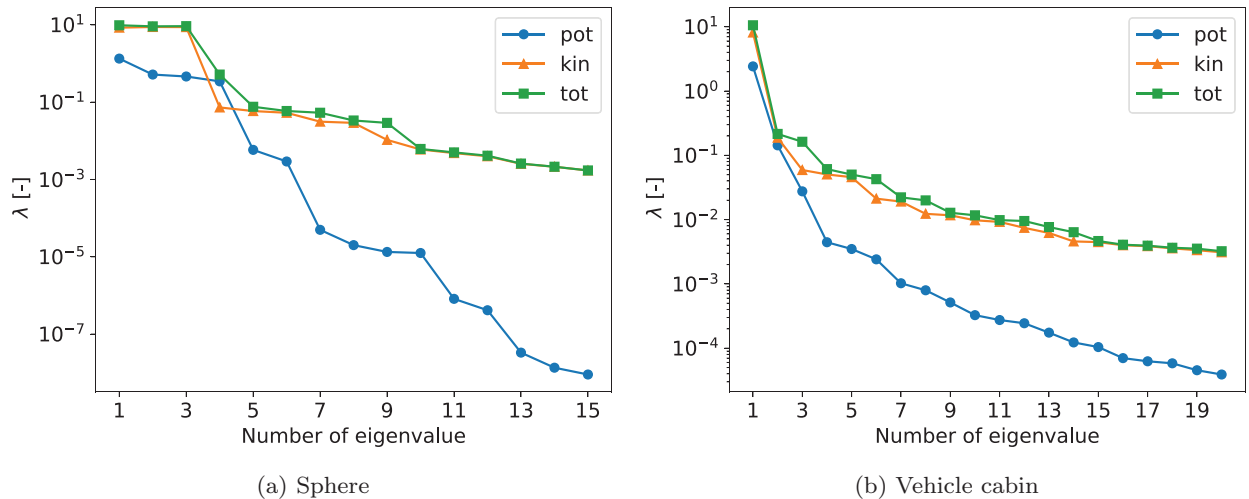

(a) Sphere   (b) Vehicle cabin

Fig. 11. (Color online) Eigenvalues of the coupling matrices regarding the potential (blue), the kinetic (orange) and the total energy density (green). The eigenvalues are shown for the sphere at 100 Hz (left) and for the vehicle cabin at 71 Hz (right). The number of field points amounts to 117 in the sphere. In the vehicle cabin, 140 field points are considered.

to the kinetic energy are higher than those related to the potential energy, although we observed in Sec. 5.1 that the energy contributions to the potential are predominant here. This discrepancy could be attributed to the presented load case, in which the sphere is uniformly excited. The eigenvalue analysis for the radiating sphere reveals only a small number of distinct eigenvalues. This emphasizes the concept of energy contribution analyses for a coarse grid in order to efficiently analyze the surface contributions for the acoustic behavior in entire cavities. It should be noted that the eigenvalues show a decaying behavior. This is in accordance with the eigenvalues analysis performed in the paper.[46,47]

Regarding the vehicle interior noise problem, the eigenvalues of the coupling matrices regarding the potential (blue), the kinetic (orange) and the total (green) energy are depicted in Fig. 11(b). The eigenvalue decomposition is performed at 71 Hz for the multi-point analysis with 140 field points. The first four distinct eigenvalues with respect to the potential energy are spotted at 1.5, 0.15, 0.02 and 0.003. Thereafter, the ratios between two adjacent eigenvalues are very small. Regarding the kinetic energy, three distinct eigenvalues are observed around 7, 0.17 and 0.05. Two further significant eigenvalues can be noticed at 0.04. The first eigenvalue corresponding to the total energy amounts approximately to 10. The next distinct eigenvalues are around 0.2 and 0.19. After that, the eigenvalues with respect to the kinetic and total energy decrease with a lower rate. Note that the eigenvalues regarding the kinetic energy are here higher than those related to the potential energy. The eigenvalue analysis shows that only few distinct eigenvalues can be observed, although the ranks of the coupling matrices $\boldsymbol{A}_p$, $\boldsymbol{A}_k$ and $\boldsymbol{A}_t$ are a multiple of the number of field points N. This again demonstrates that the information contained in the field point grid is redundant. Thus, the eigenvalue analysis supports the idea that a relatively coarse field point grid is sufficient in order to obtain an efficient approximation for the energy contributions with respect to an entire cavity. Once again, it should be pointed out that the eigenvalues are also decaying in the vehicle cabin example.

6. Conclusion

This study is set out to assess the surface contributions in an entire acoustic cavity. In order to bypass the cumbersome evaluation of the volume integral, the energy-based surface contributions were determined on a grid of regularly distributed field points. The proposed method relies on the acoustic energy density as an objective function. Our method is accompanied by the eigendecomposition of the coupling matrices, which are computed by the BEM. To validate the proposed method, the academic example of the sphere and an industrial vehicle interior noise problem were investigated. Moreover, the eigenvalues associated with the coupling matrix regarding the sound energy were investigated. The studies of the sphere example have shown that the total energy contributions in cavities can be well approximated by solely using coarse grids of regularly distributed field points. Regarding the vehicle cabin, it also seems that multiple regularly distributed field points can be used to approximate the total energy contributions. This paves the way for the efficient evaluation of the contribution of vibrating surfaces within acoustic cavities. By this means, the energy surface contribution

analysis provides deep insights on the acoustic behavior inside the cavity. Thus, the evidence from this study highlights the importance of an energy-based contribution analysis. Moreover, the vehicle interior noise problem demonstrated that the concept of energy-based surface contributions can be transferred to industrial applications. Further research should be undertaken to explore the eigenvalue distribution of the coupling matrices and how the energy contribution analysis can be extended to sound absorption problems, e.g. decaying sound fields or *in situ* applications. Moreover, research could also be conducted to determine the effectiveness of energy contributions within the NAH method. This would be a fruitful area for future work.

Acknowledgments

References

1. S.-I. Ishiyama, M. Imai, S.-I. Maruyama, H. Ido, N. Sugiura and S. Suzuki, The applications of ACOUST/BOOM — A noise level predicting and reducing computer code, *SAE Trans.* **97** (1988) 976–986.
2. R. A. Adey, S. M. Niku, J. Baynham and P. Burns, Predicting acoustic contributions and sensitivity. Application to vehicle structures, in C. A. Brebbia ed., *Computational Acoustics and its Environmental Applications* (Computational Mechanics Publications, 1995), pp. 181–188.
3. J. P. Coyette, H. Wynendaele and M. K. Chargin, A global acoustic sensitivity tool for improving structural design, in *Proc. SPIE Int. Society for Optical Engineering*, Vol. 1923 (1993), pp. 1389–1394.
4. J. Dong, K. K. Choi and N.-H. Kim, Design optimization of structural–acoustic problems using FEA-BEA with adjoint variable method, *ASME J. Mech. Des.* **126** (2004) 527–533.
5. C. Joachim, D. Nefske and J. Wolf, Application of a structural-acoustic diagnostic technique to reduce boom noise in a passenger vehicle, SAE Technical Paper (1981).
6. Y. Huang and Z. Cui, Recent developments for frequency domain analysis in LS-DYNA®, in *11th European LS-DYNA Conf.* (Salzburg, Austria, 2017).
7. K. Shaposhnikov and M. J. H. Jensen, Panel contribution analysis based on FEM, BEM and numerical Greens function approaches, *J. Theor. Comput. Acoust.* **26**(03) (2018) 1850037.
8. S. Marburg, H.-J. Hardtke, R. Schmidt and D. Pawandenat, Application of the concept of acoustic influence coefficients for the optimization of a vehicle roof, *Eng. Anal. Bound. Elem.* **20** (1997) 305–310.
9. S. Marburg, Efficient optimization of a noise transfer function by modification of a shell structure geometry — Part I: Theory, *Struct. Multidiscip. Optim.* **24**(1) (2002) 51–59.
10. M. Mühlmeier, T. Kumbeim and N. Vogler, Identifikation und Reduzierung der Flächenbeteiligungen am niederfrequenten Innenraumgeräusch, in *Berechnung und Simulation im Fahrzeugbau*, Vol. 1153, VDI Berichte (1994), pp. 221–235.
11. G. Koners, Panel noise contribution analysis: An experimental method for determining the noise contributions of panels to an interior noise, Technical report, SAE Technical Paper (2003).
12. H.-E. De Bree and T. Basten, Microflown based monopole sound sources for reciprocal measurements, SAE Technical Papers (2008).

13. E. G. Williams, *Fourier Acoustics: Sound Radiation and Nearfield Acoustical Holography* (Academic Press, 1999).

14. E. G. Williams, B. H. Houston, P. C. Herdic, S. T. Raveendra and B. Gardner, Interior near-field acoustical holography in flight, *J. Acoust. Soc. Am.* **108**(4) (2000) 1451–1463.

15. B.-K. Kim and J.-G. Ih, On the reconstruction of the vibro-acoustic field over the surface enclosing an interior space using the boundary element method, *J. Acoust. Soc. Am.* **100**(5) (1996) 3003–3016.

16. T. Kletschkowski, M. Weber and D. Sachau, Identification of noise sources in an aircraft fuselage using an inverse method based on a finite element model, *Acta Acust. United With Acust.* **97** (2011) 974–983.

17. J. M. Schmid, E. Fernandez-Grande, M. Hahmann, C. Gurbuz, M. Eser and S. Marburg, Spatial reconstruction of the sound field in a room in the modal frequency range using Bayesian inference, *J. Acoust. Soc. Am.* **150**(6) (2021) 4385–4394.

18. G. H. Koopmann, L. Song and J. B. Fahnline, A method for computing acoustic fields based on the principle of wave superposition, *J. Acoust. Soc. Am.* **86**(6) (1989) 2433–2438.

19. M. Ochmann, The complex equivalent source method for sound propagation over an impedance plane, *J. Acoust. Soc. Am.* **116**(6) (2004) 3304–3311.

20. S. F. Wu, On reconstruction of acoustic pressure fields using the Helmholtz equation least squares method, *J. Acoust. Soc. Am.* **107**(5) (2000) 2511–2522.

21. S. F. Wu, The Helmholtz equation least-squares method, in *The Helmholtz Equation Least Squares Method* (Springer, 2015), pp. 27–62.

22. Z. Wang and S. F. Wu, Helmholtz equation–least-squares method for reconstructing the acoustic pressure field, *J. Acoust. Soc. Am.* **102**(4) (1997) 2020–2032.

23. S. F. Wu and L. K. Natarajan, Panel acoustic contribution analysis, *J. Acoust. Soc. Am.* **133** (2013) 799–809.

24. M. B. S. Magalhaes and R. A. Tenenbaum, Sound sources reconstruction techniques: A review of their evolution and new trends, *Acta Acust. United With Acust.* **90**(2) (2004) 199–220.

25. E. G. Williams, Supersonic acoustic intensity, *J. Acoust. Soc. Am.* **97**(1) (1995) 121–127.

26. E. Fernandez-Grande, F. Jacobsen and Q. Leclere, Direct formulation of the supersonic acoustic intensity in space domain, *J. Acoust. Soc. Am.* **131**(1) (2012) 186–193.

27. S. Marburg, E. Lösche, H. Peters and N. Kessissoglou, Surface contributions to radiated sound power, *J. Acoust. Soc. Am.* **133**(6) (2013) 3700–3705.

28. C. A. Corrêa Junior and R. A. Tenenbaum, Useful intensity: A technique to identify radiating regions on arbitrarily shaped surfaces, *J. Sound Vib.* **332**(6) (2013) 1567–1584.

29. D. Liu, H. Peters, S. Marburg and N. Kessissoglou, Surface contributions to scattered sound power using non-negative intensity, *J. Acoust. Soc. Am.* **140**(2) (2016) 1206–1217.

30. D. Liu, Z. Havránek, S. Marburg, H. Peters and N. Kessissoglou, Non-negative intensity and back-calculated non-negative intensity for analysis of directional structure-borne sound, *J. Acoust. Soc. Am.* **142**(1) (2017) 117–123.

31. D. R. Wilkes, H. Peters, P. Croaker, S. Marburg, A. J. Duncan and N. Kessissoglou, Non-negative intensity for coupled fluid–structure interaction problems using the fast multipole method, *J. Acoust. Soc. Am.* **141**(6) (2017) 4278–4288.

32. D. Liu, S. Marburg and N. Kessissoglou, Non-negative intensity for target strength identification in marine ecosystem research, *J. Theor. Comput. Acoust.* **30**(01) (2022) 2150023.

33. M. Karimi, L. Maxit, V. Meyer, S. Marburg and R. Kirby, Non-negative intensity for planar structures under stochastic excitation, *J. Sound Vib.* **488** (2020) 115652.

34. D. Liu, S. Marburg, C. Geweth and N. Kessissoglou, Non-negative intensity for structures with inhomogeneous damping, *J. Theor. Comput. Acoust.* **27**(01) (2019) 1850050.

35. E. G. Williams, Convolution formulations for non-negative intensity, *J. Acoust. Soc. Am.* **134**(2) (2013) 1055–1066.
36. D. Liu, H. Peters, S. Marburg and N. Kessissoglou, Supersonic intensity and non-negative intensity for prediction of radiated sound, *J. Acoust. Soc. Am.* **139**(5) (2016) 2797–2806.
37. S. D. Sommerfeldt and P. J. Nashif, An adaptive filtered-x algorithm for energy-based active control, *J. Acoust. Soc. Am.* **96**(1) (1994) 300–306.
38. N. Tanaka and K. Kobayashi, Cluster control of acoustic potential energy in a structural/acoustic cavity, *J. Acoust. Soc. Am.* **119**(5) (2006) 2758–2771.
39. B. S. Cazzolato and C. H. Hansen, Active control of sound transmission using structural error sensing, *J. Acoust. Soc. Am.* **104**(5) (1998) 2878–2889.
40. B. S. Cazzolato, Sensing systems for active control of sound transmission into cavities, Dissertation, The University of Adelaide (1999).
41. B. S. Cazzolato and C. H. Hansen, Errors arising from three-dimensional energy density sensing in one-dimensional sound fields, *J. Sound Vib.* **236**(3) (2000) 375–400.
42. C. Gurbuz, J. D. Schmid, M. Luegmair and S. Marburg, Energy density-based non-negative surface contributions in interior acoustics, *J. Sound Vib.* **527** (2022) 116824.
43. G. H. Koopmann and J. B. Fahnline, *Designing Quiet Structures: A Sound Power Minimization Approach* (Academic Press, 1997).
44. S. Marburg, Developments in structural–acoustic optimization for passive noise control, *Arch. Comput. Methods Eng.* **9**(4) (2002) 291–370.
45. S. Preuss, C. Gurbuz, C. Jelich, S. K. Baydoun and S. Marburg, Recent advances in acoustic boundary element methods, *J. Theor. Comput. Acoust.* **30** (2022) 2240002.
46. S. Marburg, F. Dienerowitz, T. Horst and S. Schneider, Normal modes in external acoustics. Part II: Eigenvalues and eigenvectors in 2D, *Acta Acust. United With Acust.* **92**(1) (2006) 97–111.
47. S. Marburg, Normal modes in external acoustics. Part III: Sound power evaluation based on superposition of frequency-independent modes, *Acta Acust. United With Acust.* **92**(2) (2006) 296–311.
48. S. Marburg and R. Anderssohn, Fluid structure interaction and admittance boundary conditions: Setup of an analytical example, *J. Comput. Acoust.* **19**(01) (2011) 63–74.
49. S. Marburg, Boundary element method for time-harmonic acoustic problems, in *Computational Acoustics*, ed. M. Kaltenbacher (Springer, Cham, 2018), pp. 69–158.
50. T. Wu and A. Seybert, A weighted residual formulation for the CHIEF method in acoustics, *J. Acoust. Soc. Am.* **90**(3) (1991) 1608–1614.
51. L. E. Kinsler, A. R. Frey, A. B. Coppens and J. V. Sanders, *Fundamentals of Acoustics* (John Wiley & Sons, 1999).
52. S. Marburg and S. Schneider, Influence of element types on numeric error for acoustic boundary elements, *J. Comput. Acoust.* **11**(03) (2003) 363–386.
53. S. Marburg and H.-J. Hardtke, A study on the acoustic boundary admittance. Determination, results and consequences, *Eng. Anal. Bound. Elem.* **23**(9) (1999) 737–744.
54. M. Luegmair and J. D. Schmid, Challenges in vibroacoustic vehicle body simulation including uncertainties, SAE Technical Paper (2020).
55. C. Gurbuz, M. Eser, J. D. Schmid and S. Marburg, Gaussian processes for transfer path analysis applied on vehicle body vibration problems, SAE Technical Paper (2022).
56. J. D. Schmid, A. Hildenbrand, C. Gurbuz, M. Luegmair and S. Marburg, Variational autoencoders for dimensionality reduction of automotive vibroacoustic models, SAE Technical Paper (2022).

A.3 Paper C

A multi-fidelity Gaussian process for efficient frequency sweeps in the acoustic design of a vehicle cabin

Caglar Gurbuz, Martin Eser, Johannes Schaffner, and Steffen Marburg

JASA ARTICLE

CrossMark
click for updates

A multi-fidelity Gaussian process for efficient frequency sweeps in the acoustic design of a vehicle cabin

Caglar Gurbuz,[a] (iD) Martin Eser, (iD) Johannes Schaffner, and Steffen Marburg (iD)

Vibroacoustics of Vehicles and Machines, Technical University of Munich, Garching 85748, Germany

ABSTRACT:

Highly accurate predictions from large-scale numerical simulations are associated with increased computational resources and time expense. Consequently, the data generation process can only be performed for a small sample size, limiting a detailed investigation of the underlying system. The concept of multi-fidelity modeling allows the combination of data from different models of varying costs and complexities. This study introduces a multi-fidelity model for the acoustic design of a vehicle cabin. Therefore, two models with different fidelity levels are used to solve the Helmholtz equation at specified frequencies with the boundary element method. Gaussian processes (GPs) are trained on each fidelity level with the simulation results to predict the unknown system response. In this way, the multi-fidelity model enables an efficient approximation of the frequency sweep for acoustics in the frequency domain. Additionally, the proposed method inherently considers uncertainties due to the data generation process. To demonstrate the effectiveness of our framework, the multifrequency solution is validated with the high-fidelity (HF) solution at each frequency. The results show that the frequency sweep is efficiently approximated by using only a limited number of HF simulations. Thus, these findings indicate that multi-fidelity GPs can be adopted for fast and, simultaneously, accurate predictions.

I. INTRODUCTION

A key aspect in acoustic design processes is the fast and accurate characterization of the acoustic system. Rising requirements on modern products demand a drastic increase in the complexity of the model. Consequently, design tasks, such as sensitivity analyses and structural-acoustic optimizations, are generally associated with high computational costs (Marburg, 2002). Thus, engineers and researchers are faced with the challenge of finding solutions for large problems on the basis of small data. Ideally, their models should be fast to evaluate and, at the same time, highly accurate. However, models with a high predictive quality are generally accompanied with high demands on resources and time, whereas models, which are fast to evaluate, are usually less accurate.

Traditionally, detailed analyses are performed to assess the acoustic properties of a system. These can either be cumbersome physical experiments, e.g., measurements in an impedance tube or a reverberation chamber, or expensive numerical simulations with the finite element method (FEM) or boundary element method (BEM). At the same time, various analytical and numerical models at small scale exist, which can already yield a decent approximation of the relevant acoustic solution. One specific problem in acoustics is associated with the approximation of the frequency sweep when using BEM simulations. Existing methods, e.g., greedy

approximation (Baydoun *et al.*, 2020; Baydoun *et al.*, 2021; Jelich *et al.*, 2021) or parametric model order reduction (Panagiotopoulos *et al.*, 2022; Xie and Liu, 2021; Xie *et al.*, 2022; Xie *et al.*, 2023), already provide an efficient multifrequency solution technique. However, uncertainties, whether in the model parameters or due to the random nature of the data generation process, are not quantified within these methods. The efficient solution for a wide frequency range under uncertainties is particularly important in the acoustic design of a vehicle cabin (Gurbuz *et al.*, 2022a; Schmid *et al.*, 2022). Moreover, recent evidence suggests to prefer the sound energy density to the sound pressure as a control objective in interior acoustic problems (Cazzolato and Hansen, 1998; Gurbuz and Marburg, 2022; Gurbuz *et al.*, 2022b; Koopmann and Fahnline, 1997; Sommerfeldt and Nashif, 1994; Tanaka and Kobayashi, 2006). With the sound energy density being sensitive to the sound pressure and particle velocity, the sound energy density provides a robust objective function.

Gaussian processes (GPs) provide a useful technique to substitute a complex model by an efficient surrogate model (Hoffer *et al.*, 2022). In the sense of a Bayesian method, GPs allow to embed prior knowledge of the underlying problem and further enable predictions under consideration of uncertainties (Cutajar *et al.*, 2019; Williams and Rasmussen, 2006). In particular, GPs account for two types of uncertainties: aleatoric and epistemic. Aleatoric or statistical

uncertainties refer to the random nature of the data generation process. For instance, the output of an experiment changes when repeated. In contrast to this, epistemic or systematic uncertainties are defined as uncertainties resulting from limited knowledge of the underlying problem. In this case, it involves simplifying assumptions on the model or limited information on the model parameters. As a matter of fact, epistemic uncertainties can be mitigated by incorporating additional information. Aleatoric uncertainties, on the other hand, would remain unaffected here (Hüllermeier and Waegeman, 2021; Soize, 2017).

Raissi et al. (2017b) reported on GPs which are used to solve linear partial differential equations. These authors further extended their method to time-dependent and nonlinear problems (Raissi et al., 2018). In the field of acoustics, GPs were adopted as a surrogate model in a transfer path analysis of a vehicle cabin (Gurbuz et al., 2022a). GPs were further used as an alternative to Bayesian inference (Schmid et al., 2021) to infer a two-dimensional sound field based on a limited number of sound pressure observations (Caviedes-Nozal et al., 2021). In ocean acoustics, GPs have been applied in a source localization technique (Michalopoulou et al., 2021) and the quantification of uncertainties (Michalopoulou and Gerstoft, 2022; Yardim et al., 2011). Further source localization methods based on GPs have been reported for the sound emitted by a complex aerospace component (Hensman et al., 2010) and general two-dimensional sound radiation problems (Albert and Rath, 2020). In the latter work, the authors implemented a physics-informed approach. In a more recent study, GPs were integrated in a framework for the detection and characterization of cracks in rocks (Jiang et al., 2022).

A multi-fidelity model allows the combination of multiple models with differing fidelity levels. Typically, it consists of a low-fidelity (LF) and high-fidelity (HF) model. LF models can be attributed to low computational costs and decreased accuracy, whereas HF models can achieve predictions with higher accuracy for the burden of high expenses. In many engineering fields, analytical or numerical models at small scale can be regarded as LF models. On the other hand, highly resolved numerical models or cumbersome physical experiments can be considered to be HF models. As such, the advantages of both fidelity levels, namely, fast evaluations and high accuracy, are merged in a multi-fidelity model.

The first serious discussion and analysis of multi-fidelity modeling emerged in 1998 with the work of Craig et al (1998), introducing multi-fidelity models on the basis of linear regression. This model was further extended by using Bayesian linear regression for high-dimensional problems (Cumming and Goldstein, 2009). Another landmark study has been proposed by Kennedy and O'Hagan (2000), who developed a multi-fidelity model based on GPs. This method was further improved by a recursive formulation for the different fidelity levels (Le Gratiet and Garnier, 2014). Marburg and Hardtke (2001) applied the idea of multiple models with different predictive capabilities on an acoustic

design task, yet, without using the term multi-fidelity. More recent attention has focused on multi-fidelity models for the solution of partial differential equations (Parussini et al., 2017; Raissi et al., 2017a). Beyond GPs, artificial neural networks have been implemented in multi-fidelity schemes for parameter-dependent outputs (Guo et al., 2022) or discontinuities between the fidelity levels (Raissi and Karniadakis, 2016). This type of multi-fidelity model was further applied to a structural health monitoring problem (Torzoni et al., 2023).

The aim of this study is the development of an efficient multifrequency solution strategy for accurate predictions under the consideration of uncertainties. For this purpose, a multi-fidelity model comprising two levels of fidelity is deployed. Regarding the LF and HF models, GPs are adopted as surrogates. These surrogates are trained on the sound field data obtained by the BEM. Therefore, the acoustic Helmholtz equation is solved for two different refinements of the boundary element mesh. The solution of the fine mesh is considered to be the HF data while the frequency response of the coarse mesh is adopted as the LF data. To validate the proposed multi-fidelity model, a vehicle interior noise problem is investigated. As recently suggested, we analyze two objective functions: the sound pressure and sound energy density (Gurbuz et al., 2022b). By using a multi-fidelity model, a high predictive quality can be ensured for only a small number of BEM simulations.

This paper is structured as follows. Section II briefly outlines the Helmholtz equation, BEM, and relevant acoustic field quantities, i.e., the sound pressure and sound energy density. Section III provides the fundamentals of GPs. In Sec. IV, the theoretical background of multi-fidelity models is provided. The results for an industrial vehicle interior noise problem are presented in Sec. V. The conclusions are drawn in Sec. VI.

II. BEM

The acoustic problem setup and BEM are only briefly introduced here. For a detailed description, the interested reader is referred to Marburg (2018), Marburg (2008), and Wu (2002). By assuming the harmonic time dependence, $e^{-i\omega t}$, the interior acoustic problem in the frequency domain is governed by the Helmholtz equation,

$$\Delta p(\vec{x}) + k^2 p(\vec{x}) = 0, \quad \vec{x} \in \Omega \subset \mathbb{R}^3, \tag{1}$$

with the scalar, complex-valued sound pressure, $p(\vec{x})$, in the domain, Ω. The wavenumber is denoted by $k = \omega/c$ with the angular frequency, ω, and speed of sound, c. In this study, we focus on air-filled domains. Thus, we introduce the index "a" to refer to the material properties of air, i.e., for the speed of sound, $c = c_a$, and density, $\rho = \rho_a$.

The Robin boundary condition is formulated as (Suzuki et al., 1989)

$$v_f(\vec{x}) - v_s(\vec{x}) = Y(\vec{x})p(\vec{x}), \quad \vec{x} \in \Gamma \subset \mathbb{R}^2, \tag{2}$$

J. Acoust. Soc. Am. **153** (4), April 2023

Gurbuz et al.   2007

where $v_f(\vec{x})$, $v_s(\vec{x})$, and $Y(\vec{x})$ denote the normal fluid particle velocity, normal structural velocity, and boundary admittance at the boundary, Γ. The sound pressure on the boundary is related to the normal fluid particle velocity by the linearized Euler equation,

$$v_f(\vec{x}) = \frac{1}{i\omega\rho_a} \frac{\partial p(\vec{x})}{\partial n(\vec{x})}, \quad \vec{x} \in \Gamma \subset \mathbb{R}^2, \tag{3}$$

where the ambient density of the acoustic medium is ρ_a. The normal structural particle velocity is used to impose a vibrating pattern on the surface, whereas the Robin boundary condition is adopted to model the absorbing behavior of the enveloping structure.

The Kirchhoff-Helmholtz boundary integral equation reads

$$c(\vec{y})p(\vec{y}) + \int_\Gamma \frac{\partial G(\vec{x}, \vec{y})}{\partial n(\vec{x})} p(\vec{x}) d\Gamma(\vec{x})$$
$$= i\omega\rho_a \int_\Gamma G(\vec{x}, \vec{y}) v_f(\vec{x}) d\Gamma(\vec{x}), \quad \vec{x}, \vec{y} \in \Gamma \subset \mathbb{R}^2, \tag{4}$$

where the Green's function is $G(\vec{x}, \vec{y}) = e^{ikr}/(4\pi r)$ and the Euclidean distance is $r = r(\vec{x}, \vec{y})$. The quantity, $c(\vec{y})$, represents a geometric entity, which is determined by the boundary contour at the position, $\vec{y}$. On smooth boundaries, $c(\vec{y})$ is equal to 0.5 (Marburg, 2018). Finally, substituting Eq. (2) into Eq. (4) and discretizing the resulting equation with the collocation method yields the following linear system of equations (Marburg, 2018; Marburg, 2008):

$$[\boldsymbol{H}(k) - \boldsymbol{G}(k)\boldsymbol{Y}(k)]\boldsymbol{p}(k) = \boldsymbol{G}(k)\boldsymbol{v}_s(k). \tag{5}$$

The entity, $\boldsymbol{G}(k)$, denotes the matrix of the single layer potential, whereas $\boldsymbol{H}(k)$ is referred to as the matrix of the double layer potential. These matrices are neither Hermitian nor positive definite. As the entries of the system matrices, $\boldsymbol{G}(k)$ and $\boldsymbol{H}(k)$, are determined by the Green's function and its normal derivative, respectively, it becomes obvious that the system matrices depend on the wavenumber and, thus, on the frequency. As a consequence, the sound pressure solution, $\boldsymbol{p}(k)$, in Eq. (5) depends on the frequency. To obtain the system response in a certain frequency range, Eq. (5) has to be solved for each discrete frequency within the relevant frequency range.

In interior acoustic problems, it is widely adopted to use the sound pressure at a specific location as an objective function to characterize the acoustic system. The sound pressure inside of a cavity can be obtained by evaluating Eq. (4) in the acoustic field, Ω,

$$p_i(\vec{y}) = i\omega\rho_a \int_\Gamma G(\vec{x}, \vec{y}) v_s(\vec{x}) d\Gamma(\vec{x}) - \int_\Gamma \left[\frac{\partial G(\vec{x}, \vec{y})}{\partial n(\vec{x})} \right.$$
$$\left. - i\omega\rho \, G(\vec{x}, \vec{y})Y(\vec{x}) \right] p(\vec{x}) d\Gamma(\vec{x}), \quad \vec{y} \in \Omega, \tag{6}$$

where $p_i(\vec{y})$ denotes the field point sound pressure. Similarly, by exploiting Eq. (3), the particle velocity at a field point is computed by

$$\vec{v}_i(\vec{y}) = \int_\Gamma \vec{\nabla} G(\vec{x}, \vec{y}) v_s(\vec{x}) d\Gamma(\vec{x}) - \left[\int_\Gamma \vec{\nabla} \frac{1}{i\omega\rho_a} \frac{\partial G(\vec{x}, \vec{y})}{\partial n(\vec{x})} \right.$$
$$\left. - \vec{\nabla} G(\vec{x}, \vec{y})Y(\vec{x}) \right] p(\vec{x}) d\Gamma(\vec{x}), \quad \vec{y} \in \Omega, \tag{7}$$

where the field point particle velocity is $\vec{v}_i(\vec{y})$ (Wu and Seybert, 1991).

Recent evidence (Cazzolato and Hansen, 1998; Gurbuz et al., 2022b; Koopmann and Fahnline, 1997; Sommerfeldt and Nashif, 1994), however, suggests to use the sound energy density as a control objective because the sound pressure evaluation shows a poor performance in regions with low sound pressure values. This results from the fact that the sound pressure heavily depends on the evaluated position. Thus, a deteriorated performance is to be expected when the sound pressure is observed in the vicinity of a pressure node. As opposed to that, the sound energy density is relatively robust to the position of the evaluation point. Therefore, it was suggested as a control objective for interior acoustic problems.

With two energy forms transported in sound waves (Kinsler et al., 2000), the sound energy density is composed by the potential energy density,

$$e_p(\vec{y}) = \frac{1}{2\rho_a c_a^2} p_i^*(\vec{y}) p_i(\vec{y}), \tag{8}$$

and the kinetic energy density,

$$e_k(\vec{y}) = \frac{\rho_a}{4} \vec{v}_i^*(\vec{y}) \vec{v}_i(\vec{y}). \tag{9}$$

The total sound energy density is then obtained by

$$e_t(\vec{y}) = e_p(\vec{y}) + e_k(\vec{y})$$
$$= \frac{1}{2\rho_a c_a^2} p_i^*(\vec{y}) p_i(\vec{y}) + \frac{\rho_a}{4} \vec{v}_i^*(\vec{y}) \vec{v}_i(\vec{y}). \tag{10}$$

Equation (10) highlights that the sound energy density is sensitive to the sound pressure and particle velocity. In this way, the sound energy density provides a robust objective function, particularly, in regions with low sound pressure levels (SPLs). Further details on that topic are provided in Gurbuz and Marburg (2022), Gurbuz et al. (2022b), and Preuss et al. (2022).

III. GPS

A GP is defined as a collection of random variables which are jointly Gaussian distributed. As such, a GP can be interpreted as a probability distribution over functions. With h denoting the unknown frequency response function, the GP can be expressed by

$$h(\mathbf{f}) \sim \mathcal{GP}(m(\mathbf{f}), \mathrm{cov}(\mathbf{f}, \mathbf{f}')). \tag{11}$$

A GP is specified by a mean function, $m(\mathbf{f})$, and a covariance function or kernel, $\mathrm{cov}(\mathbf{f}, \mathbf{f}')$, where $\mathbf{f}$ and $\mathbf{f}'$ denote two sets of input frequency points (Raissi et al., 2017b).

2008   J. Acoust. Soc. Am. **153** (4), April 2023

Gurbuz *et al.*

In this study, the squared exponential covariance function,

$$\text{cov}(\mathbf{f}, \mathbf{f}') = \sigma_f^2 \exp\left(-\frac{1}{2l^2}(\mathbf{f} - \mathbf{f}')^T(\mathbf{f} - \mathbf{f}')\right), \quad (12)$$

with the characteristic length, l, and signal variance, σ_f^2, is adopted. These parameters essentially specify the characteristics of the GP. They are, thus, commonly referred to as hyperparameters. Note that this covariance function depends only on the frequency input points. The covariance of the outputs, namely, the frequency response function, is only determined by the input covariance. Closer inspection at Eq. (12) reveals that the output increases when the distance between the input points decreases (Williams and Rasmussen, 2006).

The GP prior, which defines the GP without any observations, can be then expressed by

$$\mathbf{h} \sim \mathcal{N}(\mathbf{0}, \text{cov}(\mathbf{f}, \mathbf{f}')), \quad (13)$$

where $\mathcal{N}$ denotes a multivariate Gaussian probability distribution. Note that the observed quantities are the real-valued SPL and real-valued sound energy density level. Therefore, the real-valued multivariate Gaussian distribution, $\mathcal{N}$, was chosen here. In this initial study, we assume that the frequency response function is zero prior to the involvement of any observed data. As a consequence, the mean function can be set to zero.

So far, the GP prior in Eq. (13) does not account for any physical information about the system. The great advantage of GPs emerges by incorporating observed data of the underlying physical process. Therefore, the joint probability distribution of the observed function outputs, $\mathbf{h}$, and the unknown frequency responses, $\mathbf{h}_*$, at new frequencies, $\mathbf{f}_*$, are introduced as

$$\begin{bmatrix} \mathbf{h} \\ \mathbf{h}_* \end{bmatrix} \sim \mathcal{N}\left(\mathbf{0}, \begin{bmatrix} \mathbf{K}(\mathbf{f}, \mathbf{f}) & \mathbf{K}(\mathbf{f}, \mathbf{f}_*) \\ \mathbf{K}(\mathbf{f}_*, \mathbf{f}) & \mathbf{K}(\mathbf{f}_*, \mathbf{f}_*) \end{bmatrix}\right). \quad (14)$$

The matrix, $\mathbf{K}$, denotes the evaluated covariance function for the frequencies, $\mathbf{f}$, at which observations are available, and frequencies, $\mathbf{f}_*$, at which the frequency responses are unknown. For n known frequency points, the dimension of $\mathbf{K}(\mathbf{f}, \mathbf{f})$ amounts to $n \times n$. Analogously, for n_* frequency points with unknown responses, the remaining sub-matrices, $\mathbf{K}(\mathbf{f}_*, \mathbf{f})$, $\mathbf{K}(\mathbf{f}, \mathbf{f}_*)$, and $\mathbf{K}(\mathbf{f}_*, \mathbf{f}_*)$ are of sizes $n_* \times n$, $n \times n_*$, and $n_* \times n_*$, respectively. Now, by conditioning the joint GP prior on the observed data, the joint posterior probability distribution for the unknown frequency response function is expressed by

$$P(\mathbf{h}_*|\mathbf{f}_*, \mathbf{f}, \mathbf{h}) \sim \mathcal{N}\Big(\mathbf{K}(\mathbf{f}_*, \mathbf{f})\mathbf{K}(\mathbf{f}, \mathbf{f})^{-1}\mathbf{h}, \ \mathbf{K}(\mathbf{f}_*, \mathbf{f}_*)$$
$$- \mathbf{K}(\mathbf{f}_*, \mathbf{f})\mathbf{K}(\mathbf{f}, \mathbf{f})^{-1}\mathbf{K}(\mathbf{f}, \mathbf{f}_*)\Big). \quad (15)$$

The interested reader is referred to the Appendix for an outline of the conditioning process.

Equation (15) serves as a viable implementation for noiseless data. In reality, however, data generation processes are subject to noise resulting in noisy observations. In that case, the observations can be modeled with $\mathbf{y} = \mathbf{h}(\mathbf{f}) + \epsilon$ under the assumption of additive Gaussian distributed noise. For noisy observations, the covariance function in Eq. (12) adapts to

$$\text{cov}(\mathbf{f}, \mathbf{f}') = \mathbf{K}(\mathbf{f}, \mathbf{f}) + \sigma_n^2\mathbf{I}$$
$$= \sigma_f^2 \exp\left(-\frac{1}{2l^2}(\mathbf{f} - \mathbf{f}')^T(\mathbf{f} - \mathbf{f}')\right) + \sigma_n^2\mathbf{I}, \quad (16)$$

where the noise level is σ_n^2 and the identity matrix is $\mathbf{I}$, i.e., $\epsilon \sim \mathcal{N}(\mathbf{0}, \sigma_n^2\mathbf{I})$. The joint probability distribution of the noisy observations, $\mathbf{y}$, and frequency responses, $\mathbf{h}_*$, of interest then reads

$$\begin{bmatrix} \mathbf{y} \\ \mathbf{h}_* \end{bmatrix} \sim \mathcal{N}\left(\mathbf{0}, \begin{bmatrix} \mathbf{K}(\mathbf{f}, \mathbf{f}) + \sigma_n^2\mathbf{I} & \mathbf{K}(\mathbf{f}, \mathbf{f}_*) \\ \mathbf{K}(\mathbf{f}_*, \mathbf{f}) & \mathbf{K}(\mathbf{f}_*, \mathbf{f}_*) \end{bmatrix}\right). \quad (17)$$

Conditioning the joint distribution in Eq. (17) on the observed data yields then the predictive posterior GP,

$$P(\mathbf{h}_*|\mathbf{f}_*, \mathbf{f}, \mathbf{y}) \sim \mathcal{N}(\bar{\mathbf{h}}_*, \text{cov}(\mathbf{h}_*)), \quad (18)$$

where

$$\bar{\mathbf{h}}_* = \mathbf{K}(\mathbf{f}_*, \mathbf{f})\big[\mathbf{K}(\mathbf{f}, \mathbf{f}) + \sigma_n^2\mathbf{I}\big]^{-1}\mathbf{y}, \quad (19)$$

$$\text{cov}(\mathbf{h}_*) = \mathbf{K}(\mathbf{f}_*, \mathbf{f}_*) - \mathbf{K}(\mathbf{f}_*, \mathbf{f})\big[\mathbf{K}(\mathbf{f}, \mathbf{f}) + \sigma_n^2\mathbf{I}\big]^{-1}\mathbf{K}(\mathbf{f}, \mathbf{f}_*)^T. \quad (20)$$

The posterior GP is determined by the predictive mean, $\bar{\mathbf{h}}_*$, and predictive covariance, $\text{cov}(\mathbf{h}_*)$. By this means, the posterior GP is fully specified and can be used as a surrogate model for a complex acoustic system (Williams and Rasmussen, 2006).

To obtain the optimal set of hyperparameters, the negative log likelihood function (Williams and Rasmussen, 2006),

$$\log P(\mathbf{y}|\mathbf{f}) = -\frac{1}{2}\mathbf{y}^T(\mathbf{K}(\mathbf{f}, \mathbf{f}) + \sigma_n^2\mathbf{I}))\mathbf{y}$$
$$- \frac{1}{2}\log|\mathbf{K}(\mathbf{f}, \mathbf{f}) + \sigma_n^2\mathbf{I}| - \frac{n}{2}\log 2\pi, \quad (21)$$

is minimized with respect to the characteristic length, l, signal variance, σ_f^2, and noise level, σ_n^2. Equation (21) estimates how likely the observation is for the given training inputs. In the literature, the term "training" is generally understood as the treatment of the optimization problem in Eq. (21).

IV. MULTI-FIDELITY MODEL

Following Kennedy and O'Hagan (2000), we assume that the prediction of the HF model, $\mathbf{h}_H(\mathbf{f})$, can be approximated by the solution of a lower fidelity version, $\mathbf{h}_L(\mathbf{f})$. This property

J. Acoust. Soc. Am. **153** (4), April 2023

Gurbuz *et al.*   2009

defines an autoregressive model, which is expressed by (Kennedy and O'Hagan, 2000; Le Gratiet and Garnier, 2014)

$$\mathbf{h}_H(\mathbf{f}) = \eta\, \mathbf{h}_L(\mathbf{f}) + \boldsymbol{\delta}(\mathbf{f}), \tag{22}$$

with the coupling parameter, η, and two independent GPs,

$$\mathbf{h}_L \sim \mathcal{GP}(0, \mathrm{cov}_L(\mathbf{f}, \mathbf{f}')), \tag{23}$$

$$\boldsymbol{\delta} \sim \mathcal{GP}(0, \mathrm{cov}_H(\mathbf{f}, \mathbf{f}')). \tag{24}$$

In Eqs. (22)–(24), the subscripts, L and H, denote the affiliation to the LF and HF models, respectively. For $\eta = 0$, it

$$\begin{bmatrix} \mathbf{h}_L \\ \mathbf{h}_H \end{bmatrix} \sim \mathcal{GP}\left(\begin{bmatrix} \mathbf{0} \\ \mathbf{0} \end{bmatrix}, \begin{bmatrix} \mathrm{cov}_L(\mathbf{f}_L, \mathbf{f}_L) & \eta\, \mathrm{cov}_L(\mathbf{f}_L, \mathbf{f}_H) \\ \eta\, \mathrm{cov}_L(\mathbf{f}_L, \mathbf{f}_H) & \eta^2\, \mathrm{cov}_L(\mathbf{f}_L, \mathbf{f}_H) + \mathrm{cov}_H(\mathbf{f}_L, \mathbf{f}_H) \end{bmatrix} \right), \tag{25}$$

or in compact form, where $\mathrm{cov}_{LL} = \mathrm{cov}_L$, $\mathrm{cov}_{LH} = \mathrm{cov}_{HL} = \eta\, \mathrm{cov}_L$, and $\mathrm{cov}_{HH} = \eta^2\, \mathrm{cov}_L + \mathrm{cov}_H$,

$$\begin{bmatrix} \mathbf{h}_L \\ \mathbf{h}_H \end{bmatrix} \sim \mathcal{GP}\left(\begin{bmatrix} \mathbf{0} \\ \mathbf{0} \end{bmatrix}, \begin{bmatrix} \mathrm{cov}_{LL}(\mathbf{f}_L, \mathbf{f}_L) & \mathrm{cov}_{LH}(\mathbf{f}_L, \mathbf{f}_H) \\ \mathrm{cov}_{HL}(\mathbf{f}_L, \mathbf{f}_H) & \mathrm{cov}_{HH}(\mathbf{f}_L, \mathbf{f}_H) \end{bmatrix} \right). \tag{26}$$

By including the frequencies, $\mathbf{f}_*$, at which we are interested in the response function, $\mathbf{h}_*$, the multi-fidelity GP adapts to

$$\begin{bmatrix} \mathbf{h}_* \\ \mathbf{h}_L \\ \mathbf{h}_H \end{bmatrix} \sim \mathcal{GP}\left(\begin{bmatrix} \mathbf{0} \\ \mathbf{0} \\ \mathbf{0} \end{bmatrix}, \begin{bmatrix} \mathrm{cov}_{**}(\mathbf{f}_*, \mathbf{f}_*) & \mathrm{cov}_{*L}(\mathbf{f}_*, \mathbf{f}_L) & \mathrm{cov}_{*H}(\mathbf{f}_*, \mathbf{f}_H) \\ \mathrm{cov}_{L*}(\mathbf{f}_L, \mathbf{f}_*) & \mathrm{cov}_{LL}(\mathbf{f}_L, \mathbf{f}_L) & \mathrm{cov}_{LH}(\mathbf{f}_L, \mathbf{f}_H) \\ \mathrm{cov}_{H*}(\mathbf{f}_H, \mathbf{f}_*) & \mathrm{cov}_{HL}(\mathbf{f}_L, \mathbf{f}_H) & \mathrm{cov}_{HH}(\mathbf{f}_H, \mathbf{f}_H) \end{bmatrix} \right). \tag{27}$$

Conditioning Eq. (27) on the observed LF and HF data then yields the predictive posterior GP for the unknown frequency responses,

$$P(\mathbf{h}_*|\mathbf{f}_*, \mathbf{f}_L, \mathbf{h}_L, \mathbf{f}_H, \mathbf{h}_H) = \mathcal{N}(\mathbf{K}_*\mathbf{K}^{-1}\mathbf{h}, \mathbf{K}_{**} \\ - \mathbf{K}_*\mathbf{K}^{-1}\mathbf{K}_*^T), \tag{28}$$

with

$$\mathbf{h} = \begin{bmatrix} \mathbf{h}_L & \mathbf{h}_H \end{bmatrix}^T, \tag{29}$$

$$\mathbf{K}_* = \begin{bmatrix} \mathrm{cov}_{*L}(\mathbf{f}_*, \mathbf{f}_L) & \mathrm{cov}_{*H}(\mathbf{f}_*, \mathbf{f}_H) \end{bmatrix}, \tag{30}$$

$$\mathbf{K} = \begin{bmatrix} \mathrm{cov}_{LL}(\mathbf{f}_L, \mathbf{f}_L) & \mathrm{cov}_{LH}(\mathbf{f}_L, \mathbf{f}_H) \\ \mathrm{cov}_{HL}(\mathbf{f}_H, \mathbf{f}_L) & \mathrm{cov}_{HH}(\mathbf{f}_H, \mathbf{f}_H) \end{bmatrix}, \tag{31}$$

$$\mathbf{K}_{**} = \begin{bmatrix} \mathrm{cov}_{**}(\mathbf{f}_*, \mathbf{f}_*) \end{bmatrix}. \tag{32}$$

Equations (28)–(32) fully describe the posterior multi-fidelity GP for noise-free predictions at the frequencies, $\mathbf{f}_*$, where we are interested in the frequency responses.

For noisy observations, $\mathbf{y}_L$ and $\mathbf{y}_H$, the predictive posterior distribution is expressed by

$$P(\mathbf{h}_*|\mathbf{f}_*, \mathbf{f}_L, \mathbf{y}_L, \mathbf{f}_H, \mathbf{y}_H) = \mathcal{N}(\mathbf{K}_*\mathbf{K}^{-1}\mathbf{y}, \mathbf{K}_{**} \\ - \mathbf{K}_*\mathbf{K}^{-1}\mathbf{K}_*^T), \tag{33}$$

becomes evident that the LF and HF models are uncorrelated. In this case, the multi-fidelity model will not lead to any improvement (Raissi and Karniadakis, 2016). Note that the multi-fidelity model in Eqs. (22)–(24) is adjustable by two covariance functions, cov_L and cov_H. However, in this initial study, the squared exponential covariance function in Eq. (12) is adopted for both kernel functions.

By introducing the frequency and frequency response function data pairs for the LF level, $[\mathbf{f}_L, \mathbf{h}_L]$, and HF level, $[\mathbf{f}_H, \mathbf{h}_H]$, the multi-fidelity GP prior can be formulated as

where $\mathbf{y} = [\mathbf{y}_L\, \mathbf{y}_H]$. In addition to this, the covariance matrix regarding the training points adapts to

$$\mathbf{K} = \begin{bmatrix} \mathrm{cov}_{LL}(\mathbf{f}_L, \mathbf{f}_L) + \sigma_{nL}^2\mathbf{I} & \mathrm{cov}_{LH}(\mathbf{f}_L, \mathbf{f}_H) \\ \mathrm{cov}_{HL}(\mathbf{f}_H, \mathbf{f}_L) & \mathrm{cov}_{HH}(\mathbf{f}_H, \mathbf{f}_H) + \sigma_{nH}^2\mathbf{I} \end{bmatrix}, \tag{34}$$

with the noise levels, σ_{nL}^2 and σ_{nH}^2, inherent to the LF and HF data, respectively.

Regarding the magnitudes of the acoustic quantities, the noise level transfers to the signal-to-noise ratio (SNR) according to

$$\mathrm{SNR} = 10 \log\left(\frac{\mathbf{y}\,\mathbf{y}^T}{\sigma_n^2} \right). \tag{35}$$

In the first study, the SPL at the driver's ear is adopted as the objective function. In the second case, the sound energy density level at the same field point is considered.

Last, the negative log likelihood function is rewritten as

$$\log P(\mathbf{y}|\mathbf{f}) = -\frac{1}{2}\mathbf{y}^T\left[\mathbf{K}(\mathbf{f}, \mathbf{f}) + \sigma_n^2\mathbf{I}\right]^{-1}\mathbf{y} - \frac{1}{2}\log\left|\mathbf{K}(\mathbf{f}, \mathbf{f}) \\ + \sigma_n^2\mathbf{I}\right| - \frac{n_L + n_H}{2}\log 2\pi \tag{36}$$

for the multi-fidelity GP with noisy observations, $\mathbf{y}$. Analogously, the input frequency points and noise levels for

2010   J. Acoust. Soc. Am. **153** (4), April 2023

Gurbuz *et al.*

the LF and HF data are comprised in $\mathbf{f} = [\mathbf{f}_L \, \mathbf{f}_H]$ and $\sigma_n^2 = [\sigma_{nL}^2 \, \sigma_{nH}^2]$, respectively. The corresponding numbers of input points are denoted by n_L and n_H. In accordance with Williams and Rasmussen (2006), Algorithm 1 schematically depicts the implementation of the multi-fidelity GP. Note that the matrix inversion of $[\mathbf{K} + \sigma_n^2 \mathbf{I}]$ is circumvented by using its Cholesky decomposition for the sake of computational efficiency and robustness.

ALGORITHM 1. Pseudo-code for the multi-fidelity GP.

Require: $\mathbf{f}_L$, $\mathbf{f}_H$ (input frequencies), $\mathbf{y}_L$, $\mathbf{y}_H$ (observations),
 cov (covariance function), σ_{nL}^2, σ_{nH}^2 (noise level), $\mathbf{f}_*$ (target frequencies)
 $\mathbf{L} = \text{chol}(\mathbf{K} + \sigma_n^2 \mathbf{I})$
 $\boldsymbol{\alpha} = \mathbf{L}^T \backslash (\mathbf{L} \backslash [\mathbf{y}_L \, \mathbf{y}_H]^T)$
 evaluate predictive mean $\bar{\mathbf{h}}_* = \mathbf{K}_* \boldsymbol{\alpha}$
 $\boldsymbol{\beta} = \mathbf{L} \backslash \mathbf{K}_*$
 evaluate predictive covariance $\text{cov}(\mathbf{h}_*) = \mathbf{K}_{**} - \boldsymbol{\beta}^T \boldsymbol{\beta}$
 evaluate log likelihood $\log P(\mathbf{y}|\mathbf{f})$
  return $\bar{\mathbf{h}}_*$, $\text{cov}(\mathbf{h}_*)$, $\log P(\mathbf{y}|\mathbf{f})$

V. NUMERICAL EXAMPLE

This section involves the boundary element analysis of the vehicle cabin and training procedure of the multi-fidelity GP. Moreover, the results of the multi-fidelity GP are investigated for two objective functions: the SPL and energy density level. In Sec. VI, the error of the multi-fidelity approximation is analyzed.

A. Boundary element analysis of the cabin

In this study, the acoustic problem of an industrial vehicle cabin is investigated. The boundary element model of the cabin has been provided by BMW (Munich, Germany Gurbuz et al., 2022b). The cabin has the following dimensions: 3.032 m length, 1.554 m width, and 1.283 m height. We assume that air is the acoustic medium with the density, $\rho_a = 1.21$ kg/m³, and the speed of sound, $c_a = 343$ m/s. Two different boundary element meshes of the cabin are studied: A coarse mesh with 1906 degrees of freedom (DOFs) is considered as the LF model, whereas a fine mesh with 24 036 DOFs is adopted as the HF model. In the LF model, boundary elements with constant pressure

interpolation are deployed while a linear discontinuous pressure interpolation is used for the HF model (Marburg and Schneider, 2003). The LF cabin model is meshed with an average element edge length of 0.130 m, whereas the average element edge length in the HF mesh amounts to 0.065 m. This leads to 13 elements per wavelength at 200 Hz for the LF mesh and 26 elements per wavelength for the HF mesh. The meshes for the LF and HF models are schematically depicted in Fig. 1.

To excite the numerical model, we impose a structural particle velocity at the driver's footwell, i.e., $v_s = 0.001$ m/s. The excited boundary elements are visualized in Fig. 2. Regarding the boundary admittance, we impose the Robin boundary condition, $\rho_a c_a Y = f/f_{\text{ref}}$, with the reference frequency, $f_{\text{ref}} = 2800$ Hz, on each boundary element. In Marburg and Hardtke (1999), the reverberation time was measured in a vehicle cabin at five frequencies between 30 and 300 Hz. By using Eyring's formula, the average absorption coefficient and related boundary admittance were computed. Marburg and Hardtke introduced the reference frequency, $f_{\text{ref}} = 2800$ Hz, because it provided the best approximation for the magnitude of the boundary admittance.

As customer comfort plays a crucial role in the design of a vehicle cabin, the acoustic quantities are particularly relevant at the position of the driver's ear (Schmid et al., 2022). A schematic visualization of the field point representing the location of the driver's ear is depicted in Fig. 3. With booming noise being the most prominent problem in the vehicle interior design, the relevant frequency range is chosen to be 20–200 Hz (Luegmair and Schmid, 2020).

Prior to the multi-fidelity analysis, the SPL and sound energy density level are evaluated at the position of the driver's ear. These quantities are computed with the LF and HF models; see Figs. 4(a) and 4(b), respectively. To express the acoustic quantities on a dB scale, $\text{SPL} = 20 \log (|p|/p_{\text{ref}})$ and the sound energy density level, $L_e = 10 \log (e/e_{\text{ref}})$, are computed. For sound waves propagating in air, the reference sound pressure and reference sound energy density adopt to $p_{\text{ref}} = 2.0 \times 10^{-5}$ Pa and $e_{\text{ref}} = 1.0 \times 10^{-12}$ kg/ms², respectively.

The SPL data for the LF model exhibits low values in the frequency range from 20 to 100 Hz with a small peak
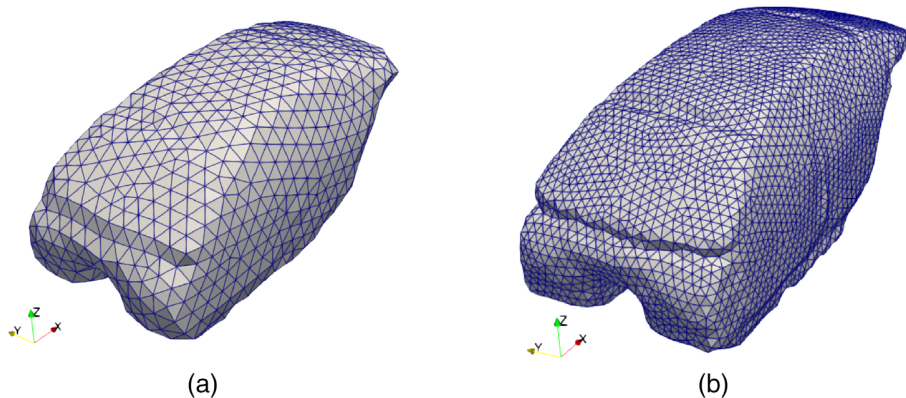

FIG. 1. (Color online) Two boundary element meshes for the two fidelity levels. A coarse mesh with 1906 DOFs is adopted as the LF model (a). A finer mesh with 24 036 DOFs is considered as the HF model (b).

(a)   (b)

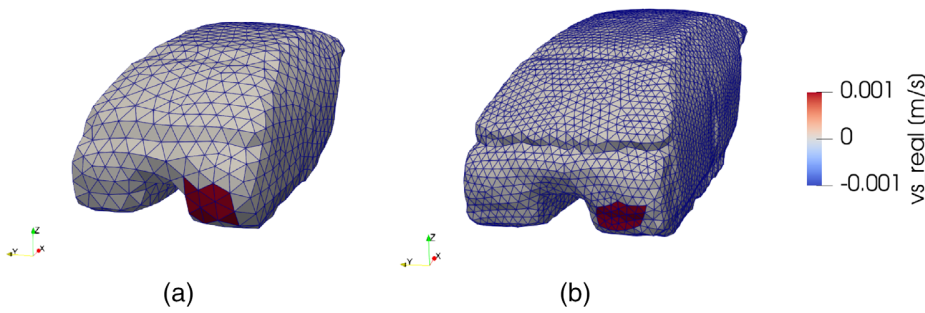J. Acoust. Soc. Am. **153** (4), April 2023

Gurbuz et al.   2011

FIG. 2. (Color online) Excited boundary elements on the LF mesh (a) and HF mesh (b) of the vehicle cabin, where the excitation is modeled as a Robin boundary condition with the real-valued structural velocity, $v_s = 0.001$ m/s.

around 75 Hz. In a previous study (Gurbuz *et al.*, 2022b), we performed the frequency sweep for the vehicle cabin without damping, e.g., $Y = 0$. In that study, we observed the first resonance frequency of the cabin at 71 Hz. In Fig. 4, the peak around that frequency is, thus, attributed to the occurrence of the first resonance. Above 100 Hz, the SPL at the driver's ear is higher except at 150 Hz, where the SPL decreases to 65 dB [Fig. 4(a)]. Here, again, two additional resonances of the cabin occur at 145 Hz and 170 Hz (Gurbuz *et al.*, 2022b). As the SPL is evaluated here between two resonances, a drop in the SPL response around 150 Hz becomes natural. Turning now to the sound energy density level with respect to the LF model, we observe a peak at 71 Hz, which is also attributed to the first resonance of the cabin; see Gurbuz *et al.* (2022b). On average, the energy density level is also higher for frequencies above 100 Hz [Fig. 4(b)]. Around 150 Hz, a small drop in the frequency response becomes apparent. As the energy density level is composed by the potential energy density, which is, in turn, determined by the sound pressure, the same explanation applies to the peak and drop in the energy density level response. Interestingly, we observe very similar SPL and energy density level responses for the HF model. Even though the HF data are generally on a lower level than the data observed in the LF simulation, the profiles of the HF and LF are in good agreement. In addition to a discretization error, the higher average SPL and energy density level for the LF mesh can be attributed to the area of the excited surface. As a matter of fact, the excited surface of the LF mesh, $A_{LF} = 0.116$ m^2, is significantly larger than the excitation area of the HF mesh, $A_{HF} = 0.064$ m^2 (Fig. 2). Also, the LF cabin with a length of 2.801 m is slightly shorter than the HF cabin, which is 2.911 m long. By this means, the energy supplied to the LF cabin turns out to be significantly higher

than that supplied to the HF cabin. It is worth noting that discrepancies in the transported energy are inevitable because meshes with different fidelity levels provide geometry approximations of varying quality. However, that circumstance is inherently considered within the proposed framework. After all, a positive correlation between the LF and HF data becomes apparent in Fig. 4, which is in accordance with the linearity assumption in Eq. (22).

B. Multi-fidelity GP training

To implement the multi-fidelity GP, a data selection strategy is required. The strategy proposes the frequencies, $\mathbf{f}_H$, at which we evaluate the response function of the HF model, $\mathbf{h}_H$. As the simulation of the HF model is accompanied with high computational costs, we are interested in the minimum possible number of HF simulations. At first glance, it might seem adequate to choose data points, which are equidistantly distributed across the frequency range. However, as frequency responses can exhibit regions with resonances or other active events, a more sophisticated approach is required. In this initial study, we introduce an empirical approach. First, the frequencies are identified, at which we observe the maxima in the frequency response and maxima of the curvatures in the LF data. Based on that suggestion, we select a frequency distribution such that we consider the largest possible frequency range. The HF simulation is then performed at the resulting frequencies. This approach is favorable because the LF model is fast to evaluate. Thus, the LF solution is abundant for a wide frequency range, which makes a sophisticated data acquisition strategy irrelevant. As a consequence, we perform the LF BEM simulation at numerous frequencies, which are equidistantly distributed over the entire frequency range.
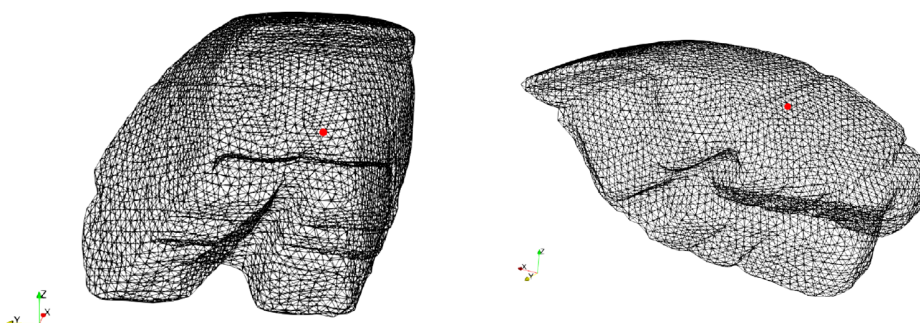

FIG. 3. (Color online) The field point position (red) at the driver's ear from a front view (left) and a lateral perspective (right). For the sake of conciseness, the field point position is only depicted for the HF model.
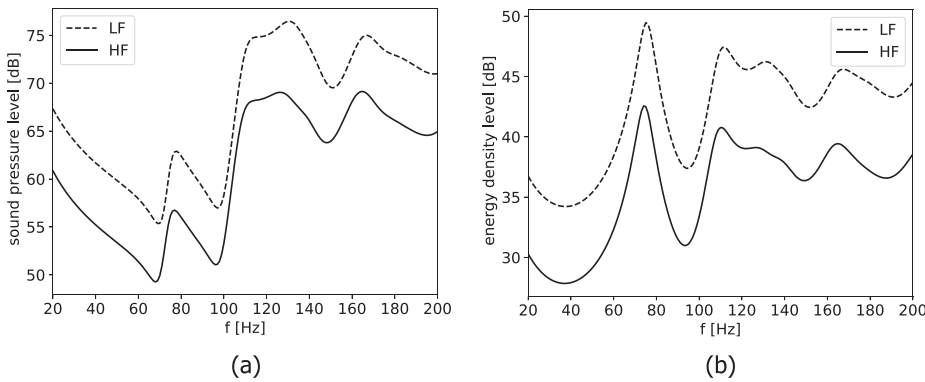
FIG. 4. The SPL (a) and energy density level (b) are evaluated with the LF model (dashed) and HF model (solid). The acoustic quantities are evaluated at the position of the driver's ear.

C. Sound pressure data

To assess the performance of the multi-fidelity GP, four cases are investigated in the following:

(a) Small LF data set with 37 points, small HF data set with four data points;

(b) large LF data set with 181 points, small HF data set with four data points;

(c) small LF data set with 37 points, large HF data set with eight data points; and

(d) large LF data set with 181 points, large HF data set with eight data points.

By varying the number of relevant data points, we analyze the influence of LF and HF data points on the performance of the proposed method. In the initial study, the noise level, $\sigma_n^2 = 0.5$ dB, is prescribed on the SPL response of the LF and HF models. Consequently, we obtain a SNR of 20.85 dB in the SPL analysis. Figure 5 shows the results for the multi-fidelity GP with regard to the SPL at the driver's ear. In the initial step, we assign 37 frequencies to the LF model and obtain the HF solution at four frequencies; see Fig. 5(a). Then, the number of LF frequency points is increased to 181 while the HF solution is still known at four frequencies [Fig. 5(b)]. Subsequently, we study the case with the HF solution at 8 frequencies based on the LF solution known at 37 frequencies [Fig. 5(c)]. In the final step, the multi-fidelity GP approximation is investigated for 181 frequency points in the LF solution and 8 points in the HF solution [Fig. 5(d)]. In all of the studies, the multi-fidelity GP approximation is compared to a reference solution. The reference solution is adopted by the HF solution at each frequency. In the initial study with 37 LF and 4 HF frequencies
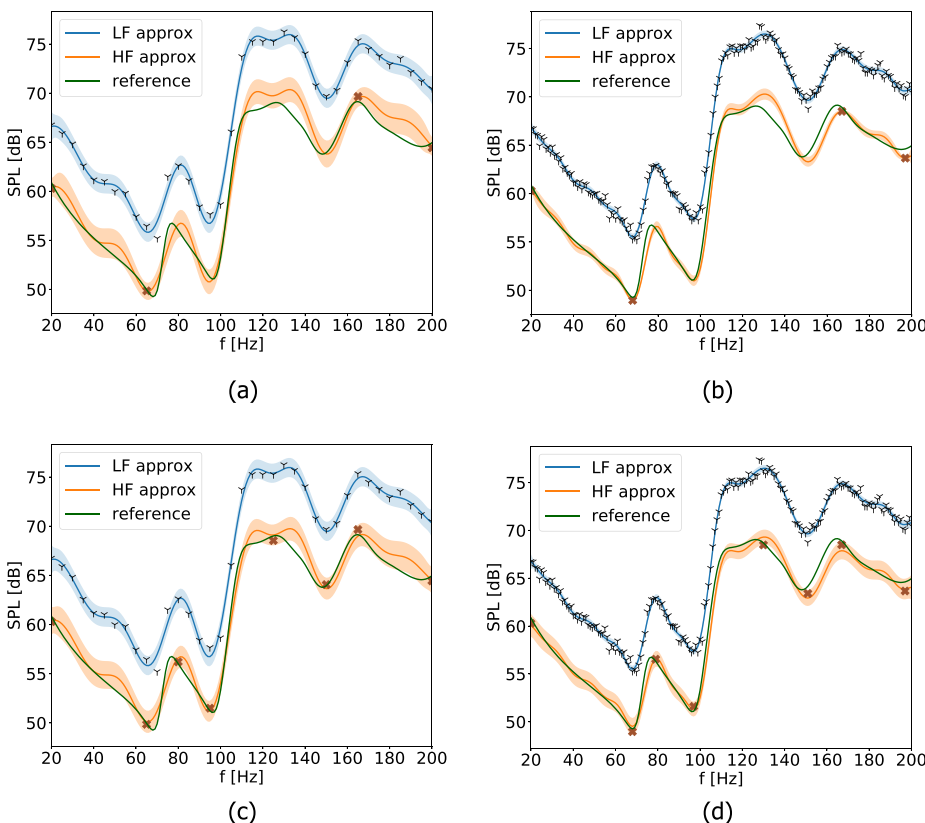

FIG. 5. (Color online) The SPL at the position of the driver's ear. The LF approximation (blue) of the SPL is evaluated at the LF frequency points (black Y-shaped markers). The HF approximation (orange) of the SPL is evaluated at the HF frequency points (orange crosses). The approximation of the HF model is compared to the reference solution (green). The approximations are associated with 95% confidence intervals (LF, light blue; HF, light orange). The LF and HF data are subject to noise corresponding to SNR = 20.85 dB.

[Fig. 5(a)], one can observe a good agreement between the HF approximation and reference solution. This is particularly the case in the frequency range 20–100 Hz, where the reference solution is either consistent with the HF approximation or at least lies within the 95% confidence interval. Even though we observe slight deviations from the reference solution above 100 Hz, it becomes apparent that the profiles of the HF approximation and reference are similar.

When the number of LF frequency points is increased to 181, the HF approximation is even more consistent with the reference solution; see Fig. 5(b). Small deviations are only apparent around 140 Hz. Moreover, we observe that the uncertainty interval is smaller in the LF approximation and the HF approximation is affected in a similar way. By this means, it becomes apparent that the reference solution is not considered within the uncertainties at the frequency range 150–165 Hz. For the remaining frequencies, one can observe that the HF approximation concurs well with the reference. Interestingly, this is also the case between 70 and 170 Hz, even though there is no HF frequency point in it.

In the next phase, the HF system responses are evaluated at 8 frequencies while the LF solution is known at, again, 37 frequencies [Fig. 5(c)]. The additional HF frequency points are placed in the frequency range between 70 and 170 Hz, where we observe an improvement of the HF approximation. This is particularly the case around 130 Hz, where the reference solution is either consistent with the HF approximation or at least included in the uncertainty interval.

In the final step, we analyze the multi-fidelity GP with 181 LF frequency points and eight HF frequency points; see

Fig. 5(d). In this study, we observe that the HF approximation is extremely consistent with the reference solution. This is especially the case around 130 Hz, where deviations appeared in the previous studies. Marginal differences, however, occur around 160 Hz, where the HF approximation slightly underestimates the reference solution. This discrepancy can be attributed to a violation of the linearity assumption in the correlation function; see Eq. (22). In particular, this inconsistency may be caused by lags in the frequency responses between the LF and HF response functions. The present results already indicate that the HF solution can be approximated with a drastically reduced number of HF simulations. The approximation can be improved by either adding a few HF frequency points or a great number of LF frequency points. Moreover, the findings show that the uncertainties in the HF approximation can be reduced by involving multiple frequency points. With the LF data being fast to obtain and, thus, abundant, it becomes apparent to prefer a large number of LF solutions for an efficient approximation.

D. Sound energy density data

Turning now to the analysis with regard to the sound energy density, the multi-fidelity GP is, again, initialized with 37 LF and 4 HF frequency points. Based on that, the number of frequency points is subsequently increased. In this study, we also prescribe the noise level $\sigma_n^2 = 0.5$ dB on the LF and HF data, resulting in a SNR of 18.51 dB. The results of the multi-fidelity GP regarding the sound energy
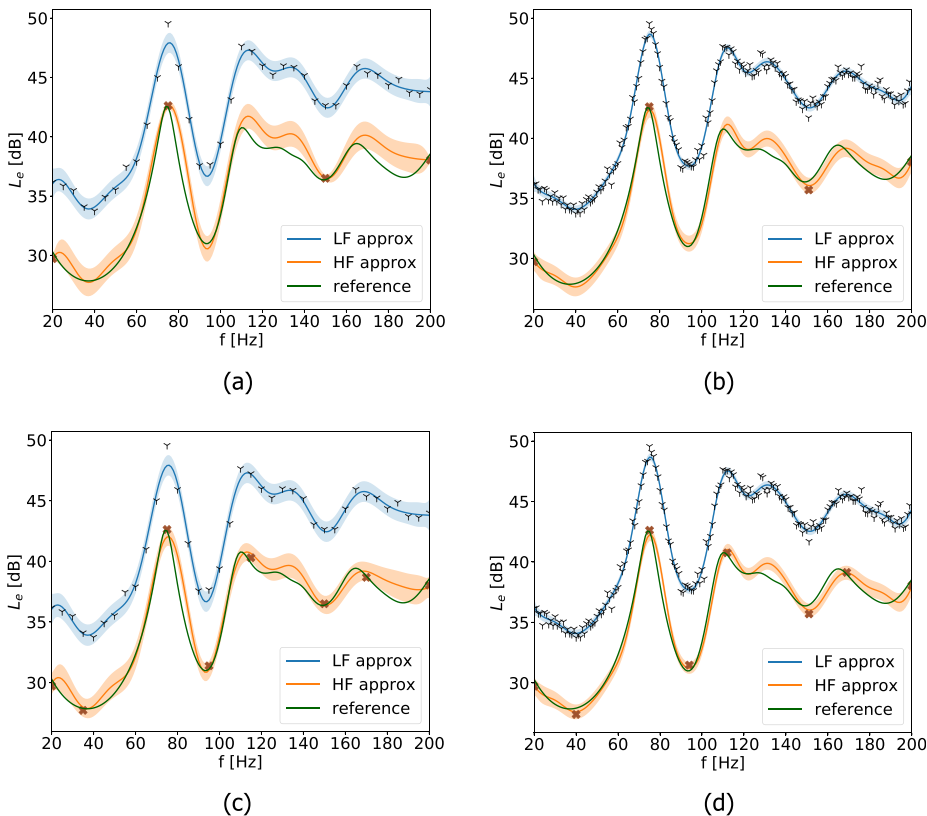

FIG. 6. (Color online) The total sound energy density level at the position of the driver's ear. The LF approximation of the sound energy density level is evaluated at the LF frequency points (black Y-shaped markers). The HF approximation (orange) of the energy density level is evaluated at the HF frequency points (orange crosses). The approximation of the HF model is compared to the reference solution (green). The approximations are associated with 95% confidence intervals (LF, light blue; HF, light orange). The LF and HF data are subject to noise corresponding to SNR = 18.51 dB.

2014   J. Acoust. Soc. Am. **153** (4), April 2023

Gurbuz *et al.*

density are depicted in Fig. 6. In the initial analysis (37 LF and 4 HF frequency points), the HF frequency points are approximately selected at 20, 80, 140, and 200 Hz, resulting in a nearly equidistant distribution; see Fig. 6(a). For this constellation, the multi-fidelity GP already yields an accurate approximation for the HF model. In particular, the resonance around 70 Hz and the average profile of the sound energy density level are recovered. Small deviations are only apparent between 110 and 150 Hz and 160 and 200 Hz, where the reference solution is overestimated. It is likely that the cause of this discrepancy is a result of the lack of HF solutions within these frequency ranges.

In the next phase, we increase the number of LF frequency points to 181 while keeping the number of HF points constant [Fig. 6(b)]. At first glance, one can observe an improved approximation for the HF solution. Closer inspection further reveals that the HF approximation agrees well with the reference solution for frequencies between 160 and 200 Hz. Although the profile of the HF approximation and reference resemble each other, we still notice differences between 110 and 150 Hz. Again, these differences are attributed to lags in the frequency responses between the LF and HF models. The fact that the number of LF solutions is increased leads to a decrease in the uncertainties and associated noise levels.

In the third study, we analyze, again, 37 LF points and increase the number of HF points to 8 [Fig. 6(c)]. In comparison to the initial study [Fig. 6(a)], the HF approximation agrees well with the reference solution over the entire frequency range. Small deviations similar to the results in Fig. 6(a) are only apparent above 170 Hz. By including additional HF solutions at 120 and at 170 Hz, the reference solution is considered in the uncertainty interval of the HF approximation even between 110 and 150 Hz and 180 and 200 Hz. The level of uncertainty remains nearly equal compared to the study in Fig. 6(a).

In the final case, the numbers of LF and HF frequency points are increased, i.e., 181 LF and 8 HF points [Fig. 6(d)]. Here, one can observe that the HF approximation is highly consistent with the reference solution, particularly, between 20 and 110 Hz. Marginal deviations only occur around 130 Hz, where the trend of the reference solution

cannot be adequately reproduced by the LF solution. Interestingly, we observe that the reference solution does not lie entirely in the uncertainty interval above 140 Hz. There is a marginal discrepancy around 150 Hz, which can be attributed to the presence of noise. The results of the energy density analysis also show that the HF reference solution can be well approximated by a multi-fidelity GP. At closer inspection, one can conclude that including additional HF data improves the approximation. However, the approximation can be similarly improved by solely including additional solutions of the LF model. The involvement of numerous LF solutions should be treated with caution as this approach is associated with the reduction of the uncertainty level. Nonetheless, this approach is highly favorable because a finer resolution of the LF solution provides an efficient way to improve the approximation of the reference solution at lower computational costs. Moreover, our results demonstrate that the proposed method performs very well even in the presence of noise. With the LF model being computationally efficient, the proposed framework provides an efficient method for the approximation of the frequency sweep in boundary element analyses. By this means, accurate and robust predictions can be achieved at lower costs by using multi-fidelity GPs.

E. Error and runtime analysis

To assess the quality of the approximation, the R^2 criterion is introduced as (Pesaran and Smith, 1994)

$$R^2 = 1 - \frac{(\mathbf{y}_* - \hat{\mathbf{y}}_H)^T (\mathbf{y}_* - \hat{\mathbf{y}}_H)}{(\mathbf{y}_* - \bar{\mathbf{y}}_H)^T (\mathbf{y}_* - \bar{\mathbf{y}}_H)}, \tag{37}$$

where $\mathbf{y}_*$ is the approximation of the HF frequency response function and $\hat{\mathbf{y}}_H$ is the HF reference solution. The entity, $\bar{\mathbf{y}}_H$, denotes the mean value of the HF reference solution, which is constantly distributed over the frequency range. For a perfect agreement between the approximation and reference solution, we would obtain $R^2 = 1$. The resulting R^2 values for the predictions of the multi-fidelity GP are depicted in Fig. 7. The results for the SPL analysis show that R^2 values around 0.95 are already achieved with two HF points; see
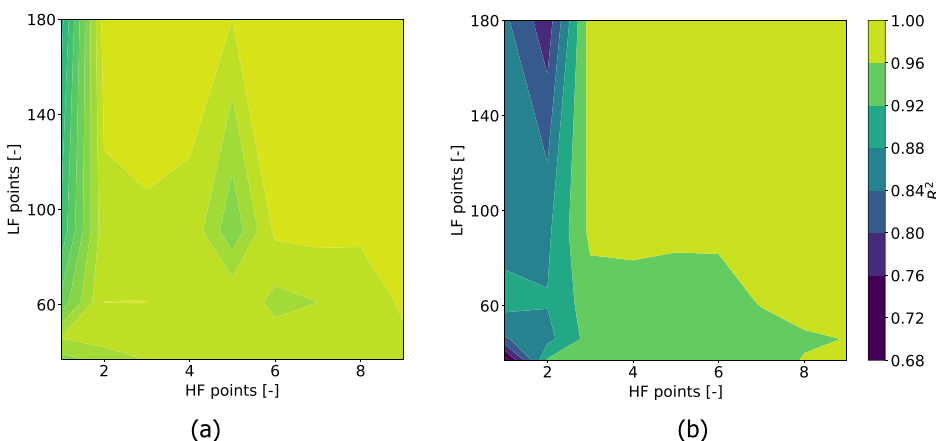

FIG. 7. (Color online) R^2 values are shown for the predictions of the multi-fidelity GP with regard to the SPL analysis (left) and energy density level analysis (right).

J. Acoust. Soc. Am. **153** (4), April 2023

Gurbuz *et al.* 2015

Fig. 7(a). By increasing the number of HF points, the R^2 criterion even amounts to 0.98. Regarding the LF data, we achieve R^2 values close to 0.95 for 60 and 100 LF points. For more than 100 LF points, the R^2 criterion rises to 0.98. This result indicates that the influence of the LF points is particularly strong when only a small number of HF points are considered. For more HF points, the performance of the multi-fidelity GP can be significantly improved by including additional LF points. Moreover, this result demonstrates that 4 HF and 100 LF points already suffice to achieve highly accurate predictions.

For the energy density analysis, the R^2 value is around 0.90 when we consider only two HF points [Fig. 7(b)]. By adding two further HF points, the R^2 criterion rapidly increases to values around 0.98. For more than four HF points, the R^2 value remains around 0.98. For 60 LF points, the R^2 criterion is around 0.90. By involving 100 or more LF points, one can observe R^2 values at 0.98. This finding also shows that 4 HF and 100 LF points suffice for an improved performance. The most interesting result to emerge from the R^2 data is that the performance of the multi-fidelity GP is essentially improved by including only a small number of HF points. Based on that, the performance is further improved by adding a decent amount of LF points. As anticipated, discrepancies in the approximation of the HF solution occurred at frequencies where the assumption of a linear correlation [Eq. (22)] was not valid. However, in our studies, they were only marginal; see Figs. 5(d) and 6(d). Next, we observed that the discrepancies could be reduced or at least considered in the uncertainty range by including additional information. This was accomplished by either involving the HF solution at a few more frequencies [Figs. 5(c) and 6(c)] or the LF solution at a decent amount of frequencies [Figs. 5(b) and 6(b)]. Presumably, advanced nonlinear correlation functions would further alleviate this issue.

Table I shows the comparison of the computational runtime between the multi-fidelity GP and HF BEM simulation. For this purpose, the approximation of the frequency sweep is investigated for two cases. The first case refers to the multi-fidelity GP with 37 LF and 4 HF simulations; see Fig. 5(a). In the second case, the frequency sweep is approximated with 181 LF and 8 HF simulations [Fig. 5(d)]. The resulting computational times are compared to the

reference method, where the HF simulation is performed at 181 frequencies. As the proposed method requires only a small number of HF simulations, the computational effort is drastically reduced. For instance, in the second case, the runtime is reduced to 3.71 h, resulting in a relative time saving of 92.4%. The computational time is reduced even further in the first case, where the approximation of the frequency sweep is obtained in 1.39 h. In this way, 97.1% of the total runtime is saved. Thus, multi-fidelity GPs provide an efficient technique to overcome the burden of high computational costs and time expense.

The present study raises the possibility to accelerate frequency sweep studies with the BEM. However, it is important to bear in mind that the present posterior multi-fidelity GP only holds for the position of the driver's ear and cannot be extrapolated to an arbitrary evaluation point. As the transfer functions of the cabin vary for different evaluation points, the multi-fidelity GP needs to be trained again when the position of the evaluation point changes. More specifically, the frequency selection strategy, as introduced in Sec. V B, and the LF model simulations have to be performed from scratch to obtain new proposals for the HF simulations. In contrast to this, the frequency range remains unaffected because it is defined by the underlying problem.

In the sense of a Bayesian method, multi-fidelity models based on GPs account for uncertainties within the data generation process. In the context of the acoustic design of a vehicle cabin, uncertainties are ubiquitous in early design stages. They may occur in the boundary conditions, particularly, in the excitation from the enveloping chassis or boundary admittance of the cabin. Moreover, modifications on the cabin geometry in the development cycle result in variations of the evaluated position. Thus, the position of the driver's ear becomes an additional source of uncertainty. Uncertainties can further occur as a result of simplifying model assumptions. For the Helmholtz equation, this may involve the assumption that the underlying acoustic problem can be considered to be linear.

Finally, it should be noted that our findings are conducted with a squared exponential covariance function. Among the vast amount of covariance functions, complex-valued and physics-based covariance functions (Caviedes-Nozal et al., 2021) sound very promising as they account for spatial information on the characteristics of the propagating waves.

VI. CONCLUSIONS

This paper set out to improve the efficiency in the design of acoustic systems. Therefore, a multi-fidelity model was developed based on boundary element simulations of two different meshes. A coarse resolution of the mesh was adopted as the LF model, whereas a fine mesh was considered as the HF model. The fidelity levels were realized by GPs, which were trained with the related frequency responses. To demonstrate the effectiveness of our method, we investigated a vehicle interior noise problem, where we

TABLE I. Runtime comparison of the multi-fidelity GPs with the full frequency sweep for the HF BEM model (reference). The multi-fidelity GPs are evaluated for 37 LF points, 4 HF points (case 1) and 181 LF points, 8 HF points (case 2). The runtime for a single LF simulation amounts to 30.45 s, whereas a single HF simulation required 965.04 s.

	Multi-fidelity GPs, case 1	Multi-fidelity GPs, case 2	Reference solution
Number of HF simulations	4	8	181
Number of LF simulations	37	181	—
Multi-fidelity GP training	20.87 s	142.05 s	—
Total runtime	1.39 h	3.71 h	48.52 h

2016   J. Acoust. Soc. Am. **153** (4), April 2023

Gurbuz et al.

analyzed the frequency response of the cabin with respect to the driver's ear. Regarding the objective function, the SPL and sound energy density at the driver's ear were used. In our study, we compared the approximation of the multi-fidelity GP with the HF solution at each frequency. Moreover, we assessed the performance of the proposed method by studying the influence of LF and HF solutions at additional frequencies. The results in our study have shown that the HF solutions were efficiently approximated by the proposed method. In addition to this, sensitivities to model parameters and uncertainties arising from the data generation process were inherently quantified. By this means, multi-fidelity GPs provide an efficient and robust tool to determine the frequency-dependent characteristics of acoustic systems. The evidence from our work, thus, emphasizes the exploration of multi-fidelity GPs in acoustic problems. With a rather semi-empirical approach to determine the relevant frequencies, a natural progression of this work is to implement a more elegant technique for the selection of frequency points at which the HF model is evaluated. One possible strategy could involve a decision criterion in the form of a loss function. Future work needs to examine the links between the HF model and LF model because we only focused on linearly correlated models in this study. Moreover, we strongly recommend the integration of different data generation sources in the proposed framework. This involves particularly physical experiments as well as analytical solutions within a model of multiple fidelity levels.

ACKNOWLEDGMENTS

APPENDIX: CONDITIONING ON OBSERVED DATA

Following Williams and Rasmussen (2006), the joint probability distribution of two Gaussian random vectors, $\mathbf{x}$ and $\mathbf{y}$, reads

$$\begin{bmatrix} \mathbf{x} \\ \mathbf{y} \end{bmatrix} \sim \mathcal{N}\left(\begin{bmatrix} \boldsymbol{\mu}_x \\ \boldsymbol{\mu}_y \end{bmatrix}, \begin{bmatrix} \mathbf{A} & \mathbf{C} \\ \mathbf{C}^T & \mathbf{B} \end{bmatrix} \right). \tag{A1}$$

The conditional probability distribution for $\mathbf{x}$ given $\mathbf{y}$, then, can be expressed by

$$P(\mathbf{x}|\mathbf{y}) = \mathcal{N}(\boldsymbol{\mu}_x + \mathbf{C}\mathbf{B}^{-1}(\mathbf{y} - \boldsymbol{\mu}_y), \mathbf{A} - \mathbf{C}\mathbf{B}^{-1}\mathbf{C}^T). \tag{A2}$$

In our study, the observations are stored in $\mathbf{y}$ while the unknown function values are expressed by $\mathbf{x}$.

Albert, C. G., and Rath, K. (2020). "Gaussian process regression for data fulfilling linear differential equations with localized sources," Entropy 22(2), 152.

Baydoun, S. K., Voigt, M., Jelich, C., and Marburg, S. (2020). "A greedy reduced basis scheme for multifrequency solution of structural acoustic systems," Int. J. Numer. Methods Eng. 121(2), 187–200.

Baydoun, S. K., Voigt, M., and Marburg, S. (2021). "Low-rank iteration schemes for the multi-frequency solution of acoustic boundary element equations," J. Theor. Comp. Acoust. 29(03), 2150004.

Caviedes-Nozal, D., Riis, N. A., Heuchel, F. M., Brunskog, J., Gerstoft, P., and Fernandez-Grande, E. (2021). "Gaussian processes for sound field reconstruction," J. Acoust. Soc. Am. 149(2), 1107–1119.

Cazzolato, B. S., and Hansen, C. H. (1998). "Active control of sound transmission using structural error sensing," J. Acoust. Soc. Am. 104(5), 2878–2889.

Craig, P. S., Goldstein, M., Seheult, A., and Smith, J. (1998). "Constructing partial prior specifications for models of complex physical systems," J. R. Stat. Soc.: Ser. D 47(1), 37–53.

Cumming, J. A., and Goldstein, M. (2009). "Small sample bayesian designs for complex high-dimensional models based on information gained using fast approximations," Technometrics 51(4), 377–388.

Cutajar, K., Pullin, M., Damianou, A., Lawrence, N., and González, J. (2019). "Deep Gaussian processes for multi-fidelity modeling," arXiv:1903.07320.

Guo, M., Manzoni, A., Amendt, M., Conti, P., and Hesthaven, J. S. (2022). "Multi-fidelity regression using artificial neural networks: Efficient approximation of parameter-dependent output quantities," Comput. Methods Appl. Mech. Eng. 389, 114378.

Gurbuz, C., Eser, M., Schmid, J. D., Marburg, S., and Luegmair, M. (2022a). "Gaussian processes for transfer path analysis applied on vehicle body vibration problems," SAE Technical Paper 2022-01-0948 (Society of Automotive Engineers, Warrendale, PA).

Gurbuz, C., and Marburg, S. (2022). "Efficient analysis of energy-based surface contributions for an entire acoustic cavity," J. Theor. Comput. Acoust. (published online 2022).

Gurbuz, C., Schmid, J. D., Luegmair, M., and Marburg, S. (2022b). "Energy density-based non-negative surface contributions in interior acoustics," J. Sound Vib. 527, 116824.

Hensman, J., Mills, R., Pierce, S., Worden, K., and Eaton, M. (2010). "Locating acoustic emission sources in complex structures using Gaussian processes," Mech. Syst. Signal Process. 24(1), 211–223.

Hoffer, J. G., Geiger, B. C., and Kern, R. (2022). "Gaussian process surrogates for modeling uncertainties in a use case of forging superalloys," Appl. Sci. 12(3), 1089.

Hüllermeier, E., and Waegeman, W. (2021). "Aleatoric and epistemic uncertainty in machine learning: An introduction to concepts and methods," Mach. Learn. 110(3), 457–506.

Jelich, C., Koji Baydoun, S., Voigt, M., and Marburg, S. (2021). "A greedy reduced basis algorithm for structural acoustic systems with parameter and implicit frequency dependence," Int. J. Numer. Meth. Eng. 122(24), 7409–7430.

Jiang, J., Su, G., Yan, Z., Zheng, Z., and Hu, X. (2022). "Rock crack type identification by Gaussian process learning on acoustic emission," Appl. Acoust. 197, 108926.

Kennedy, M. C., and O'Hagan, A. (2000). "Predicting the output from a complex computer code when fast approximations are available," Biometrika 87(1), 1–13.

Kinsler, L. E., Frey, A. R., Coppens, A. B., and Sanders, J. V. (2000). Fundamentals of Acoustics (Wiley, New York).

Koopmann, G. H., and Fahnline, J. B. (1997). Designing Quiet Structures: A Sound Power Minimization Approach (Academic Press, San Diego, London).

Le Gratiet, L., and Garnier, J. (2014). "Recursive co-kriging model for design of computer experiments with multiple levels of fidelity," Int. J. Uncertainty Quantif. 4(5), 365–386.

Luegmair, M., and Schmid, J. D. (2020). "Challenges in vibroacoustic vehicle body simulation including uncertainties," SAE Technical Paper 2020-01-1571.

Marburg, S. (2002). "Developments in structural-acoustic optimization for passive noise control," ARCO 9(4), 291–370.

Marburg, S. (2008). "A unified approach to finite and boundary element discretization in linear time–harmonic acoustics," in Computational Acoustics of Noise Propagation in Fluids – Finite and Boundary Element Methods, edited by S. Marburg and B. Nolte (Springer, Berlin, Heidelberg), pp. 1–34.

Marburg, S. (2018). "Boundary element method for time-harmonic acoustic problems," in Computational Acoustics, edited by M. Kaltenbacher (Springer, Cham), pp. 69–158.

JASA

Marburg, S., and Hardtke, H.-J. (**1999**). "A study on the acoustic boundary admittance. determination, results and consequences," Eng. Anal. Boundary Elem. **23**(9), 737–744.

Marburg, S., and Hardtke, H.-J. (**2001**). "Shape optimization of a vehicle hat-shelf: Improving acoustic properties for different load cases by maximizing first eigenfrequency," Comput. Struct. **79**(20-21), 1943–1957.

Marburg, S., and Schneider, S. (**2003**). "Influence of element types on numeric error for acoustic boundary elements," J. Comp. Acoust. **11**(03), 363–386.

Michalopoulou, Z.-H., and Gerstoft, P. (**2022**). "Uncertainty reduction in matched field inversion using Gaussian processes," J. Acoust. Soc. Am. **151**(4), A66.

Michalopoulou, Z.-H., Gerstoft, P., and Caviedes-Nozal, D. (**2021**). "Matched field source localization with Gaussian processes," JASA Express Lett. **1**(6), 064801.

Panagiotopoulos, D., Desmet, W., and Deckers, E. (**2022**). "Parametric model order reduction for acoustic boundary element method systems through a multiparameter krylov subspaces recycling strategy," Int. J. Numer. Methods Eng. **123**, 5546–5569.

Parussini, L., Venturi, D., Perdikaris, P., and Karniadakis, G. E. (**2017**). "Multi-fidelity Gaussian process regression for prediction of random fields," J. Comput. Phys. **336**, 36–50.

Pesaran, M. H., and Smith, R. J. (**1994**). "A generalized R^2 criterion for regression models estimated by the instrumental variables method," Econometrica **62**(3), 705–710.

Preuss, S., Gurbuz, C., Jelich, C., Baydoun, S. K., and Marburg, S. (**2022**). "Recent advances in acoustic boundary element methods," J. Theor. Comp. Acoust. **30**(03), 2240002.

Raissi, M., and Karniadakis, G. (**2016**). "Deep multi-fidelity Gaussian processes," arXiv:1604.07484.

Raissi, M., Perdikaris, P., and Karniadakis, G. E. (**2017a**). "Inferring solutions of differential equations using noisy multi-fidelity data," J. Comput. Phys. **335**, 736–746.

Raissi, M., Perdikaris, P., and Karniadakis, G. E. (**2017b**). "Machine learning of linear differential equations using Gaussian processes," J. Comput. Phys. **348**, 683–693.

Raissi, M., Perdikaris, P., and Karniadakis, G. E. (**2018**). "Numerical Gaussian processes for time-dependent and nonlinear partial differential equations," SIAM J. Sci. Comput. **40**(1), A172–A198.

Schmid, J. D., Hildenbrand, A., Gurbuz, C., Luegmair, M., and Marburg, S. (**2022**). "Variational autoencoders for dimensionality reduction of automotive vibroacoustic models," SAE Technical Paper 2022-01-0941.

Schmid, J. M., Fernandez-Grande, E., Hahmann, M., Gurbuz, C., Eser, M., and Marburg, S. (**2021**). "Spatial reconstruction of the sound field in a room in the modal frequency range using Bayesian inference," J. Acoust. Soc. Am. **150**(6), 4385–4394.

Soize, C. (**2017**). "Fundamental notions in stochastic modeling of uncertainties and their propagation in computational models," in Uncertainty Quantification (Springer, Cham), pp. 1–15.

Sommerfeldt, S. D., and Nashif, P. J. (**1994**). "An adaptive filtered-x algorithm for energy-based active control," J. Acoust. Soc. Am. **96**(1), 300–306.

Suzuki, S., Maruyama, S., and Ido, H. (**1989**). "Boundary element analysis of cavity noise problems with complicated boundary conditions," J. Sound Vib. **130**(1), 79–96.

Tanaka, N., and Kobayashi, K. (**2006**). "Cluster control of acoustic potential energy in a structural/acoustic cavity," J. Acoust. Soc. Am. **119**(5), 2758–2771.

Torzoni, M., Manzoni, A., and Mariani, S. (**2023**). "A deep neural network, multi-fidelity surrogate model approach for Bayesian model updating in SHM," in European Workshop on Structural Health Monitoring, edited by P. Rizzo and A. Milazzo (Springer, Cham), pp. 1076–1086.

Williams, C. K., and Rasmussen, C. E. (**2006**). Gaussian Processes for Machine Learning (MIT Press, Cambridge, MA), Vol. 2.

Wu, T. W. (ed.) (**2000**). Boundary Element in Acoustics: Fundamentals and Computer Codes (WIT Press, Southampton).

Wu, T., and Seybert, A. (**1991**). "A weighted residual formulation for the chief method in acoustics," J. Acoust. Soc. Am. **90**(3), 1608–1614.

Xie, X., and Liu, Y. (**2021**). "Efficient multi-frequency solutions of FE–BE coupled structural–acoustic problems using arnoldi-based dimension reduction approach," Comput. Methods Appl. Mech. Eng. **386**, 114126.

Xie, X., Wang, W., He, K., and Li, G. (**2022**). "Fast model order reduction boundary element method for large-scale acoustic systems involving surface impedance," Comput. Methods Appl. Mech. Eng. **400**, 115618.

Xie, X., Zuo, Q., Chen, H., Xu, Y., Yi, Z., and He, K. (**2023**). "A non-intrusive model order reduction boundary element method for frequency sweeps of 2D acoustics," J. Sound Vib. **544**, 117396.

Yardim, C., Michalopoulou, Z.-H., and Gerstoft, P. (**2011**). "An overview of sequential bayesian filtering in ocean acoustics," IEEE J. Ocean. Eng. **36**(1), 71–89.